



**Development of new nanostructured  
composites based on block copolymers  
or nanostructured thermosetting  
systems modified with nanoparticles**

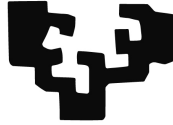
**Laida Cano Gonzalez**

**Donostia-San Sebastián, 2015**





eman ta zabal zazu



Universidad  
del País Vasco

Euskal Herriko  
Unibertsitatea

**DEVELOPMENT OF NEW NANOSTRUCTURED  
COMPOSITES BASED ON BLOCK COPOLYMERS  
OR NANOSTRUCTURED THERMOSETTING  
SYSTEMS MODIFIED WITH NANOPARTICLES**

**Laida Cano Gonzalez**

**Thesis Supervisor: Dr. Agnieszka Tercjak**

PhD Program Renewable Materials Engineering

Department of Chemical and Environmental Engineering

Polytechnic School of Donostia-San Sebastián

Donostia-San Sebastián, 2015



## Summary

This investigation work is focused on the development of novel nanostructured materials based on block copolymers modified with metal oxide nanoparticles and on the other hand, on epoxy based thermosetting systems modified with block copolymers. The main interest consists in taking advantage of the ability of block copolymers to obtain nanostructured materials as well as in achieving the enhancement of the final properties of the designed materials, such as conductive, optical, magnetic and mechanical properties.

The work is composed of 9 chapters. Chapter 1 is a general introduction about nanotechnology and the use of block copolymers as templates for the development of hybrid inorganic/organic nanocomposites as well as their use as modifiers for thermosetting systems. In Chapter 2, all the experimental techniques employed for the characterization of resulting materials are described.

Chapters from 3 to 6 describe the preparation and characterization of inorganic/organic nanocomposites, using the polystyrene-*block*-polymethyl methacrylate block copolymer as a template for the dispersion of inorganic nanoparticles. In Chapter 3, commercial TiO<sub>2</sub> nanocrystals are incorporated and in Chapter 4, synthesized TiO<sub>2</sub> nanorods, and both kinds of nanocomposites are characterized mainly in terms of their conductive and optical properties in function of TiO<sub>2</sub> content. After seeing the promising results of nanocomposites designed using synthesized TiO<sub>2</sub> nanorods, these nanocomposites are utilized for the fabrication of electro-devices in Chapter 5, as an approach to a potential application in the field of energy conversion. In addition, Chapter 6 is based on the development of nanocomposites with synthesized  $\gamma$ -Fe<sub>2</sub>O<sub>3</sub> nanocrystals, and their characterization is focused on the magnetic properties, together with a deep study of the morphology of the designed materials.

Epoxy based thermosetting systems modified with block copolymers are studied in Chapters 7 and 8. In Chapter 7, the same block copolymer as in previous chapters is used, whereas in Chapter 8 the polyethylene oxide-*block*-polypropylene oxide-*block*-polyethylene oxide triblock copolymer was employed. The aim of modifying a thermosetting matrix with a block copolymer is based on the improvement in the mechanical properties.

Finally, the general conclusions of this investigation work are summarized in Chapter 9 as well as future work and scientific contributions related with the results obtained along this investigation study.

## Motivation and objectives

Materials with diverse structures at the nanoscale can show very different properties compared to their properties at the macroscale. Nanotechnology is not simply working at smaller dimensions. Working at the nanoscale enables to utilize the unique physical, chemical, mechanical, and optical properties of materials that naturally occur at that scale. Therefore, the attraction of nanotechnology stems from the unique quantum and surface phenomena that matter exhibits at the nanoscale, making possible novel applications and designed materials with tunable properties.

In this context, block copolymers represent a simple path to reach nanostructures and this fact makes them excellent materials to create novel complex materials, such as nanocomposites, among others. The combination of block copolymers with functional nanoparticles can lead to nanocomposites for a high number of applications in many fields of nanotechnology due to the appealing properties of nanoparticles and their capacity to transfer these properties to a block copolymer matrix when they are well dispersed or selectively located in one phase of the block copolymer.

On the other hand, the self-assembly ability of block copolymers has also resulted to be appropriate to achieve the nanostructuration of thermosetting systems based on epoxy resins, together with reaching an important enhancement in some of their properties, mechanical properties, in particular.

Regarding this, the main objective of this work consists in the development of novel nanostructured materials by employing block copolymers. In particular, the following objectives are proposed:

- Design novel nanocomposite materials based on block copolymers and different inorganic metal oxide nanoparticles,  $\text{TiO}_2$  and  $\gamma\text{-Fe}_2\text{O}_3$  nanoparticles, commercially acquired as well as *ex situ* synthesized.
- Study the morphology and optical, conductive and magnetic properties of the designed nanocomposites, in function of the nanoparticle content in the polymeric matrix.
- Employ nanocomposites for the fabrication of electro-devices as a first approach of a potential application in the field of energy conversion.

- Design epoxy based thermosetting systems modified with a block copolymer with the aim to enhance the mechanical properties.

# Contents

<b>1. Introduction</b>	<b>3</b>
<b>1.1. Block copolymers</b>	<b>4</b>
1.1.1. Phase behavior	5
1.1.2. Block copolymers applications	8
1.1.3. Block copolymer based nanocomposites	9
<b>1.2. Inorganic nanoparticles</b>	<b>10</b>
1.2.1. Hybrid inorganic/organic nanocomposites	12
<b>1.3. Epoxy based thermosets</b>	<b>13</b>
1.3.1. Epoxy based thermosetting systems modified with block copolymers	15
<b>1.4. References</b>	<b>17</b>
<b>2. Characterization techniques</b>	<b>25</b>
<b>2.1. Physico-chemical characterization</b>	<b>25</b>
2.1.1. X-ray diffraction (XRD)	25
2.1.2. Fourier transform infrared spectroscopy (FTIR)	25
<b>2.2. Thermal characterization</b>	<b>26</b>
2.2.1. Differential scanning calorimeter (DSC)	26
<b>2.3. Morphological characterization</b>	<b>26</b>
2.3.1. Atomic force microscopy (AFM)	26
2.3.2. Transmission electron microscopy (TEM)	27
2.3.3. Scanning electron microscopy (SEM)	28
<b>2.4. Conductive characterization</b>	<b>29</b>
2.4.1. Electrostatic force microscopy (EFM)	29
2.4.2. PeakForce tunneling atomic force microscopy (TUNA)	29
2.4.3. Keithley semiconductor analyzer	30
<b>2.5. Magnetic characterization</b>	<b>31</b>
2.5.1. Magnetic force microscopy (MFM)	31
<b>2.6. Mechanical characterization</b>	<b>32</b>
2.6.1. PeakForce Quantitative nanomechanical measurements (QNM)	32
2.6.2. Materials testing system (MTS)	32
2.6.2.1. Flexural test	33

2.6.2.2. Fracture toughness test	33
<b>2.7. Optical characterization</b>	<b>34</b>
2.7.1. Ultraviolet-visible spectroscopy	34
<b>2.8. Surface characterization</b>	<b>35</b>
2.8.1. Water contact angle	35
<b>2.9. References</b>	<b>35</b>
<b>3. Polystyrene-<i>block</i>-polymethyl methacrylate diblock copolymer and TiO<sub>2</sub> nanocrystals based nanocomposites</b>	<b>39</b>
<b>3.1. Introduction</b>	<b>39</b>
<b>3.2. Materials and methods</b>	<b>40</b>
3.2.1. Materials	40
3.2.2. TiO <sub>2</sub> NC/PS- <i>b</i> -PMMA nanocomposite preparation	40
3.2.3. Characterization techniques	41
3.2.3.1. X-ray diffraction	41
3.2.3.2. Differential scanning calorimeter	41
3.2.3.3. Atomic force microscopy	41
3.2.3.4. Electrostatic force microscopy	42
3.2.3.5. Ultraviolet-visible spectroscopy	42
<b>3.3. Results and discussion</b>	<b>42</b>
3.3.1. Characterization of the commercial TiO <sub>2</sub> nanocrystals	42
3.3.2. Characterization of the TiO <sub>2</sub> NC/PS- <i>b</i> -PMMA nanocomposites	43
3.3.2.1. Thermal behavior	43
3.3.2.2. Morphology	44
3.3.2.3. Conductive properties	46
3.3.2.4. Optical properties	48
<b>3.4. Conclusions</b>	<b>49</b>
<b>3.5. References</b>	<b>49</b>
<b>4. Polystyrene-<i>block</i>-polymethyl methacrylate diblock copolymer and synthesized TiO<sub>2</sub> nanorods based nanocomposites</b>	<b>53</b>
<b>4.1. Introduction</b>	<b>53</b>
<b>4.2. Materials and methods</b>	<b>55</b>

4.2.1. Materials	55
4.2.2. Synthesis of TiO <sub>2</sub> nanorods	55
4.2.3. TiO <sub>2</sub> NR/PS- <i>b</i> -PMMA nanocomposite preparation	55
4.2.4. Characterization techniques	56
4.2.4.1. Fourier transform infrared spectroscopy	56
4.2.4.2. Transmission electron microscopy	56
4.2.4.3. Atomic force microscopy	56
4.2.4.4. Electrostatic force microscopy	57
4.2.4.5. Keithley semiconductor analyzer	57
4.2.4.6. Tunneling atomic force microscopy	57
4.2.4.7. Ultraviolet-visible spectroscopy	57
<b>4.3. Results and discussion</b>	<b>58</b>
4.3.1. Characterization of the synthesized TiO <sub>2</sub> nanorods	58
4.3.2. Characterization of the TiO <sub>2</sub> NR/PS- <i>b</i> -PMMA nanocomposites	59
4.3.2.1. Visual appearance	59
4.3.2.2. Morphology	59
4.3.2.3. Conductive properties	62
4.3.2.4. Optical properties	69
<b>4.4. Conclusions</b>	<b>70</b>
<b>4.5. References</b>	<b>71</b>
<b>5. Polystyrene-<i>block</i>-polymethyl methacrylate diblock copolymer and synthesized TiO<sub>2</sub> nanorods based nanocomposites for potential solar cell application</b>	<b>77</b>
<b>5.1. Introduction</b>	<b>77</b>
<b>5.2. Materials and methods</b>	<b>79</b>
5.2.1. Materials	79
5.2.2. ITO-glass/PEDOT:PSS/P3HT/(TiO <sub>2</sub> NR/PS- <i>b</i> -PMMA) electro-devices fabrication	79
5.2.3. Characterization techniques	79
5.2.3.1. Atomic force microscopy	79
5.2.3.2. Keithley semiconductor analyzer	80

5.2.3.3. Tunneling atomic force	80
5.2.3.4. Ultraviolet-visible spectroscopy	80
<b>5.3. Results and discussion</b>	<b>80</b>
5.3.1. Characterization of ITO-glass/PEDOT:PSS/P3HT/(TiO <sub>2</sub> NR/PS- <i>b</i> -PMMA) electro-devices	80
5.3.1.1. Morphology	81
5.3.1.2. Conductive properties	82
5.3.1.3. Optical properties	87
<b>5.4. Conclusions</b>	<b>87</b>
<b>5.5. References</b>	<b>88</b>
<b>6. Polystyrene-<i>block</i>-polymethyl methacrylate diblock copolymer and synthesized <math>\gamma</math>-Fe<sub>2</sub>O<sub>3</sub> nanocrystals based nanocomposites</b>	<b>93</b>
<b>6.1. Introduction</b>	<b>93</b>
<b>6.2. Materials and methods</b>	<b>95</b>
6.2.1. Materials	95
6.2.2. Synthesis of $\gamma$ -Fe <sub>2</sub> O <sub>3</sub> nanocrystals	92
6.2.3. $\gamma$ -Fe <sub>2</sub> O <sub>3</sub> NC/PS- <i>b</i> -PMMA nanocomposite preparation	96
6.2.4. Characterization techniques	96
6.2.4.1. Fourier transform infrared spectroscopy	96
6.2.4.2. Transmission electron microscopy	96
6.2.4.3. Atomic force microscopy	97
6.2.4.4. Scanning electron microscopy	97
6.2.4.5. Magnetic force microscopy	97
<b>6.3. Results and discussion</b>	<b>98</b>
6.3.1. Characterization of the synthesized $\gamma$ -Fe <sub>2</sub> O <sub>3</sub> nanocrystals	98
6.3.2. Characterization of the $\gamma$ -Fe <sub>2</sub> O <sub>3</sub> NC/PS- <i>b</i> -PMMA nanocomposites	99
6.3.2.1. Visual appearance	99
6.3.2.2. Morphology	100
6.3.2.3. Magnetic properties	106
<b>6.4. Conclusions</b>	<b>109</b>
<b>6.5. References</b>	<b>110</b>

<b>7. Epoxy based thermosetting system modified with polystyrene-<i>block</i>- polymethyl methacrylate diblock copolymer</b>	<b>115</b>
<b>7.1. Introduction</b>	<b>115</b>
<b>7.2. Materials and methods</b>	<b>116</b>
7.2.1. Materials	116
7.2.2. PS- <i>b</i> -PMMA/(DGEBA-MCDEA) cured thermosetting system preparation	117
7.2.3. Characterization techniques	118
7.2.3.1. Differential scanning calorimeter	118
7.2.3.2. Atomic force microscopy	118
7.2.3.3. Materials testing system	118
7.2.3.4. PeakForce quantitative nanomechanical mapping	119
<b>7.3. Results and discussion</b>	<b>119</b>
7.3.1. Characterization of the neat DGEBA-MCDEA cured system and PS- <i>b</i> -PMMA/(DGEBA-MCDEA) cured systems	119
7.3.1.1. Transparency	119
7.3.1.2. Miscibility and thermal behavior	120
7.3.1.3. Morphology	122
7.3.1.4. Mechanical properties	126
<b>7.4. Conclusions</b>	<b>131</b>
<b>7.5. References</b>	<b>132</b>
<b>8. Epoxy based thermosetting system modified with polyethylene oxide-<i>block</i>-polypropylene oxide-<i>block</i>-polyethylene oxide triblock copolymer</b>	<b>137</b>
<b>8.1. Introduction</b>	<b>137</b>
<b>8.2. Materials and methods</b>	<b>138</b>
8.2.1. Materials	138
8.2.2. PEO- <i>b</i> -PPO- <i>b</i> -PEO/(DGEBA-MXDA) cured thermosetting system preparation	139
8.2.3. Characterization techniques	140
8.2.3.1. Differential scanning calorimeter	140
8.2.3.2. Atomic force microscopy	140

8.2.3.3. Transmission electron microscopy	140
8.2.3.4. Materials testing system	140
8.2.3.5. PeakForce quantitative nanomechanical mapping	141
8.2.3.6. Ultraviolet-visible spectroscopy	141
8.2.3.7. Contact angle	141
<b>8.3. Results and discussion</b>	<b>142</b>
8.3.1. Characterization of the neat DGEBA-MXDA cured system and PEO- <i>b</i> -PPO- <i>b</i> -PEO/(DGEBA-MXDA) cured systems	142
8.3.1.1. Transparency	142
8.3.1.2. Miscibility and thermal behavior	142
8.3.1.3. Morphology	144
8.3.1.4. Mechanical properties	147
8.3.1.5. Optical properties	151
8.3.1.6. Surface properties	153
<b>8.4. Conclusions</b>	<b>154</b>
<b>8.5. References</b>	<b>155</b>
<b>9. General conclusions, future work and scientific contributions</b>	<b>161</b>
9.1. General conclusions	161
9.2. Future work	161
9.3. Scientific contributions	162
9.3.1. Publications	162
9.3.2. Contributions in conferences	164
9.3.3. Research stays	167
<b>Appendix</b>	<b>169</b>
List of symbols	169
List of abbreviations	170
List of tables	173
List of figures	174

# 1

## Introduction



## 1. Introduction

Nanotechnology is the understanding and control of matter at dimensions of roughly 1 to 100 nanometers, where unique phenomena enable novel applications. The nanoscale is the scale of atoms and molecules, the fundamental building blocks of the material world (**Figure 1.1**).

In many occasions, the fact of making things smaller changes their properties. Many substances behave in a very different way in the world of atoms and molecules. For example, the metal copper is transparent at the nanoscale while gold, which is normally unreactive, becomes chemically very active [1]. In other words, materials can have different physical properties at the nanoscale even though they are still the same materials. At the nanoscale, it is easier for atoms and molecules to move around and between one another, so the chemical properties of materials can also change. Thus, when a particle has nanometric dimensions, properties such as melting point, fluorescence, electrical conductivity, magnetic permeability, and chemical reactivity can change as a function of the size of the particle [2].

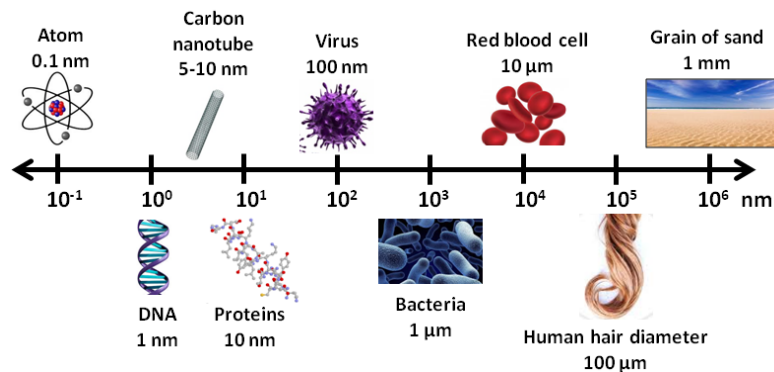


**Figure 1.1.** Some examples of materials in the size range from 0.1 nm to 1 mm.

Moreover, nanoscale materials have much larger surface areas than the same mass of macroscale materials (**Figure 1.2**). When the specific surface area of a material increases, a higher amount of the material can be in contact with the surrounding materials, thus strongly affecting reactivity.

One benefit of the greater surface area and improved reactivity in nanostructured materials is that they have helped to create better catalysts. Nanoengineered batteries, fuel cells, and catalysts can potentially use enhanced reactivity at the nanoscale to produce cleaner, safer, and more affordable modes of

producing and storing energy. Large surface area also makes nanostructured membranes and materials ideal candidates for water treatment, among other uses. It also helps to the functionalization of nanoscale material surfaces for applications ranging from drug delivery to clothing insulation [3].

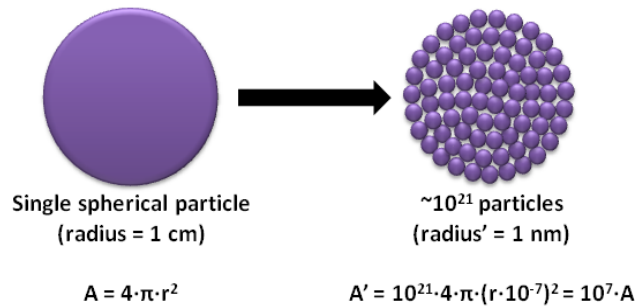


**Figure 1.2.** Illustration to demonstrate the effect of the increased surface area provided by nanomaterials.

As a result of that, nanotechnology is helping to considerably improve, even revolutionize, many technological and industrial sectors, such as: information technology, energy, environmental science, medicine, homeland security, food safety, and transportation, among many others. Some of the fields where nanotechnology can find application are presented in **Figure 1.3**.

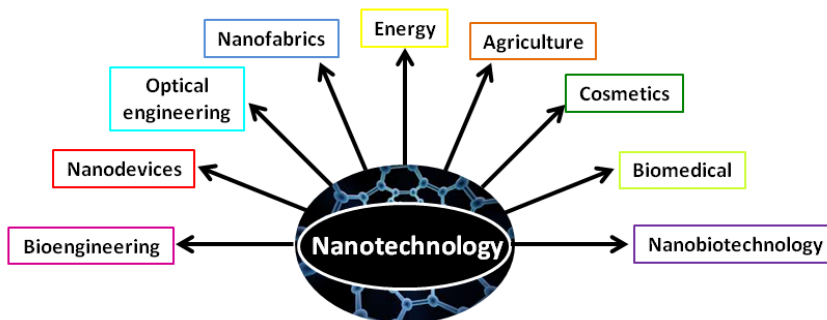


**Figure 1.3.** Various applications of nanotechnology.

### 1.1. Block copolymers

Block copolymers are generally defined as macromolecules that contain two or more different polymer chains which are bound together through covalent bonds [4]. The simplest and most well-studied block copolymer is the diblock copolymer, which consists of two distinct polymer chains covalently attached at a single point. More complicated architectures include triblock copolymers and mixed arm block

copolymers, among others, where three or more polymer chains are covalently attached at a common branching point. Some of these typical block copolymer types are shown in **Figure 1.4**.

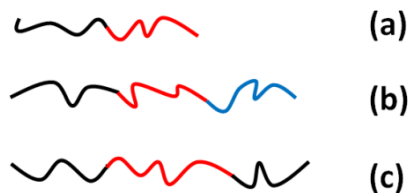


**Figure 1.4.** Schematic representation of some types of linear block copolymers: AB diblock copolymer (a), ABC triblock copolymer (b) and ABA triblock copolymer (c).

The first synthesis of block copolymers was carried out by Bolland and Melville [5] via living macroradicals in 1938. Nevertheless, block copolymers gained great importance after Szwarc et al. synthesized well-defined block copolymers via anionic polymerization in 1956 [6]. Many different synthesis routes are now used to produce a wide variety of block copolymers [7]. In the last years the main advance in block copolymer synthesis was the discovery of living radical polymerization techniques such as atom transfer radical polymerization [8], which allowed the synthesis of many new block copolymer species.

Nowadays the development of block copolymers is closely linked with the advancement of highly controlled living polymerization techniques. Well-defined block copolymers can be synthesized by a wide range of different methods including ionic (cationic [9], anionic [10] or group transfer [11]), radical (atom-transfer radical polymerization (ATRP) [12,13] or reversible addition fragmentation transfer (RAFT) [14]), chain growth polycondensation [15] and metal-catalyzed olefin metathesis [16] techniques, among others. Additionally, supramolecular interactions such as metal-ligand coordination and hydrogen bonding can also be used to prepare block copolymers [17].

### 1.1.1. Phase behavior

Block copolymers have received significant attention over the last few decades due to their ability to self-assemble at the nanometer length scale [18-24] and so to obtain nanostructured structures with controlled morphology both in bulk and in thin

films. This self-assembly is caused by the fact that covalently connected chemically dissimilar polymer blocks phase separate into ordered nanostructures with length scales on the order from 10 to 100 nanometers. Different blocks of the block copolymer tend to separate like it would happen in the case of polymer blends, but in this case the covalent bond between different blocks avoids the macroseparation of the blocks, leading to a microphase separation [18-24].

The phase separation in the block copolymers is governed by the difference in the chemical properties of polymer segments and the length of the polymer, which can be described by the Flory-Huggins interaction parameter ( $\chi$ ) between the two chains and the number of polymer repeating unit or degree of polymerization ( $N$ ), respectively [19,20,22-24]. The interaction parameter indicates the repulsive energy between the two monomers. Thus, the higher the  $\chi$  of the two blocks, the easier the block copolymer will microphase separate. The same occurs with the parameter  $N$ . Therefore, the segregation strength of a given block copolymer system is determined by the product  $\chi \cdot N$ , which must be sufficiently high to occur the spontaneous phase separation. The configurational entropy contribution to the Gibbs energy is proportional to  $N$ . When the product  $\chi \cdot N$  exceeds a critical value  $\chi \cdot N_{ODT}$ , being ODT the order-disorder transition, the block copolymer microphase separates into a periodically ordered structure [23,24].

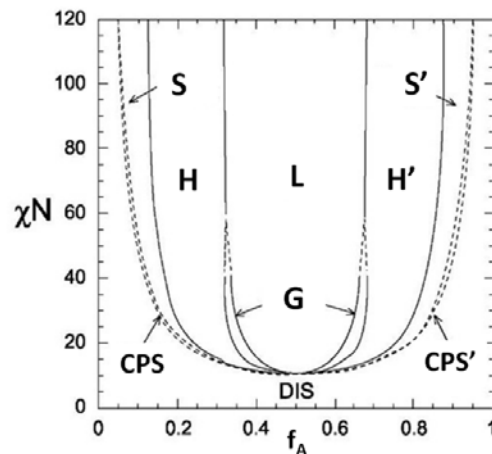


**Figure 1.5.** Theoretical phase diagram of an AB diblock copolymer.

Most studies on block copolymers have focused on diblock copolymers where each block is a fully flexible polymer chain. Therefore, structures generated by these block copolymers are well understood. In general for all diblock copolymers, the

existing different equilibrium morphologies can be completely described by a phase diagram like that shown in **Figure 1.5**, according to the self-consistent mean-field (SCMF) theory [22-25].

The self-assembled domain shapes can be modified by adjusting the relative volume fraction of each block ( $f$ ), Flory-Huggins interaction parameter ( $\chi$ ), and the degree of polymerization ( $N$ ). In a typical block copolymer, the dimension of the domains ranges from 10 nm to 100 nm and this could be controlled by changing the overall molecular weight of the macromolecule. Block copolymer structures described in the phase diagram are the following ones: hexagonally-packed cylinders (H and H'), lamellae (L), double-gyroid phase (G), body-centered spheres (S and S'), close-packed spheres (CPS and CPS') and disordered structure (DIS) [22-25]. These morphologies are also schematically shown in **Figure 1.6** [22].

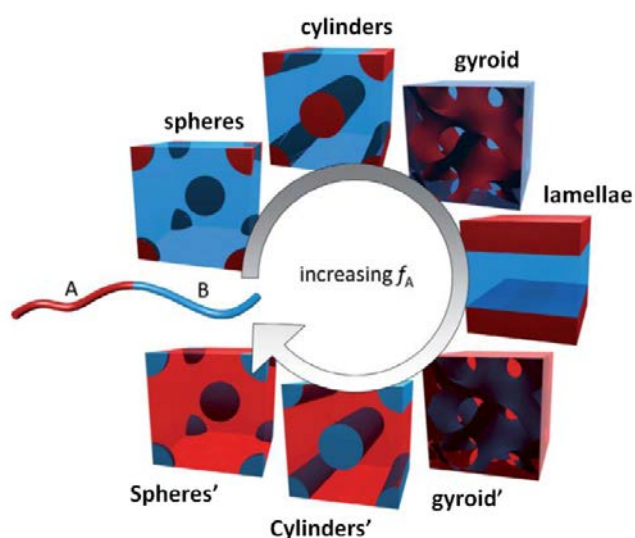


**Figure 1.6.** Equilibrium morphologies of AB diblock copolymers in bulk.

The arrangement of block copolymer morphology can be achieved not only by self-assembly but also by the application of external fields, which can favor the ordering of block copolymers to reach nanostructured morphologies, such as solvent vapor annealing [26-28] mechanical flow [29,30] or electrical field [31,32] among others, that induce an enhanced morphology alignment of the block copolymers. Consequently, block copolymers can be ideal scaffolds or templates to pattern nanoparticles or for fabrication of hybrid structures to be integrated in devices for various electronic, optical and optoelectronic applications.

### 1.1.2. Block copolymers applications

In the solid state, block copolymers can microphase separate to form well-defined self-assembled structures of predictable size [18-24]. The nature of the morphology is dependent on many factors, such as the architecture of the block copolymer, the degree of polymerization of each block, interactions between blocks and the interactions of each block with the environment, as well as sample processing [7].

The material properties of block copolymers come from the physical characteristics of the constituent homopolymer blocks. Consequently, this leads to various combinations of properties, which result in functional materials for a wide range of emerging applications [7,21,22]. Some of these applications will be mentioned here.

One of the main applications of the block copolymers is their use as templates [33,34], since the ability to phase-separate at the nanoscale makes block copolymers perfect for templating other materials by using a top-down approach. One of the strategies for templating is to use block copolymers where one of the phases can be degraded in a controlled way [35,36] and thus obtain nanoporous substrates that, depending on the functionalities of the remaining phase, can be used for applications like the fabrication of hybrid solar cells [37,38].

Block copolymers can also be used for the fabrication of membranes [39], as selective barriers to regulate gas, liquid, or substance transport. The more extended fields of application of block copolymer based membranes are reverse osmosis [40], dialysis [41] and filtration [42] depending to the particle size.

The ability of block copolymers to self-assemble into periodic geometries in the bulk state makes them adequate materials also for the construction of photonic crystals [43]. As a consequence of their ability to allow, prevent, and direct different wavelengths of light, photonic crystals are under investigation for a large range of applications including the use in optoelectronics, lasers, photonic pigments, displays, and reflective coatings.

Organic photovoltaic field also takes advantage of block copolymers for the synthesis of bulk-heterojunction organic photovoltaics [44], which have been

developed to optimize the donor-acceptor interface by increasing the surface area thank to the ability of block copolymers to form thermodynamically stable nanoscale structures.

Thin films where the film thickness is comparable to the domain size of the block copolymer in the bulk state often can show differences in their self-assembled morphologies. The study of thin films for lithography and patterning purposes represents one of the most prominent areas of research for block copolymers [45,46].

Therefore, it can be concluded that nowadays block copolymers are being investigated as promising polymeric materials for a high number of attractive applications. Along this investigation work, on the one hand block copolymers have been used as polymeric matrix templates for the preparation of hybrid inorganic/organic materials by means of the incorporation of inorganic metal nanocrystals. On the other hand, they have also been employed as modifier agents for epoxy based thermosetting matrices.

### 1.1.3. Block copolymer based nanocomposites

Hybrid materials composed of a polymeric matrix and an additive with the characteristic length in the nanometer scale are nowadays one of the most studied areas in the field of polymer composites [47-53]. In general, the properties of a composite created by combining two or more materials mainly depend on the properties of its constituent components. In the particular case of nanocomposites, where the characteristic length scales of the additive material are in the nanometer range, the addition of the nanofiller such as nanoparticles, carbon nanotubes, clays, nanofibers or cellulose nanocrystals, among others, can have a strong effect on the properties of the resulting material, due to the small size of the filler, compared to more conventional ones and consequently to its original and size dependent characteristics, including surface area. Moreover, due to the small size of the filler, certain properties may be modified, while not affecting others, for example, achieving mechanical enhancement while maintaining optical transparency.

The peculiar features of nanomaterials make them very interesting since even when added in a low proportion to the composite matrix, they can achieve a much more

significant enhancement of a specific property than that observed in the case of the use of a material of larger dimension. Namely, nanofillers can significantly improve different properties of the materials into which they are incorporated, such as optical [54-56], electrical [50,57-59], magnetic [60,61], mechanical [49] or thermal [62] properties.

The improvement of these properties is definitely dependent on the microstructure of the nanocomposite. In this regard, the control of the morphology of nanocomposites has gained increasing attention in the last years. Among the different methods to obtain nanostructured nanocomposites with controlled morphology, one of the most employed strategies relies on the use of block copolymers as matrices for nanocomposite materials. Block copolymers are ideal materials for this purpose taking into account their ability to create ordered nanostructures, as explained before.

Three different types of nanofillers can exist, depending on the dimensionality of the nanomaterial, as exhibited in **Figure 1.7**, which lead to different nanocomposites. The nanofiller can be zero-dimensional (dot or sphere shape), one-dimensional (tube or rod shape) or two-dimensional (sheet shape). At least one characteristic dimension of the inclusion must be on the order of the length scale of the block copolymer microstructure (10-100 nm) in order to form a nanocomposite.

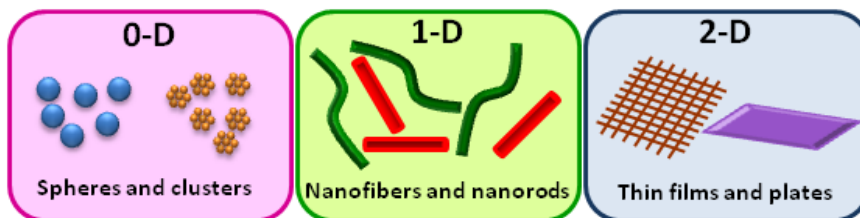


**Figure 1.7.** Different kinds of nanofillers, depending on their shape.

Many studies have reported diverse procedures to somehow direct the nanofillers into a specific phase of a block copolymer and it has been widely proved that the use of block copolymers is a simple way to achieve the desired location of nanofillers in the polymeric matrices determined by the morphology reached by block copolymer self-assembly [57,63-67].

## 1.2. Inorganic nanoparticles

Nowadays there are a high number of materials with characteristic length scales on the order of nanometers. Among the materials with the 3 dimensions at the

nanoscale, we can find nanoparticles, which can be inorganic nanoparticles, organic nanoparticles and hybrid inorganic/organic nanoparticles [68,69]. Inorganic nanoparticles and in particular metal oxide nanoparticles possess interesting properties, which make them attractive as reinforcement of polymeric matrices. As mentioned above, the combination of block copolymers with metal oxide nanoparticles leads to highly ordered nanocomposites with many applications due to the optical, magnetic, electrical, mechanical and thermal properties of inorganic nanoparticles.

The synthesis and characterization of nanoparticles is currently being continuously developed. There are many ways to synthesize metal oxide nanoparticles and can be mainly divided into two categories: top-down approach and bottom-up approach (**Figure 1.8**). In the top-down process [70-73], the bulk materials are used as the starting materials and treated by physical means such as mechanical alloying and sputtering techniques among others to synthesize nanomaterials. The particles synthesized by this method generally have a broad size distribution [71]. Metal oxide nanoparticles synthesized by this method are typically larger and cannot be reproduced resulting in irreproducible catalytic activity. On the other hand, in the bottom-up process [74-76], the single atoms or ions are allowed to grow into clusters or nanoparticles using wet chemical synthesis methods such as chemical reduction of metal salts and the decomposition of precursors using thermal or photochemical treatment. These chemical methods have a good control over the size and shape of the particles and the particles synthesized usually have a narrow size distribution.

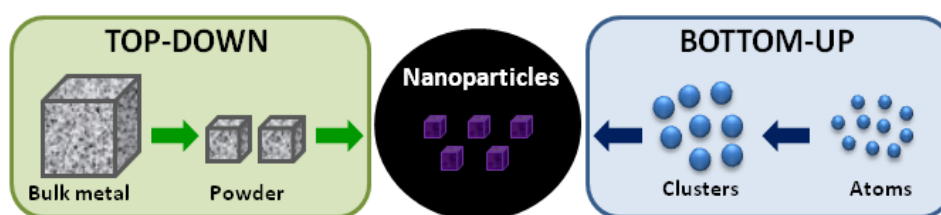


**Figure 1.8.** Top-down and bottom-up approaches for the synthesis of nanoparticles.

Colloidal nanoparticles, which are synthesized by a chemical method, can be highly manipulated. They can be made by chemical reactions in solutions, injected into biological systems, or self-assembled into structures, which may have superior lithographic resolution than can be achieved using top-down fabrication approaches

[77-80]. Additionally, colloidal nanoparticles can be functionalized with small organics or polymers on their surfaces [81,82], which allows to adjust the optical and electronic properties of the inorganic core independently of their surface chemistry.

Colloidal inorganic nanoparticles are attractive materials in biomedical and energy conversion research and they enable applications in drug delivery, imaging contrast agents, photothermal therapies, and sensing applications. Semiconductor nanoparticles (CdSe, ZnSe, ZnS, TiO<sub>2</sub>, ZnO, etc.) can be employed for *in vivo* imaging and contrast agents as well as the development of energy conversion devices like solar cells [83,84]. Insulator nanoparticles (SiO<sub>2</sub>) find application in the development of nanoscale phosphors [85], and mesoporous silica nanoparticles possess functionalized nanoscale pores that can enhance drug delivery applications [86].

#### 1.2.1. Hybrid inorganic/organic nanocomposites

As already explained, the ability to control the length scale and orientational organization of block copolymer morphologies makes these materials particularly attractive as scaffolds or templates for the engineering of nanostructures. Such structures are composed of two continuous substructures, where the minority component forms a connected network within the matrix. These microdomain structures can act as hosts for nanoscopic inclusions of appropriate chemical affinity and geometry.

Two synthetic approaches are employed to create block copolymer based nanocomposite materials. In the first one, the particles are synthesized *in situ* within the block copolymer matrix [87,88] and in the second one the nanocomposite is fabricated by the assembly of the block copolymer and nanoparticles that are previously synthesized *ex situ* [64,89]. The first one depends mainly on the details of reaction and diffusion kinetics of the growing nanocrystals within the targeted polymer domains, whereas the second one does not possess the restrictions of *in situ* chemical pathways for particle synthesis. The *ex situ* procedure involves many factors such as the particle size and shape relative to the size and shape of the host microdomains, polymer chain configuration, particle orientation, and particle-particle as well as particle-polymer interactions.

Therefore, not only the size and shape of the nanoparticles is important but also the interactions between nanoparticles and host polymer. This latter is specially a key point, since unfavorable interactions typically exist between the particle surface and the host polymer. As a result of that, most particles will need to be pretreated or functionalized in order to tailor their surface for compatibilization. The functionalization can be carried out by attaching a polymer chain to the particle surface for example by means of grafting (grafting to, grafting from or grafting through) [59,90,91].

In the case of colloidal nanoparticles, the functionalization can take place during the synthesis resulting in organic ligands coated nanoparticles [81,82,92], with modified surface which make them compatible with the polymeric matrix. In this way, not only nanoparticles will be compatible with the host matrix, but also they can be selectively compatible with one of the microphase of the block copolymer matrix and thus achieve preferential confinement of nanoparticles in a specific block copolymer domain. Surface functionalization is responsible for the chemical affinity between nanoparticles and one block of the block copolymer, therefore this can be exploited to direct the nanoparticles into the target block copolymer domain during the assembling process.

### **1.3. Epoxy based thermosets**

Epoxyes are the most common and widely employed thermosets [93,94]. Their characteristics, which provide a diversity of applications, are explained by the chemistry of the epoxide functional group as well as the curing reaction. The high degree of crosslinking and the nature of the interchain bonds give cured epoxyes many desirable characteristics. These characteristics include excellent adhesion to many substrates, high strength (tensile, compressive and flexural), chemical resistance, fatigue resistance, corrosion resistance and electrical resistance [93,94]. In addition, processing is simplified by the low shrinkage and lack of volatile by-products. Properties of the uncured epoxy resins such as viscosity, which are important in processing, as well as final properties of cured epoxyes such as strength or electrical resistance can be optimized by appropriate selection of the epoxy monomer and the curing agent or catalyst. Owing to the ease of application and desirable properties,

epoxies are widely used for surface coatings, moulds, corrosion protection, electric insulation, fiber reinforced composites, adhesives and aerospace and electronic industries, among others [93-95].

Epoxies are characterized by the presence of one or more epoxide functional groups (**Figure 1.9**) in the polymer chain. The epoxide group is planar, with a three member ring composed of one oxygen and two carbon atoms. Due to the high ring strain, this group is very reactive.

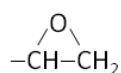


**Figure 1.9.** Epoxide functional group.

The curing process of epoxy resins consists in the reaction of the epoxy groups of the epoxy resin with the functional groups of the same epoxy molecule or with the groups of another reactive compound known as hardener or curing agent [93,96,97]. Amines are one of the most used curing agents [94]. The polymerization and crosslinking in epoxy resins can be of two general types, catalyzed homopolymerization or bridging reactions incorporating a reactive crosslinking agent into the network. The incorporation, or bridging reaction, involves nucleophilic attack on one of the epoxide carbons by an amine (**Figure 1.10**) or an anhydride compound. Reactions shown in **Figure 1.10** illustrate the reaction of the primary amine hydrogen with an epoxy group (a), followed by the secondary amine hydrogen reacting with another epoxy group (b) and the etherification reaction (c) which has to be considered since it is highly favored by the temperature [96-98].

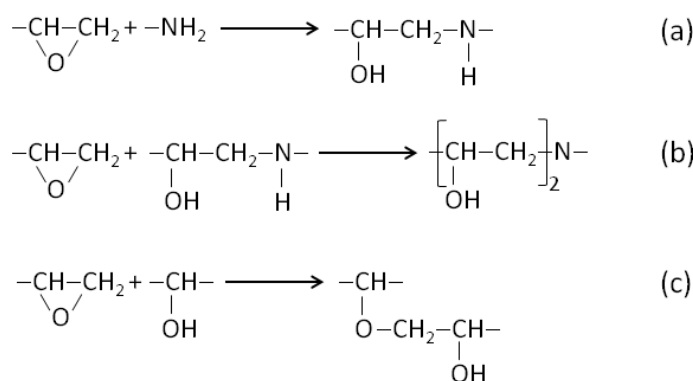


**Figure 1.10.** Reactions which take place during the curing: primary amine hydrogen with an epoxy group (a), secondary amine hydrogen reacting with another epoxy group (b) and etherification reaction (c).

An obvious and important difference in the result of the two different curing methods is that in homopolymerization the network is only composed of the cross-linked epoxy monomers, whereas in the bridging reaction the network is composed of a copolymer of both epoxy monomers and a curing agent [99-101]. Therefore, in a bridging reaction the network properties are a function of two components, which allows modifications to be incorporated in either component.

Epoxy curing involves two phenomena, polymerization and crosslinking [96-98]. During the initial stage of curing, polymerization is favored due to the fact that primary reactions are more reactive than secondary ones, and the terminal epoxide group reactivity is high. The molecular weight of the growing polymer increases until the molecular weight approaches infinity, so that all monomers are connected by at least one bond and a network is formed. At this point, called the gel point, the polymer possesses high molecular weight and some crosslinks, and thus behaves like a very high molecular weight thermoplastic. From the gel point, crosslinking becomes the dominant phenomenon due to the lack of free monomers. The crosslinking reactions produce a growing network and reduce the mobility of the chain segments. The growth of the network results in mechanical and thermal stabilization of the structure, resulting in increasing modulus and glass transition and degradation temperatures. At a certain high degree of crosslinking, the increasing molecular weight of the structure exceeds the molecular weight, which is thermodynamically stable as a rubber, and the material transforms into a glass, in a process called vitrification. In a glassy state, the mobility of reactants is severely restricted, reducing the rate of the reaction to a diffusion-controlled reaction, which is much slower. Further conversion is still possible; however, the rate is much slower since the process relies on diffusion rather than mobility to bring the reactants together. When the crosslinking reaction exhausts all the reactive sites available, the resulting structure is hard and insoluble due to a high degree of interchain bonding [96,102].

#### 1.3.1. Epoxy based thermosetting systems modified with block copolymers

As a result of the high cross-link density achieved during the curing process, these materials tend to be rather brittle having low impact and fracture strengths,

being this their main drawback for some applications. In recent years, many researchers have focused their work on the enhancement of the toughness of the epoxy resins [103,104]. One of the efficient ways to make the epoxy based thermosets tougher is to modify the original epoxy resin by the incorporation of a second phase into the continuous matrix of epoxy based thermoset through physical blending or chemical reactions. The addition of modifiers can convert the epoxy based thermoset into multiphase systems and in the case when the modifier is suitably dispersed through the matrix, the fracture toughness could be significantly increased. Highly cross-linked thermosetting systems have a limited ability to be deformed by shielding, and the incorporation of another component could reduce the cross-linking density, leading to an improved toughness. Many kinds of modifiers have been employed for this purpose, such as thermoplastic homopolymers, block copolymers, liquid rubbers, reactive diluents, inorganic particles, etc [105-107].

Among these materials, many studies have confirmed that block copolymers can provide new or improved properties to the epoxy resins [108-115]. The main contribution of the block copolymers is their capacity to self-assemble in ordered nanostructures leading to microphase separated morphologies and to generate nanostructured thermosetting systems when they are mixed with an epoxy resin. Beside the ability to get ordered nanostructures with different morphologies, the addition of block copolymers to thermosetting matrices can lead to an improvement in the mechanical properties of the matrix.

One of the approaches to achieve nanostructured morphology by mixing with a block copolymer requires a block of the block copolymer to be immiscible with the thermosetting system and another block to be miscible with it up to high contents. Depending on the solubility of the different blocks of the block copolymer, the self-assembly of the block copolymer can take place before curing leading to the microphase separation [108], or during the curing reaction, by a mechanism known as reaction induced phase separation (RIPS) [116] where one of the blocks undergoes phase separation as the polymerization reaction proceeds due to the increasing immiscibility with the thermosetting matrix.

In general, epoxy thermosetting systems modified with a block copolymer can have two behaviors in terms of the phase separation phenomenon and the influence

of the temperature. One of them is the upper critical solution temperature (UCST), where the miscibility would occur when increasing the temperature and the second one is the lower critical solution temperature (LCST), where the miscibility increases when the temperature decreases.

Some of the block copolymers most commonly used in literature for the toughening of thermosetting systems have been poly(ethylene oxide)-*b*-poly(ethylene-*alt*-propylene) (PEO-*b*-PEP) [117], poly(ethylene oxide)-*b*-poly(propylene oxide)-*b*-poly(ethylene oxide) (PEO-*b*-PPO-*b*-PEO) [118], polystyrene-*b*-polybutadiene (PS-*b*-PB) [119], and polystyrene-*b*-polybutadiene-*b*-poly-(methyl methacrylate) (PS-*b*-PB-*b*-PMMA) [120], among others. In general, the most widely employed epoxy miscible blocks for this purpose have been poly(ethylene oxide) and poly(methyl methacrylate).

#### 1.4. References

- [1] S. K. Gupta, *Krishan's Engineering Physics II*, Krishna Prakashan Media (P) Ltd., Meerut (India), 2001.
- [2] G. A. Mansoori, *Principles of Nanotechnology: Molecular-based study of condensed matter in small systems*, World Scientific Publishing Co. Pte. Ltd., Singapore (Singapore), 2005.
- [3] S. Logothetidis, *Nanostructured materials and their applications*, Springer-Verlag, Berlin (Germany), 2012.
- [4] N. Hadjichristidis, S. Pispas, G. Floudas, *Block Copolymers. Synthetic Strategies, Physical Properties and Applications*, John Wiley & Sons, New Jersey (USA), 2003.
- [5] J. H. Bolland, H. W. Melville, *Proceedings of the First Rubber Technology Conference*, W. Heffer and Sons, London (United Kingdom), 1938.
- [6] M. Szwarc, M. Levy, R. Milkovich, *J. Am. Chem. Soc.* 1956, **78**, 2656-2657.
- [7] F. H. Schacher, P. A. Rupar, I. Manners, *Angew. Chem. Int. Ed.* 2012, **51**, 7898-7921.
- [8] K. A. Davis, K. Matyjaszewski, *Macromolecules* 2001, **34**, 2101-2107.
- [9] S. Aoshima, S. Kanaoka, *Chem. Rev.* 2009, **109**, 5245-5287.
- [10] M. Szwarc, *Nature* 1956, **178**, 1168-1169.
- [11] O. W. Webster, W. R. Hertler, D. Y. Sogah, W. B. Farnham, T. V. RajanBabu, *J. Am. Chem. Soc.* 1983, **105**, 5706-5708.

- [12] M. Ouchi, T. Terashima, M. Sawamoto, *Chem. Rev.* 2009, **109**, 4963-5050.
- [13] J. S. Wang, K. Matyjaszewski, *J. Am. Chem. Soc.* 1995, **117**, 5614-5615.
- [14] A. B. Lowe, C. L. McCormick, *Prog. Polym. Sci.* 2007, **32**, 283-351.
- [15] A. P. Soto, I. Manners, *Macromolecules* 2009, **42**, 40-42.
- [16] A. Leitgeb, J. Wappel, C. Slugovc, *Polymer* 2010, **51**, 2927-2946.
- [17] A. O. Moughton, R. K. O'Reilly, *Macromol. Rapid Commun.* 2010, **31**, 37-52.
- [18] G. Riess, *Prog. Polym. Sci.* 2003, **28**, 1107-1170.
- [19] I. W. Hamley, *Nanotechnology* 2003, **14**, R39-R54.
- [20] S. B. Darling, *Prog. Polym. Sci.* 2007, **32**, 1152-1204.
- [21] I. W. Hamley, *Prog. Polym. Sci.* 2009, **34**, 1161-1210.
- [22] Y. C. Tseng, S. B. Darling, *Polymers* 2010, **2**, 470-489.
- [23] Y. Mai, A. Eisenberg, *Chem. Soc. Rev.* 2012, **41**, 5969-5985.
- [24] H. Hu, M. Gopinadhan, C. O. Osuji, *Soft Matter* 2014, **10**, 3867-3889.
- [25] M. W. Matsen, F. S. Bates, *Macromolecules* 1996, **29**, 1091-1098.
- [26] J. Gutierrez, A. Tercjak, I. Garcia, I. Mondragon, *Nanotechnology* 2009, **20**, 225603/1-225603/9.
- [27] E. Metwalli, J. Perlich, W. Wang, A. Diethert, S. V. Roth, C. M. Papadakis, P. Müller-Buschbaum, *Macromol. Chem. Phys.* 2010, **211**, 2102-2108.
- [28] S. S. Dinachali, W. Bai, K. H. Tu, H. K. Choi, J. Zhang, M. E. Kreider, L. C. Cheng, C. A. Ross, *ACS Macro Lett.* 2015, **4**, 500-504.
- [29] D. E. Angelescu, J. H. Waller, R. A. Register, P. M. Chaikin, *Adv. Mater.* 2005, **17**, 1878-1881.
- [30] S. Sakurai, *Polymer* 2008, **49**, 2781-2796.
- [31] A. Böker, H. Elbs, H. Hänsel, A. Knoll, S. Ludwigs, H. Zettl, A. V. Zvelindovsky, G. J. A. Sevink, V. Urban, V. Abetz, A. H. E. Müller, G. Krausch, *Macromolecules* 2003, **36**, 8078-8087.
- [32] M. Ruppel, C. W. Pester, K. M. Langner, G. J. Sevink, H. G. Schoberth, K. Schmidt, V. S. Urban, J. W. Mays, A. Böker, *ACS Nano* 2013, **7**, 3854-3867.
- [33] J. Gutierrez, I. Mondragon, A. Tercjak, *Macromol. Symp.* 2012, **321-322**, 99-104.
- [34] L. Zhu, H. Tran, F. L. Beyer, S. D. Walck, X. Li, H. Agren, K. L. Killops, L. M. Campos, *J. Am. Chem. Soc.* 2014, **136**, 13381-13387.
- [35] M. A. Hillmyer, *Adv. Polym. Sci.* 2005, **190**, 137-181.

- [36] S. Krishnamoorthy, C. Hinderling, H. Heinzelmann, *Mater. Today* 2006, **9**, 40-47.
- [37] M. C. Orilall, U. Wiesner, *Chem. Soc. Rev.* 2011, **40**, 520-535.
- [38] A. Sarkar, N. J. Jeon, J. H. Noh, S. I. Seok, *J. Phys. Chem. C* 2014, **118**, 16688-16693.
- [39] E. A. Jackson, M. A. Hillmyer, *ACS Nano* 2010, **4**, 3548-3553.
- [40] J. S. Louie, I. Pinnau, I. Ciobanu, K. P. Ishida, A. Ng, M. Reinhard, *J. Membrane Sci.* 2006, **280**, 762-770.
- [41] X. Qiu, H. Yu, M. Karunakaran, N. Pradeep, S. P. Nunes, K. V. Peinemann, *ACS Nano* 2013, **7**, 768-776.
- [42] H. Ahn, S. Park, S. W. Kim, P. J. Yoo, D. Y. Ryu, T. P. Russell, *ACS Nano* 2014, **8**, 11745-11752.
- [43] O. B. Ayyub, M. B. Ibrahim, R. M. Briber, P. Kofinas, *Biosens. Bioelectron.* 2013, **46**, 124-129.
- [44] K. Yuan, L. Chen, Y. Chen, *Polym. Int.* 2014, **63**, 593-606.
- [45] C. Tang, E. M. Lennon, G. H. Fredrickson, E. J. Kramer, C. J. Hawker, *Science* 2008, **322**, 429-432.
- [46] A. Nunns, J. Gwyther, I. Manners, *Polymer* 2013, **54**, 1269-1284.
- [47] B. N. Jang, D. Wang, C. A. Wilkie, *Macromolecules* 2005, **38**, 6533-6543.
- [48] A. Tercjak, J. Gutierrez, C. J. Ocando, L. Peponi, I. Mondragon, *Acta Mater.* 2009, **57**, 4624-4631.
- [49] A. Tercjak, J. Gutierrez, L. Peponi, L. Rueda, I. Mondragon, *Macromolecules* 2009, **42**, 3386-3390.
- [50] A. Tercjak, J. Gutierrez, I. Mondragon, *J. Phys. Chem. C* 2011, **115**, 1643-1648.
- [51] D. Kim, S. Srivastava, S. Narayanan, L. A. Archer, *Soft Matter* 2012, **8**, 10813-10818.
- [52] M. Mutz, D. W. Holley, D. Baskaran, J. W. Mays, M. D. Dadmun, *Polymer* 2012, **53**, 5087-5096.
- [53] T. Nardi, M. Sangermano, Y. Leterrier, P. Allia, P. Tiberto, J. A. E. Manson, *Polymer* 2013, **54**, 4472-4479.
- [54] J. L. Martinez-Hurtado, *Nanomaterials* 2011, **1**, 20-30.
- [55] J. Gutierrez, I. Mondragon, A. Tercjak, *Polymer* 2011, **52**, 5699-5707.
- [56] W. C. Yen, Y. H. Lee, J. F. Lin, C. A. Dai, U. S. Jeng, W. F. Su, *Langmuir* 2011, **27**, 109-115.

- [57] A. Tercjak, J. Gutierrez, C. J. Ocando, L. Peponi, I. Mondragon, *Acta Mater.* 2009, **57**, 4624-4631.
- [58] J. Gutierrez, A. Tercjak, I. Mondragon, *J. Am. Chem. Soc.* 2010, **132**, 873-878.
- [59] H. Etxeberria, A. Tercjak, I. Mondragon, A. Eceiza, G. Kortaberria, *Colloid Polym. Sci.* 2014, **292**, 229-234.
- [60] I. Garcia, A. Tercjak, L. Rueda, I. Mondragon, *Macromolecules* 2008, **41**, 9295-9598.
- [61] L. G. Bach, R. Islam, J. T. Kim, S. Y. Seo, K. T. Lim, *Appl. Surf. Sci.* 2012, **258**, 2959-2966.
- [62] E. Ayandele, B. Sarkar, P. Alexandridis, *Nanomaterials* 2012, **2**, 445-475.
- [63] T. Thurn-Albrecht, R. Steiner, J. DeRouchey, C. M. Stafford, E. Huang, M. Bal, M. Tuominen, C. J. Hawker, T. P. Russell, *Adv. Mater.* 2000, **12**, 787-791.
- [64] M. R. Bockstaller, R. A. Mickiewicz, E. L. Thomas, *Adv. Mater.* 2005, **17**, 1331-1349.
- [65] W. H. Binder, C. Kluger, C. J. Straif, G. Friedbacher, *Macromolecules* 2005, **38**, 9405-9410.
- [66] A. Haryono, W. H. Binder, *Small* 2006, **2**, 600-611.
- [67] M. Luo, T. H. Epps, *Macromolecules* 2013, **46**, 7567-7579.
- [68] S. Kango, S. Kalia, A. Celli, J. Njuguna, Y. Habibi, R. Kumar, *Prog. Polym. Sci.* 2013, **38**, 1232-1261.
- [69] K. Li, B. Liu, *Chem. Soc. Rev.* 2014, **43**, 6570-6597.
- [70] B. X. Chung, C. P. Liu, *Mater. Lett.* 2004, **58**, 1437-1440.
- [71] V. Bouchat, O. Feron, B. Gallez, B. Masereel, C. Michiels, T. V. Borghet, S. Lucas, *Surf. Coat. Tech.* 2011, **205**, S577-S581.
- [72] P. Asanithi, S. Chaiyakun, P. Limsuwan, *J. Nanomater.* 2012, 2012, 963609/1-963609/8.
- [73] S. Suzuki, T. Suzuki, Y. Tomita, M. Hirano, K. Okazaki, S. Kuwabata, T. Torimoto, *CrystEngComm* 2012, **14**, 4922-4926.
- [74] Y. Li, J. Liu, Y. Wang, Z. L. Wang, *Chem. Mater.* 2001, **13**, 1008-1014.
- [75] V. Logvinenko, O. Polunina, Y. Mikhailov, K. Mikhailov, B. Bokhonov, *J. Therm. Anal. Calorim.* 2007, **90**, 813-816.
- [76] M. G. Guzmán, J. Dille, S. Godet, *Int. J. Chem. Biomol. Eng.* 2009, **2**, 104-111.
- [77] M. De, P. S. Ghosh, V. M. Rotello, *Adv. Mater.* 2008, **20**, 4225-4241.

- [78] R. Sardar, A. M. Funston, P. Mulvaney, R. W. Murray, *Langmuir* 2009, **25**, 13840-13851.
- [79] J. I. Cutler, E. Auyeung, C. A. J. Mirkin, *J. Am. Chem. Soc.* 2012, **134**, 1376-1391.
- [80] S. E. Lohse, C. J. Murphy, *J. Am. Chem. Soc.* 2012, **134**, 15607-15620.
- [81] P. D. Cozzoli, A. Kornowski, H. Weller, *J. Am. Chem. Soc.* 2003, **125**, 14539-14548.
- [82] A. Convertino, M. Tamborra, M. Striccoli, G. Leo, A. Agostiano, M. L. Curri, *Thin Solid Films* 2011, **519**, 3931-3938.
- [83] H. Goesmann, C. Feldmann, *Angew. Chem. Int. Ed.* 2010, **49**, 1362-1395.
- [84] T. Froschl, U. Hormann, P. Kubiak, G. Kucerova, M. Pfanzelt, C. K. Weiss, R. J. Behm, N. Husing, U. Kaiser, K. Landfester, M. Wohlfahrt-Mehrens, *Chem. Soc. Rev.* 2012, **41**, 5313-5360.
- [85] K. Chang, X. Men, H. Chen, Z. Liu, S. Yin, W. Qin, Z. Yuan, C. Wu, *J. Mater. Chem. C* 2015, **3**, 7281-7285.
- [86] Y. Wang, Q. Zhao, N. Han, L. Bai, J. Li, J. Liu, E. Che, L. Hu, Q. Zhang, T. Jiang, S. Wang, *Nanomed.: Nanotech. Biol. Med.* 2015, **11**, 313-327.
- [87] T. Tang, M. J. Krysmann, I. W. Hamley, *Colloid. Surface A* 2008, **317**, 764-767.
- [88] Y. H. Lee, C. J. Chang, C. J. Kao, C. A. Dai, *Langmuir* 2010, **36**, 4196-4206.
- [89] M. A. Hood, M. Mari, R. Muñoz-Espí, *Materials* 2014, **7**, 4057-4087.
- [90] B. Mu, T. Wang, Z. Wu, H. Shi, D. Xue, P. Liu, *Colloid. Surface A* 2011, **375**, 163-168.
- [91] S. T. Hailu, S. Samant, C. Grabowski, M. Durstock, A. Karim, D. Raghavan, *J. Polym. Sci. A1* 2015, **53**, 468-478.
- [92] N. Depalo, P. Carrieri, R. Comparelli, M. Striccoli, A. Agostiano, L. Bertinetti, C. Innocenti, C. Sangregorio, M. L. Curri, *Langmuir* 2011, **27**, 6962-6970.
- [93] D. Ratna, *Handbook of thermoset resins*, iSmithers, Shrewsbury (United Kingdom), 2009.
- [94] F. L. Jin, X. Li, S. J. Park, *J. Ind. Eng. Chem.* 2015, **29**, 1-11.
- [95] S. Deng, L. Djukic, R. Paton, L. Ye, *Composites, Part A* 2015, **68**, 121-132.
- [96] B. Bilyeu, W. Brostow, K. P. Menard, *J. Mater. Educ.* 1999, **21**, 281-286.
- [97] A. Bonnet, J. P. Pascault, H. Sautereau, M. Taha, *Macromolecules* 1999, **32**, 8517-8523.
- [98] G. Nikolic, S. Zlatkovic, M. Cakic, S. Cakic, C. Lacnjevac, Z. Rajic, *Sensors* 2010, **10**, 684-696.
- [99] S. J. Park, H. J. Jeong, C. Nah, *Mater. Sci. Eng. A* 2004, **385**, 13-16.

- [100] S. J. Park, F. L. Jin, J. R. Lee, J. S. Shin, *Eur. Polym. J.* 2005, **41**, 231-237.
- [101] H. R. Jeon, J. H. Park, M. Y. Shon, *J. Ind. Eng. Chem.* 2013, **19**, 849-853.
- [102] J. K. Gillham, *Polym. Eng. Sci.* 1986, **26**, 1429-1433.
- [103] L. Ruiz-Pérez, G. J. Royston, J. P. A. Fairclough, A. J. Ryan, *Polymer* 2008, **49**, 4475-4488.
- [104] N. Domun, H. Hadavinia, T. Zhang, T. Sainsbury, G. H. Liaghat, S. Vahid, *Nanoscale* 2015, **7**, 10294-10329.
- [105] J. H. Park, S. C. Jana, *Polymer* 2003, **44**, 2091-2100.
- [106] M. R. Dadfar, F. Ghadami, *Mater. Design* 2013, **47**, 16-20.
- [107] A. J. Kinloch, S. H. Lee, A. C. Taylor, *Polymer* 2014, **55**, 6325-6334.
- [108] M. A. Hillmyer, P. M. Lipic, D. A. Hajduk, K. Almdal, F. S. Bates, *J. Am. Chem. Soc.* 1997, **119**, 2749-2750.
- [109] E. Girard-Reydet, H. Sautereau, J. P. Pascault, *Polymer* 1999, **40**, 1677-1687.
- [110] R. B. Grubbs, J. M. Dean, F. S. Bates, *Macromolecules* 2001, **34**, 8593-8595.
- [111] E. Serrano, A. Tercjak, G. Kortaberria, J. A. Pomposo, D. Mecerreyes, N. E. Zafeiropoulos, M. Stamm, I. Mondragon, *Macromolecules* 2006, **39**, 2254-2261.
- [112] S. Maiez-Tribut, J. P. Pascault, E. R. Soulé, J. Borrajo, R. J. J. Williams, *Macromolecules* 2007, **40**, 1268-1273.
- [113] J. Gutierrez, A. Tercjak, I. Mondragon, *J. Phys. Chem. C* 2010, **114**, 22424-22430.
- [114] A. Tercjak, J. Gutierrez, M. D. Martin, I. Mondragon, *Eur. Polym. J.* 2012, **48**, 16-25.
- [115] C. Declet-Perez, L. F. Francis, F. S. Bates, *Macromolecules* 2015, **48**, 3672-3684.
- [116] R. B. Grubbs, J. M. Dean, M. E. Broz, F. S. Bates, *Macromolecules* 2000, **33**, 9522-9534.
- [117] J. M. Dean, P. M. Lipic, R. B. Grubbs, R. F. Cook, F. S. Bates, *J. Polym. Sci., Part B: Polym. Phys.* 2001, **39**, 2996-3010.
- [118] M. Larrañaga, E. Serrano, M. D. Martin, A. Tercjak, G. Kortaberria, K. de la Caba, C. C. Riccardi, I. Mondragon, *Polym. Int.* 2007, **56**, 1392-1403.
- [119] C. Ocando, A. Tercjak, M. D. Martin, J. A. Ramos, M. Campo, I. Mondragon, *Macromolecules* 2009, **42**, 6215-6224.
- [120] S. Ritzenthaler, F. Court, E. Girard-Reydet, L. Leibler, J. P. Pascault, *Macromolecules* 2003, **36**, 118-126.

# 2

## Characterization techniques



## 2. Characterization techniques

The characterization techniques employed along this thesis will be described in this Chapter. The experimental procedures as well as characterization techniques conditions will be detailed in the following Chapters.

### 2.1. Physico-chemical characterization

#### 2.1.1. X-ray diffraction (XRD)

XRD analysis is based on the constructive interference of monochromatic X-rays and a sample. The X-rays are generated by a cathode ray tube, filtered to produce monochromatic radiation, and directed toward the sample. The interaction of the incident rays with the sample produces constructive interference and a diffracted ray when conditions satisfy Bragg's law [1,2]. This law relates the wavelength of the electromagnetic radiation to the diffraction angle and the lattice spacing in a crystalline sample.

The characteristic x-ray diffraction pattern generated in a typical XRD analysis provides a unique fingerprint of the crystals present in the sample. When properly interpreted, by comparison with standard reference patterns and measurements, this fingerprint allows the identification of the crystalline form.

#### 2.1.2. Fourier transform infrared spectroscopy (FTIR)

FTIR is based on the fact that most molecules absorb light in the infrared region of the electromagnetic spectrum. IR radiation is passed through a sample. Some of the infrared radiation is absorbed by the sample and some of it is passed through. Generally the absorption corresponds to the bonds present in the molecule. The resultant absorption spectrum from the bond natural vibration frequencies indicates the presence of various chemical bonds and functional groups present in the sample [3]. Thus, this technique is particularly useful for the identification of organic molecular groups and compounds due to the range of functional groups, side chains and cross-links involved, all of which have characteristic vibrational frequencies in the infrared range. The frequency range is measured as wavenumbers typically over the range 4000-600  $\text{cm}^{-1}$ .

## **2.2. Thermal characterization**

### **2.2.1. Differential scanning calorimeter (DSC)**

DSC is a technique in which the difference in the amount of heat required to increase the temperature of a sample and a reference is measured as a function of temperature or time [4]. Both the sample and reference are maintained at nearly the same temperature throughout the experiment. While heating or cooling, when the sample undergoes an endothermic or exothermic physical transformation such as phase transitions, controlled heat will be needed to flow to it to maintain both the sample and the reference at the same temperature. For example, this would be due to the absorption of heat by the sample as it undergoes the endothermic phase transition from solid to liquid. By observing the difference in heat flow between the sample and reference, differential scanning calorimeter is able to measure the amount of heat absorbed or released during such transitions. The main application of DSC is in studying phase transitions, such as melting, glass transitions, or even in studying polymer curing.

## **2.3. Morphological characterization**

### **2.3.1. Atomic force microscopy (AFM)**

AFM works by scanning the sample surface using a very sharp tip, typically less than 5  $\mu\text{m}$  long and often less than 10 nm in diameter, along the sample surface, carefully maintaining the force between the probe and surface at a set level [5,6]. Usually, the tip is located at the free end of a cantilever, and the deflection or vertical bending of the cantilever due to interaction forces mainly consisting of Van der Waals interactions, short-range repulsive interactions and adhesion and capillary forces [7] acting on the tip is detected by a laser focused on the back of the cantilever, as shown in **Figure 2.1**. A light beam from the laser diode bounces off the back of the cantilever and onto a quad photo-detector, which consists of four independent segments. As the cantilever bends, the position of the laser beam on the detector changes.

When a laser spot shines on the photo-detector, each segment generates a voltage signal, proportional to the amount of laser light on that particular segment.

When the cantilever slightly bends upward due to a tip-sample interaction force change, the cantilever changes slightly its angle, consequently the laser spot position on the photo-detector will change.

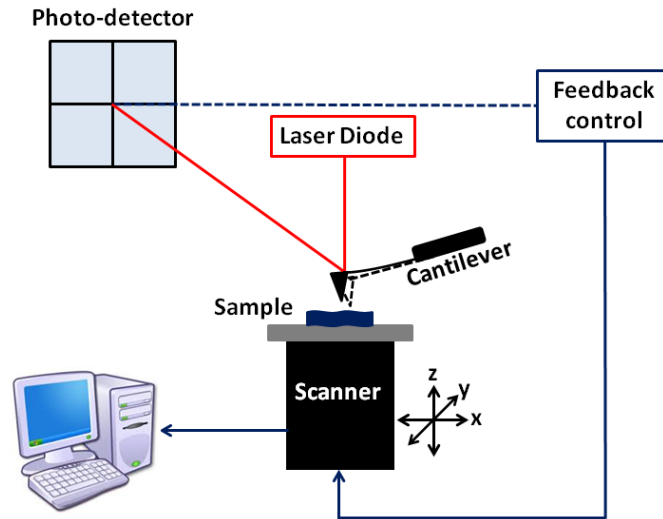


**Figure 2.1.** Schematic illustration of the AFM tapping mode operation.

The movement of the probe over the surface is controlled by a scanner. This is normally made from a piezoelectric material, which can move the probe very precisely in the  $x$ ,  $y$ , and  $z$  axes. The signal from the photo-detector passes through a feedback circuit, and goes into the  $z$ -movement part of the scanner. During the scanning the  $z$ -piezo moves up and down to maintain the set point deflection signal. This distance provides the topography information. Height and phase images are collected simultaneously, where height image indicates the topography of the sample and phase image the material properties like elasticity and adhesion. AFM can operate in contact, tapping or noncontact modes [7]. In tapping mode (TM-AFM), the tip of the probe oscillates very close to the sample (distance between tip-sample  $<150$  nm), and moves completely away from the sample in each oscillation cycle. This is often the most stable mode to use in air, and so is currently more commonly used than either noncontact or contact modes for most applications.

### 2.3.2. Transmission electron microscopy (TEM)

TEM uses high energy electrons which are accelerated to nearly the speed of light. The beam of electrons from the electron gun is restricted by the condenser

aperture, which excludes high angle electrons. The beam passes through the thin sample and part of it is transmitted depending of the thickness and electron transparency of the sample [8]. This transmitted portion is focused by the objective lens into an image on phosphor screen or charge coupled device camera. The image then passed down the column through the intermediate and projector lenses, is enlarged all the way. The darker areas of the image represent those areas of the sample where fewer electrons are transmitted through while the lighter areas of the image represent those areas of the sample that more electrons were transmitted through.

The imaging mode provides a highly magnified view of the micro- and nanostructure. In the high resolution imaging mode, quantum dots quality, shape, size and density can be analyzed.

### **2.3.3. Scanning electron microscopy (SEM)**

In a SEM, the sample is exposed to a focused beam of high-energy electrons, which rapidly moves over or scans the surface of the specimen. This causes the release of a shower of secondary electrons and other types of radiations such as backscattered electrons, diffracted backscattered electrons, photons, visible light and heat, from the specimen surface [8]. Secondary electrons and backscattered electrons are commonly used for imaging samples, secondary electrons are most valuable for showing morphology and topography of samples and backscattered electrons are most valuable for illustrating contrasts in composition in multiphase samples.

The intensity of the secondary electrons depends on the shape and the chemical composition of the irradiated sample. These electrons are collected by a detector, which generates electronic signals. These signals are scanned in the manner of a television system to produce an image on a cathode ray tube. The image is recorded by capturing it from the cathode ray tube.

The signals that derive from electron-sample interactions reveal information about the sample including external morphology, chemical composition and crystalline structure and orientation of materials making up the sample.

## 2.4. Conductive characterization

### 2.4.1. Electrostatic force microscopy (EFM)

EFM maps conductive properties on a sample surface by measuring the local electrostatic interactions between the surface and a biased AFM cantilever. EFM applies a voltage between the tip and the sample while the cantilever moves above the surface, in the Lift Mode, in which the tip is raised. The cantilever is vibrated near its resonant frequency by a small piezoelectric element. The cantilever resonant frequency changes and it deflects when it scans over static charges, proportionally to the charge density. Attractive forces reduce the cantilever resonant frequency, whereas repulsive forces increase the resonant frequency, as can be seen in **Figure 2.2**. Thus, the cantilever resonance frequency and phase change with the strength of the electric field gradient and are used to construct the EFM image [6].

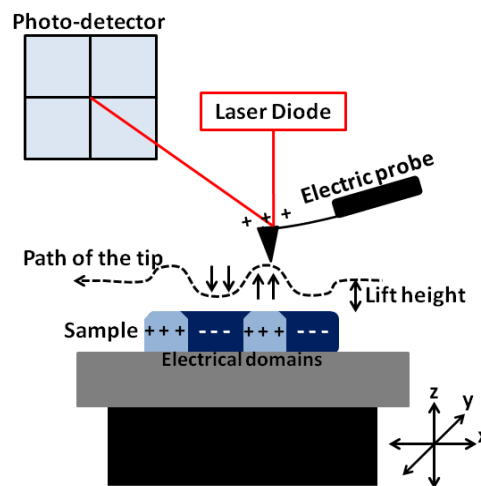


**Figure 2.2.** Schematic illustration of the EFM operation.

EFM images contain qualitative information about conductive properties such as the surface potential and charge distribution of a sample surface and maps locally charged domains on the sample surface. This technique is used to distinguish conductive and insulating regions in a sample.

### 2.4.2. PeakForce tunneling atomic force microscopy (TUNA)

PeakForce TUNA mode consists in PeakForce tapping mode, where the probe and sample are intermittently brought into contact while the tip is scanned across the sample. This eliminates lateral forces during imaging.

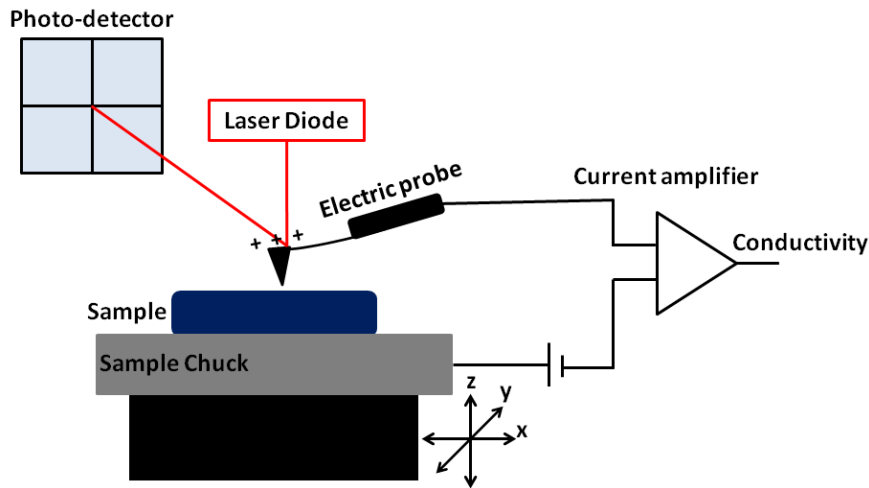


**Figure 2.3.** Schematic illustration of the PeakForce TUNA operation.

An electrically conductive probe is scanned over the sample surface in PeakForce Tapping mode as the feedback loop keeps the maximum force applied on the tip at a constant value by adjusting the extension of the Z piezo. This protects the tip and sample from damage while allowing the tip-sample contact area to be minimized. During scanning, a direct current bias between the tip and the sample can be applied, as seen in **Figure 2.3** [6]. The TUNA module, a high-bandwidth linear current amplifier, detects quantitatively the resulting current passing through the sample. This data is presented simultaneously with the topography image, enabling the direct correlation of local topography with conductive properties. The observed current can be used as a measure of the local conductivity or electrical integrity of the sample under study.

### 2.4.3. Keithley semiconductor analyzer

Keithley semiconductor analyzer is a modular, fully integrated parameter analyzer that performs electrical characterization of materials, semiconductor devices and processes. There are more than one modes of working, which will give different information about the characterized sample [9].

The current-voltage (I-V) curve can be generated by the two-point mode of the semiconductor analyzer, which is able to source and measure both current and voltage between the two probes. I-V curve is useful to know the relationship between the current flowing through an electronic device and the applied voltage across its terminals. On the other hand, to measure the sheet resistivity, the four-point collinear probe mode can be used. In this mode, two of the probes (outer ones) are used to

source current and the other two probes (inner ones) are used to measure the resulting voltage drop across the surface of the sample. These two different modes are shown in **Figure 2.4**.

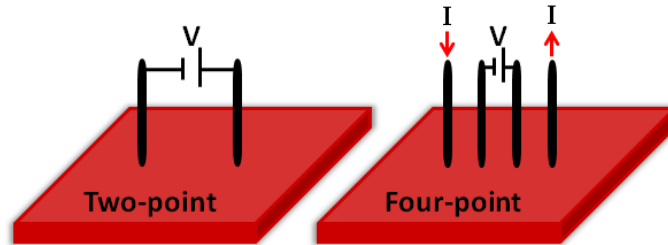


**Figure 2.4.** Schematic illustration of the two-point mode and four-point collinear probe mode.

Sheet resistivity obtained directly from the latter mode allows to easily calculate the electrical resistivity as well as the electrical conductivity by using the following equations, where  $R_s$  is the sheet resistivity ( $\Omega/\text{sq}$ ),  $\rho$  the electrical resistivity ( $\Omega\cdot\text{cm}$ ),  $t$  the thickness (cm) and  $\sigma$  the electrical conductivity (S/cm):

$$\rho = R_s \cdot t$$

$$\sigma = 1/\rho$$

## 2.5. Magnetic characterization

### 2.5.1. Magnetic force microscopy (MFM)

MFM is a technique that employs the same working principle as EFM, but in terms of magnetic properties. It images the spatial variation of magnetic field within the sample surface, through measuring local magnetic interaction between a magnetic tip and a sample [6,10].

In MFM a magnetic tip coated with a ferromagnetic thin film is magnetized and moves above the surface sample, in the Lift Mode. As the tip moves over a magnetic field gradient, it is either pulled toward or repulsed away from the sample, depending on the magnetic moment direction of the sample, as observed in **Figure 2.5**. This deflection of the cantilever or change in the resonant frequency is proportional to the magnetic field strength and can be measured in order to construct the MFM image. Thus, MFM can be used to evaluate qualitatively magnetic materials and devices or to locate and map magnetic defects on a variety of materials and surfaces.

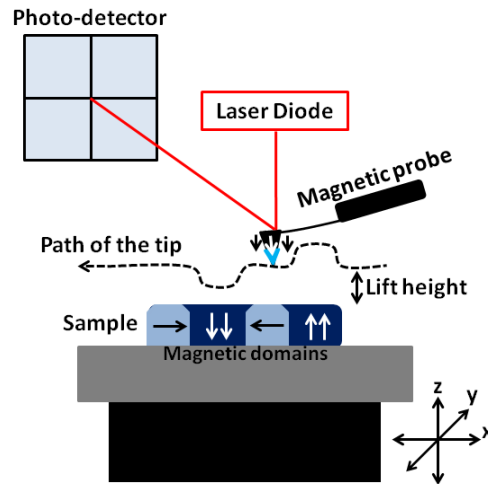


**Figure 2.5.** Schematic illustration of the MFM operation.

## 2.6. Mechanical characterization

### 2.6.1. PeakForce Quantitative nanomechanical measurements (QNM)

PeakForce QNM is a technique which works in a similar way as the PeakForceTUNA technique explained above, by employing the PeakForce tapping mode. In this case, it maps and distinguishes between nanomechanical properties, including modulus and adhesion [6]. QNM is able to acquire and analyze the individual force curves from each tip-sample interaction (usually van der Waals, electrostatic or capillary forces) that occurs during the imaging process. The curves are analyzed in real-time to obtain quantitative mechanical properties of the sample, including adhesion, modulus, deformation, and dissipation. These material property maps can be displayed and analyzed together with topography. PeakForce QNM operates over an extremely wide range, approximately from 1 MPa to 50 GPa for modulus and from 10 pN to 10  $\mu$ N for adhesion, enabling characterization of a large variety of nanoscale materials.

### 2.6.2. Materials testing system (MTS)

The mechanical properties at macroscale are measured by means of flexural test and fracture toughness test. Three-point bending method was used for both tests. For the flexural test the specimens were rectangular whereas for the toughness fracture test they were single edge notched specimens (SENB). The

setup of the two different tests as well as corresponding specimen shapes are shown in **Figure 2.6**.

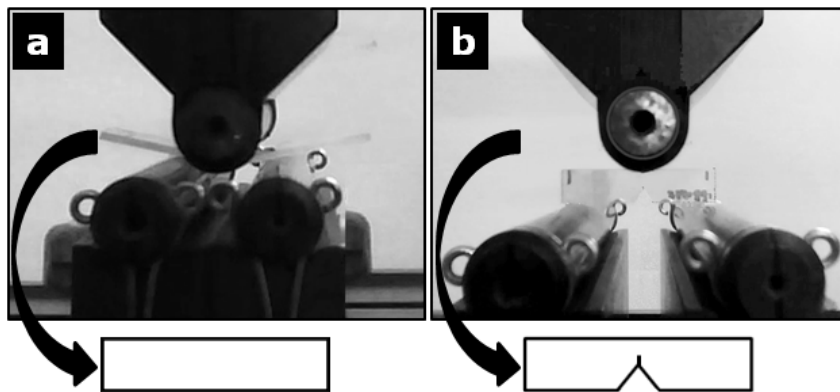


**Figure 2.6.** Setup of three-bending system for the flexural test (a) and the fracture toughness test (b), and corresponding specimen shapes.

#### 2.6.2.1. Flexural test

Flexural tests were carried out following the Procedure B of the ASTM D790-10 standard test method [11] and using MTS provided with a 250 N load cell. Three-point bending tests were carried out until the maximum strain in the outer surface of the test specimen reached 0.05 mm/mm. The flexural modulus was determined by applying the following equation, where  $E$  is the flexural modulus (MPa),  $L$  the support span (mm),  $b$  the specimen width (mm),  $d$  specimen depth (mm), and  $m$  the slope of the tangent to the initial straight-line portion of the load-deflection curve (N/mm):

$$E = \frac{L^3 \cdot m}{4 \cdot b \cdot d^3}$$

#### 2.6.2.2. Fracture toughness test

Fracture toughness tests were performed according to ASTM D5045-99 standard test method [12] using the same MTS as for flexural tests. First rectangular shaped specimens were machined in order to create a sharp V-shape notch and then a natural crack was initiated using a razor blade, to obtain single edge notched specimens (SENB), as seen in **Figure 2.6**. The depth of the natural crack must be at least two times longer than the width of the machined notch tip radius and also the following

condition has to be satisfied, where  $a$  is the notch length plus the natural crack and  $W$  is the specimen depth:

$$0.45 < a/W < 0.55$$

Fracture toughness was determined by calculating the critical stress intensity factor ( $K_{IC}$ ) and the critical strain energy release rate ( $G_{IC}$ ).  $K_{IC}$  was calculated employing the following equation, where  $K_{IC}$  is the critical stress intensity factor ( $\text{MPa}\cdot\text{m}^{1/2}$ ),  $P$  is the load (kN) calculated according to the 9.1.1 section of the standard,  $B$  the specimen thickness (cm),  $W$  the specimen depth (cm),  $a$  the crack length (cm) and  $f(x)$  the equation A1.1 of the standard:

$$K_{IC} = \frac{P \cdot f(x)}{B \cdot W^{1/2}}$$

On the other hand,  $G_{IC}$ , which is the toughness parameter based on energy required to fracture, was calculated from the energy derived from integration of the load versus displacement curve up to the same load point as used for  $K_{IC}$ , since according to the standard, the direct equation proposed for the calculation of  $G_{IC}$  introduces many uncertainties and it is preferable to avoid its use. Therefore,  $G_{IC}$  is obtained by the integration of the load versus displacement curve up to the same load point as used for  $K_{IC}$  and by making a correction of this value taking into account the indentation at the loading points as well as sample compression and system compliance. Finally,  $G_{IC}$  ( $\text{J}/\text{m}^2$ ) is calculated by the following equation, where  $U$  is the corrected integrated energy (J),  $B$  the specimen thickness (m),  $W$  the specimen depth (m), and  $\phi$  the energy calibration factor, defined in equation A1.4 of the standard:

$$G_{IC} = \frac{U}{B \cdot W \cdot \phi}$$

## 2.7. Optical characterization

### 2.7.1. Ultraviolet-visible spectroscopy

Absorbance spectroscopy is based on measuring the amount of light absorbed by a sample at a given wavelength. Light absorption as a function of wavelength provides information about electronic transitions occurring in the material [13].

A monochromatic beam of light from a visible-UV light source passes through a sample. The intensity of this light beam is then measured by electronic detectors and compared to the intensity of the light that has passed through a reference, which does not absorb. Different molecules absorb radiation of different wavelengths. An absorption spectrum will show a number of absorption bands corresponding to structural groups within the molecule. The absorption of UV or visible radiation corresponds to the excitation of outer electrons. When an atom or molecule absorbs energy, electrons are promoted from their ground state to an excited state. The spectrometer usually displays absorbance on the vertical axis versus wavelength or transmittance versus wavelength, being the transmittance related with the light that passes through the sample in comparison to the light that has not. Most substances have characteristic absorbance spectra and can be identified thereby.

## **2.8. Surface characterization**

### **2.8.1. Water contact angle**

Contact angle between water drops and analyzed sample surface can be measured directly from the angle formed at the contact between the liquid and the flat surface [14]. Measurements are made using a goniometer. The drop is illuminated from behind and viewed through a lens focused on the silhouette of the drop. The drop is projected onto the computer screen to view the contact angle. A reference line is manually positioned to read the contact angle. The contact angle value gives useful information about the hydrophobic or hydrophilic character of a sample.

## **2.9. References**

- [1] A. Guinier, *X-Ray Diffraction in Crystals, Imperfect Crystals, and Amorphous Bodies*, Dover Publications, Inc., New York (USA), 1994.
- [2] C. Suryanarayana, M. G. Norton, *X-Ray Diffraction A practical Approach*, Springer Science+Business Media, LLC, New York (USA), 1998.
- [3] N. L. Alpert, W. E. Keiser, H. A. Szymanski, *IR Theory and Practice of Infrared Spectroscopy*, Plenum Press, New York (USA), 2012.

- [4] G. W. H. Höhne, W. F. Hemminger, H. J. Flammersheim, *Differential Scanning Calorimetry*, Springer, Berlin (Germany), 2003.
- [5] Dimension Icon AFM manual from Bruker Corporation.
- [6] H. J. Butt, B. Cappella, M. Kappl, *Surf. Sci. Rep.* 2005, **59**, 1-152.
- [7] R. García, R. Pérez, *Surf. Sci. Rep.* 2002, **47**, 197-301.
- [8] A. R. Clarke, C. N. Eberhardt, *Microscopy techniques for materials science*, Woodhead Publishing Limited, Cambridge (United Kingdom), 2002.
- [9] Keithley 4200 Applications Guide.
- [10] U. Hartmann, *Annu. Rev. Mater. Sci.* 1999, **29**, 53-87.
- [11] ASTM D790-10 Test Methods for Flexural Properties of Unreinforced and Reinforced Plastics and Electrical Insulating Materials.
- [12] ASTM D5045-99 Standard Test Methods for Plane-Strain Fracture Toughness and Strain Energy Release Rate of Plastic Materials.
- [13] Z. Chen, H. N. Dinh, E. Miller, *Photoelectrochemical Water Splitting*, Springer, New York (USA), 2013.
- [14] D. Y. Kwok, A. W. Neumann, *Adv. Colloid Interfac.* 1999, **81**, 167-249.

# 3

**Polystyrene-*block*-polymethyl  
methacrylate diblock copolymer and  
TiO<sub>2</sub> nanocrystals based nanocomposites**



### 3. Polystyrene-*block*-polymethyl methacrylate diblock copolymer and TiO<sub>2</sub> nanocrystals based nanocomposites

In this Chapter, TiO<sub>2</sub>NC/PS-*b*-PMMA nanocomposites were prepared by the incorporation of commercial titanium dioxide nanocrystals (TiO<sub>2</sub>NC) into a self-assembled polystyrene-*block*-polymethyl methacrylate (PS-*b*-PMMA) block copolymer. Different amounts of TiO<sub>2</sub> nanocrystals were added to the PS-*b*-PMMA matrix in order to study the effect of the TiO<sub>2</sub> nanocrystal content on the final properties of TiO<sub>2</sub>NC/PS-*b*-PMMA nanocomposites, and more deeply on their optical and conductive properties.

#### 3.1. Introduction

The combination of self-assembled block copolymer systems with inorganic components like different types of inorganic nanocrystals can lead to highly ordered nanocomposites that have the potential to be used in a wide range of applications due to the optical [1-3], magnetic [4-6] or conductive [7-10] properties of the inorganic nanocrystals. In the last decade, many researchers have used polystyrene-*block*-polymethyl methacrylate (PS-*b*-PMMA) block copolymer as a template to create hybrid inorganic/organic nanocomposites by adding different kinds of inorganic nanocrystals to the polymeric matrix.

Nanoparticles such as Fe<sub>3</sub>O<sub>4</sub> [6,11], SiO<sub>2</sub> [12], Au [13-15] or TiO<sub>2</sub> [16-18] among others have been incorporated into the PS-*b*-PMMA block copolymer matrix to obtain a uniform distribution of the inorganic nanoparticles in the organic polymeric matrix. In all these cases, the location of the nanoparticles in one of the microphase separated domains required the pretreatment of the nanoparticles using adequate surfactants, such as ionic or nonionic types, or functioning agents containing functional groups (applying grafting from or grafting to methods) compatible with the targeted microphase separated domains of one block of the block copolymer.

In this Chapter, an easy method of fabrication of hybrid inorganic/organic nanocomposites based on PS-*b*-PMMA block copolymer as self-assembled matrix modified with different commercial, hydrophobic TiO<sub>2</sub> nanocrystals content was

employed. It should be pointed out that for the incorporation of TiO<sub>2</sub> nanocrystals to the PS-*b*-PMMA block copolymer no surfactant was used, although TiO<sub>2</sub> nanocrystals were commercially modified to make them hydrophobic. Therefore, nanocrystals were selectively directed to one of the blocks of the PS-*b*-PMMA block copolymer. The final morphologies of the neat PS-*b*-PMMA block copolymer and TiO<sub>2</sub>NC/PS-*b*-PMMA nanocomposites, the dispersion of the nanocrystals in the polymeric matrix and the possibility of confinement of the inorganic nanocrystals in one of the blocks of the block copolymer were studied by AFM. Conductive properties and optical properties of obtained TiO<sub>2</sub>NC/PS-*b*-PMMA nanocomposites were studied by using EFM and UV-vis absorption spectroscopy, respectively. DSC has been used to study the thermal behavior of the obtained nanocomposites.

## 3.2. Materials and methods

### 3.2.1. Materials

PS-*b*-PMMA diblock copolymer (**Figure 3.1**), purchased from Polymer Source, was used as the self-assembling matrix.

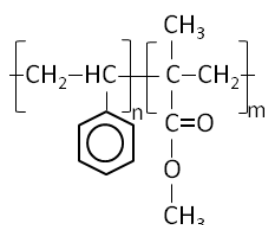


**Figure 3.1.** Chemical structure of the PS-*b*-PMMA diblock copolymer.

The polydispersity index ( $M_w/M_n$ ) of this diblock copolymer was 1.12 and the number-average molecular weights of PS and PMMA blocks were 85000 and 91000 g/mol, respectively. Hydrophobic titanium dioxide nanocrystals covered by stearic acid, with crystal size of 20 nm according to the supplier (Kemira Pigments Oy), were used in powder as received. Chloroform (purchased from Sigma-Aldrich) was used as solvent. Ammonia and hydrogen peroxide were purchased from Panreac.

### 3.2.2. TiO<sub>2</sub>NC/PS-*b*-PMMA nanocomposite preparation

First, PS-*b*-PMMA block copolymer was sonicated in chloroform (concentration

of 0.4 mg/mL) at room temperature using a 750 W microprocessor sonicator (Vibracell 75043 from Bioblock Scientific) with amplitude around 28 %. After the sonication for 2.5 h, thin films were prepared by spin-coating onto previously cleaned silicon wafer substrates using a spin-coater (Model P6700 from Specialty Coating Systems, Inc.) at 2000 rpm for 120 s.

In the case of the nanocomposites, thin films were prepared by the sonication technique in the same way as the neat block copolymer. Requested amount of TiO<sub>2</sub> nanocrystals (0.5, 1, 2, 3 and 4 wt % in respect of PS-*b*-PMMA block copolymer content) was added to the solution before the sonication. Once thin films were prepared, they were stored at ambient atmosphere until characterization.

The silicon wafers were previously cleaned by sonication in deionized water for 15 minutes, followed by the immersion into an ammonia-hydrogen peroxide-water solution (1:1:1 in volume) at 70 °C for one hour and a half. The silicon wafers were rinsed many times with deionized water.

### **3.2.3. Characterization techniques**

#### **3.2.3.1. X-ray diffraction**

XRD was carried out on a Philips PW 1710 diffractometer. The Cu K $\alpha$  X-ray source was set to 40 kV and 100 mA and the samples were examined at room temperature over the angular range from 5 to 70°.

#### **3.2.3.2. Differential scanning calorimeter**

Dynamic scans were performed from -40 to 200 °C with a heating rate of 5 °C/min and a nitrogen flow of 10 mL/min after carrying out a previous heating scan to delete the thermal history of the samples, using a Mettler Toledo DSC 822<sup>e</sup>.

#### **3.2.3.3. Atomic force microscopy**

AFM images were obtained in ambient conditions with a Nanoscope IIIa scanning probe microscope (Multimode™, Digital Instruments). Tapping mode (TM) was employed in air using an integrated tip/cantilever (125  $\mu$ m in length with ca. 300 kHz resonant frequency). Typical scan rates during recording were 0.7-1 line/s

using a scan head with a maximum range of 16  $\mu\text{m}$  x 16  $\mu\text{m}$ . More than one thin film of each composition was analyzed and different zones of each thin film were measured by AFM in order to check the homogeneity of the investigated nanocomposite films.

#### 3.2.3.4. Electrostatic force microscopy

EFM measurements were performed using the same scanning probe microscope operated in the lift mode (lift height was  $\sim 100$  nm) in ambient conditions and equipped with an integrated Co/Cr-coated MESP tip having a resonance frequency around 75 kHz. The secondary imaging mode derived from the tapping mode that measures the electric field gradient distribution above the sample surface was detected by applying a voltage to the cantilever tip.

#### 3.2.3.5. Ultraviolet-visible spectroscopy

UV-vis absorption spectra were obtained using a UV-vis spectrophotometer (Jasco V-630) in the range 200-1000 nm, from the samples prepared in chloroform solution.

### 3.3. Results and discussion

#### 3.3.1. Characterization of the commercial $\text{TiO}_2$ nanocrystals

First of all, the characterization of the commercial  $\text{TiO}_2$  nanocrystals was carried out. These commercial  $\text{TiO}_2$  nanocrystals were characterized by XRD. The diffraction pattern, as can be observed in **Figure 3.2a**, shows strong diffraction peaks at 27.5, 36.2, 41.3 and 54.4°, which were attributed to the rutile phase. Consequently, since no other phases of  $\text{TiO}_2$  nanocrystals were detected, this confirmed that they crystallized in the rutile phase [19,20].

As shown in **Figure 3.2b**,  $\text{TiO}_2$  nanocrystals, with size of around 20 nm in diameter, are clearly detected in the phase AFM image as bright, spherical spots on the dark surface of the silicon wafer. Additionally, as shown in detail in the inset of the AFM phase image and its corresponding profile, in **Figures 3.2b** and **3.2c**,  $\text{TiO}_2$  nanocrystals were surrounded by a softer material visible as a dark ring

around the bright spots [7,21], which corroborates with the fact that these nanocrystals are commercially modified with organic surfactants to be hydrophobic.

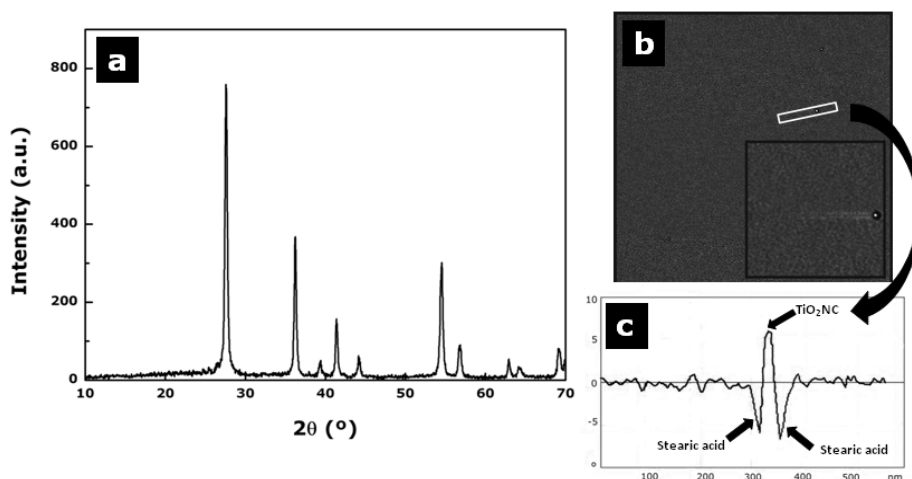


**Figure 3.2.** XRD pattern (a) and AFM image (5  $\mu\text{m}$  x 5  $\mu\text{m}$  and inset of 1  $\mu\text{m}$  x 1  $\mu\text{m}$ ) (b) of the commercial  $\text{TiO}_2$  nanocrystals and AFM phase profile of a  $\text{TiO}_2$  nanocrystal (c). The bar on the AFM phase image indicates the position where the profile was measured.

### 3.3.2. Characterization of the $\text{TiO}_2\text{NC}/\text{PS-}b\text{-PMMA}$ nanocomposites

#### 3.3.2.1. Thermal behavior

Thermal transition temperatures of the neat  $\text{PS-}b\text{-PMMA}$  block copolymer and  $\text{TiO}_2\text{NC}/\text{PS-}b\text{-PMMA}$  nanocomposites were determined by DSC. DSC thermograms of the neat  $\text{PS-}b\text{-PMMA}$  block copolymer and  $\text{TiO}_2\text{NC}/\text{PS-}b\text{-PMMA}$  nanocomposites with five different contents of  $\text{TiO}_2$  nanocrystals (0.5, 1, 2, 3 and 4 wt %) are shown in the **Figure 3.3**.

In the case of the neat  $\text{PS-}b\text{-PMMA}$  block copolymer, two glass transition temperatures ( $T_g$ ) were observed. The first one, around 105  $^\circ\text{C}$ , corresponds to the  $T_g$  of the PS block and the second, around 130  $^\circ\text{C}$ , to the PMMA block.

On the other hand, DSC thermograms of  $\text{TiO}_2\text{NC}/\text{PS-}b\text{-PMMA}$  nanocomposites also showed two independent glass transitions related to the PS block and PMMA block rich phases, which appeared at temperatures similar to the glass transitions of the neat  $\text{PS-}b\text{-PMMA}$  block copolymer. In this case,  $T_g$ s corresponding to both PS block and PMMA block rich phases in investigated nanocomposites were almost the same if compared to the  $T_g$ s in the neat  $\text{PS-}b\text{-PMMA}$  block copolymer.

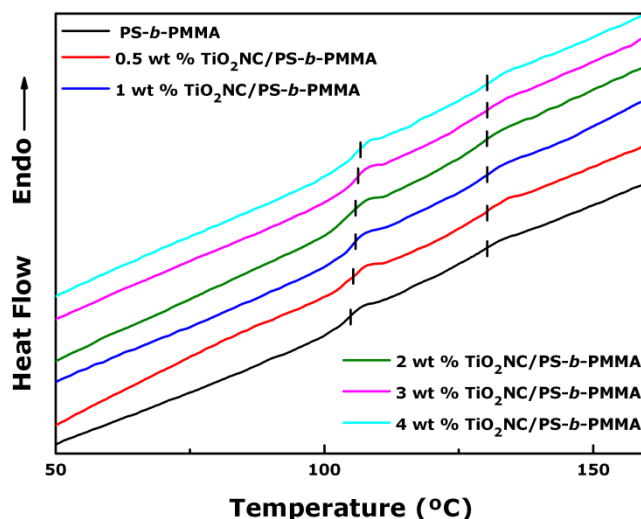


**Figure 3.3.** DSC thermograms of the neat PS-*b*-PMMA block copolymer and TiO<sub>2</sub>NC/PS-*b*-PMMA nanocomposites containing different TiO<sub>2</sub> nanocrystal contents.

However, a slight increase of the  $T_g$  corresponding to the PS block in TiO<sub>2</sub>NC/PS-*b*-PMMA nanocomposites was detected with the increasing of the TiO<sub>2</sub> nanocrystal content. This fact indicates that TiO<sub>2</sub> nanocrystals are located in the PS block of the block copolymer since the presence of TiO<sub>2</sub> nanocrystals in that block would hinder the PS block chains mobility resulting in a higher glass transition temperature of the block [22].

### 3.3.2.2. Morphology

The morphologies of PS-*b*-PMMA block copolymer and its nanocomposites with TiO<sub>2</sub> were investigated by AFM in order to prove the location of TiO<sub>2</sub> nanocrystals in the PS-*b*-PMMA matrix as well as the effect of the TiO<sub>2</sub> nanocrystal content on the final morphology of the investigated nanocomposites.

Phase AFM images of the neat PS-*b*-PMMA block copolymer and of the investigated PS-*b*-PMMA based nanocomposites are shown in **Figure 3.4**. In the case of the neat block copolymer, a microphase separation can be clearly observed in a regular self-assembled block copolymer film. As can be clearly distinguished, the neat block copolymer (**Figure 3.4a**) consists of bright microphase separated domains in a dark matrix (for more details see the inset in **Figure 3.4a**). Bright domains might correspond to the PS block rich phase whereas dark areas might correspond to the PMMA block rich phase. The size of the

microphase separated PS block domains is around 30-45 nm in diameter and 40-80 nm in length and they show typical worm-like structure [23,24]. Optical microscope was also used to analyze the PS-*b*-PMMA block copolymer thin film and it indicated lack of macrophase separation. Consequently, taking this into account and the fact that AFM measurement performed in different zones showed worm-like structure, uniformly nanostructured PS-*b*-PMMA block copolymer film was obtained.

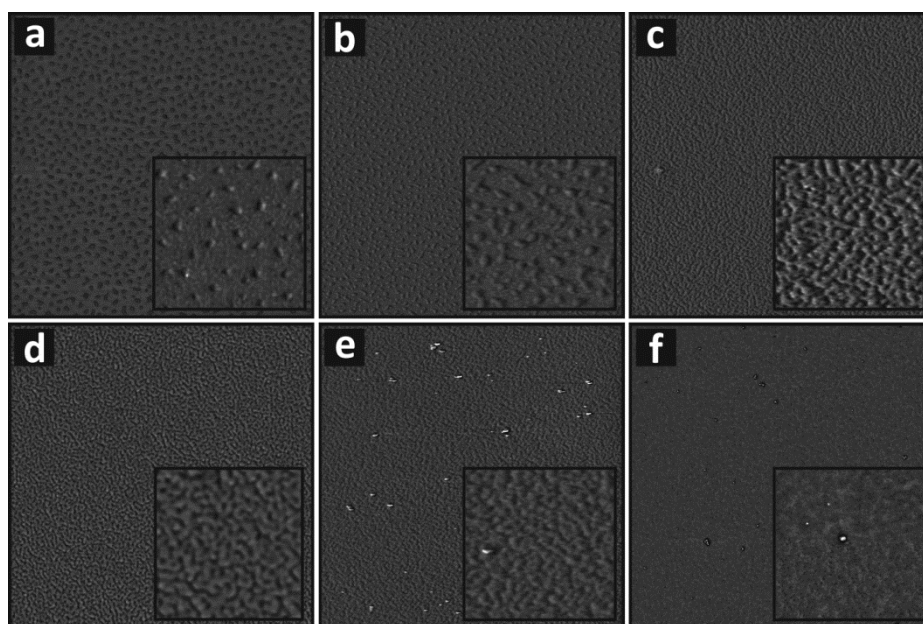


**Figure 3.4.** AFM phase images (5 μm x 5 μm and inset of 1 μm x 1 μm) of the neat PS-*b*-PMMA block copolymer (a) and TiO<sub>2</sub>NC/PS-*b*-PMMA nanocomposites containing 0.5 (b), 1 (c), 2 (d), 3 (e) and 4 (f) wt % TiO<sub>2</sub> nanocrystal contents.

On the other hand, all investigated nanocomposites showed good dispersion of TiO<sub>2</sub> nanocrystals in the PS-*b*-PMMA block copolymer matrix independent of the content of the inorganic part. Moreover, as not expected, the increase of the TiO<sub>2</sub> nanocrystals amount even up to 4 wt % in the nanocomposites did not prevent the self-assembly of PS-*b*-PMMA block copolymer matrix. The addition of 0.5 wt % TiO<sub>2</sub> nanocrystals into the block copolymer matrix did not change the final morphology of the nanocomposite if compared with the morphology of neat PS-*b*-PMMA block copolymer. However, it is worth to note that the size of the bright TiO<sub>2</sub>NC/PS block rich phase increased to 40-60 nm in diameter and 60-130 nm in length if compared with the size of microphase separated PS block in the neat PS-*b*-PMMA confirming the confinement between TiO<sub>2</sub> nanocrystals and PS block.

This phenomenon can be better understood taking into account that the employed nanocrystals had a hydrophobic character due to the stearic acid used by the supplier as an organic surfactant. In addition to this, the Flory-Huggins interaction parameters between the surfactant and each block of the block copolymer calculated applying Hoftyzer and Van Krevelen method [25] confirm good affinity between TiO<sub>2</sub> nanocrystals and the PS block of the PS-*b*-PMMA block copolymer.

The introduction of 1 wt % of TiO<sub>2</sub> nanocrystals led to a significant change on the morphology from worm-like to cylindrical structure (parallelly and perpendicularly oriented cylinders). Additionally, in these nanocomposites the bright TiO<sub>2</sub>NC/PS block rich phase became the matrix, where the total area increased with increasing the inorganic part in TiO<sub>2</sub>NC/PS-*b*-PMMA nanocomposites. Thus, the increase of the TiO<sub>2</sub> nanocrystal content caused an increase in the size of PS block domains, which confirmed once more that TiO<sub>2</sub> nanocrystals were mainly located in the PS block. As can be clearly seen by comparison of AFM images corresponding to nanocomposites, the addition of 3 and 4 wt % of TiO<sub>2</sub> nanocrystals into PS-*b*-PMMA matrix deteriorated the final morphology of the systems probably due to the fact that aggregates of inorganic nanocrystals appear as a consequence of a high TiO<sub>2</sub> nanocrystal content.

Here, it should be also noted that AFM technique was also used to measure the thickness of the thin films, by scratching a part of each investigated film prepared by spin-coating, resulting in films with a thickness lower than 20 nm.

### 3.3.2.3. Conductive properties

Conductive properties of the neat PS-*b*-PMMA block copolymer and TiO<sub>2</sub>NC/PS-*b*-PMMA nanocomposites in function of the addition of TiO<sub>2</sub> nanocrystals to the block copolymer matrix were studied by EFM. EFM phase images of the neat PS-*b*-PMMA block copolymer and TiO<sub>2</sub>NC/PS-*b*-PMMA nanocomposites after applying different positive and negative voltages are shown in **Figure 3.5**.

As was expected, PS-*b*-PMMA block copolymer did not show any response to any of the applied voltages, indicating absence of conductivity. For all investigated TiO<sub>2</sub>NC/PS-*b*-PMMA nanocomposites it can be clearly seen that likewise no bright

domains were detected when 0 V was applied. However, when any positive or negative voltage was applied, some bright conductive areas appeared on the surface related to the presence of TiO<sub>2</sub> nanocrystals in one of the blocks of PS-*b*-PMMA block copolymer. Thus, the contrast between the bright and the dark areas increased with the increase of the value of the applied voltage, whereas the response was clearly independent of the sign of the voltage. Moreover, the morphology obtained by AFM and EFM image showed a clear correspondence between each other, which confirmed that the brighter microphase separated phase in AFM phase images corresponded to the charged domains in EFM phase images. The microphase separated phase corresponded to TiO<sub>2</sub>NC/PS block rich phase and taking into account that PS-*b*-PMMA block copolymer does not respond to the applied voltage, this proves that TiO<sub>2</sub>NC/PS block rich phase possesses conductive properties due to the location of TiO<sub>2</sub> nanocrystals in the PS block.

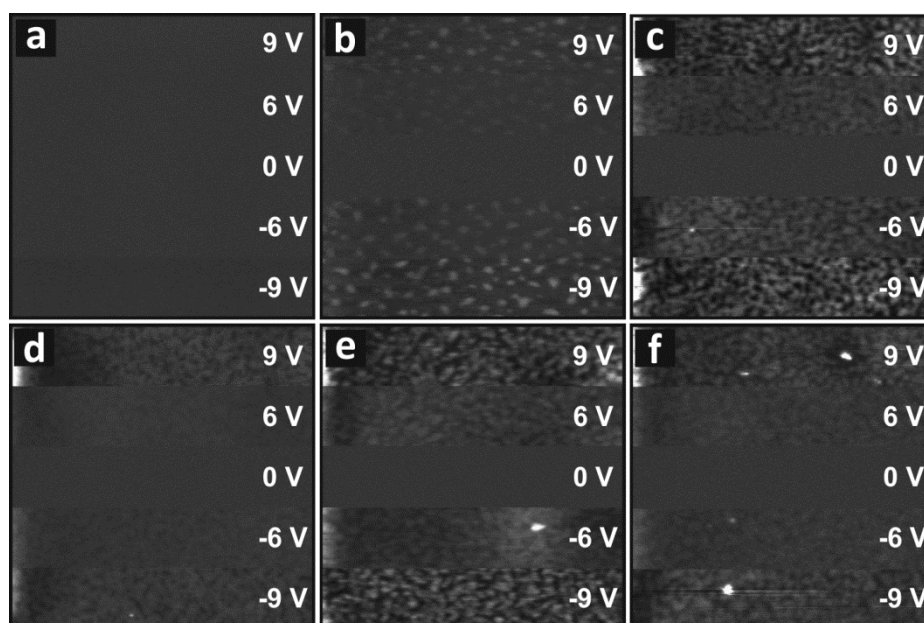


**Figure 3.5.** EFM phase images (2  $\mu\text{m}$  x 2  $\mu\text{m}$ ) of the neat PS-*b*-PMMA block copolymer (a) and TiO<sub>2</sub>NC/PS-*b*-PMMA nanocomposites containing 0.5 (b), 1 (c), 2 (d), 3 (e) and 4 (f) wt % TiO<sub>2</sub> nanocrystal contents obtained by applying 0, 6, 9, -6 and -9 V.

On the other hand, comparing the results corresponding to all investigated nanocomposites among them, one can conclude that the increase of TiO<sub>2</sub> nanocrystals does not provoke significant changes in the obtained EFM phase images. Here it should be pointed out that EFM measurement is a qualitative measurement, not quantitative. However, it can be appreciated that the images become slightly less clear when the

content of nanocrystals is higher in the nanocomposite. This can be related to the fact that in nanocomposites with higher content of nanocrystals some aggregates of  $\text{TiO}_2$  nanocrystals can be detected (see **Figures 3.5e** and **3.5f**) since they are not only located in the microphase separated PS block domains but also in the PMMA matrix. In addition to this, in the cases of 3 and 4 wt %  $\text{TiO}_2\text{NC}/\text{PS-}b\text{-PMMA}$  nanocomposites, some charged spots can be detected on the surface that might be related to  $\text{TiO}_2$  nanocrystals aggregates.

#### 3.3.2.4. Optical properties

UV-vis absorption was used to characterize  $\text{PS-}b\text{-PMMA}$  block copolymer and  $\text{TiO}_2\text{NC}/\text{PS-}b\text{-PMMA}$  nanocomposite solutions in chloroform. The UV-vis absorption spectra of the  $\text{TiO}_2$  nanocrystals, neat  $\text{PS-}b\text{-PMMA}$  block copolymer and  $\text{TiO}_2\text{NC}/\text{PS-}b\text{-PMMA}$  nanocomposites are shown in **Figure 3.6**.

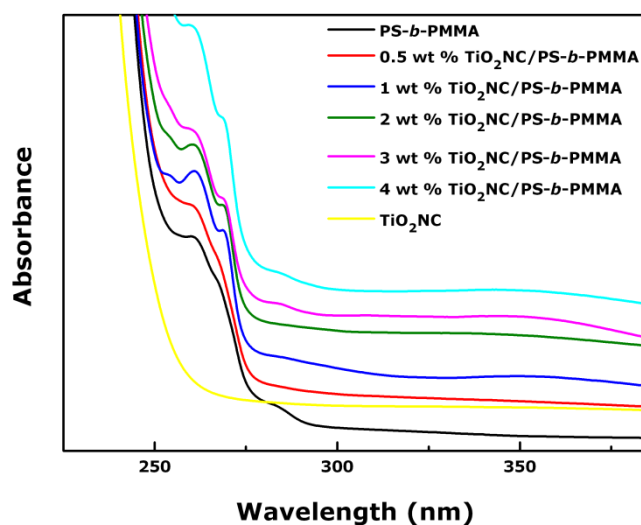


**Figure 3.6.** UV-vis absorption spectra of the neat  $\text{PS-}b\text{-PMMA}$  block copolymer and  $\text{TiO}_2\text{NC}/\text{PS-}b\text{-PMMA}$  nanocomposites containing different  $\text{TiO}_2$  nanocrystal contents.

$\text{PS-}b\text{-PMMA}$  block copolymer and all investigated  $\text{TiO}_2\text{NC}/\text{PS-}b\text{-PMMA}$  nanocomposites absorbed around 275 nm wavelength. Moreover,  $\text{TiO}_2\text{NC}/\text{PS-}b\text{-PMMA}$  nanocomposites showed higher absorbance with the increase of the  $\text{TiO}_2$  nanocrystal content. This phenomenon can be better understood taking into account that  $\text{TiO}_2$  nanocrystals, as optically active inorganic fillers, absorbed strongly in the range lower than 260 nm wavelength. These results confirm that  $\text{TiO}_2$  nanocrystals transfer their optical properties to the designed nanocomposites.

### 3.4. Conclusions

PS-*b*-PMMA block copolymer was used as template for the fabrication of TiO<sub>2</sub>NC/PS-*b*-PMMA nanocomposites with different contents of commercial rutile TiO<sub>2</sub> nanocrystals covered by stearic acid. The materials obtained by the addition of TiO<sub>2</sub> nanocrystals to the PS-*b*-PMMA block copolymer showed good properties against UV radiation, which confirmed that TiO<sub>2</sub> nanocrystals transfer their optical properties to TiO<sub>2</sub>NC/PS-*b*-PMMA nanocomposites. On the other hand, as confirmed by AFM measurements, the addition of even a high content of TiO<sub>2</sub> nanocrystals did not prevent the self-assembly of PS-*b*-PMMA block copolymer in the designed nanocomposites. Additionally, a good dispersion of TiO<sub>2</sub> nanocrystals was achieved independent on the TiO<sub>2</sub> content.

DSC and AFM results indicated that TiO<sub>2</sub> nanocrystals were confined in the microphase separated PS block domains. Consequently, the increase of the TiO<sub>2</sub> nanocrystal content led to the increase of the size of the microphase separated PS block rich phase. This affected the final morphology of the nanocomposites if compared to the morphology of the neat block copolymer. Thus, worm-like structure changed to cylindrical one. As seen by EFM, TiO<sub>2</sub> nanocrystals transfer also their conductive properties to the TiO<sub>2</sub>NC/PS-*b*-PMMA nanocomposites, which allow designing inorganic/organic hybrid materials with optical and conductive properties.

### 3.5. References

- [1] J. L. Martinez-Hurtado, *Nanomaterials* 2011, **1**, 20-30.
- [2] J. Gutierrez, I. Mondragon, A. Tercjak, *Polymer* 2011, **52**, 5699-5707.
- [3] W. C. Yen, Y. H. Lee, J. F. Lin, C. A. Dai, U. S. Jeng, W. F. Su, *Langmuir* 2011, **27**, 109-115.
- [4] C. T. Lo, C. J. Chao, *Langmuir* 2009, **25**, 12865-12869.
- [5] L. G. Bach, R. Islam, J. T. Kim, S. Y. Seo, K. T. Lim, *Appl. Surf. Sci.* 2012, **258**, 2959-2966.
- [6] C. Xu, K. Ohno, V. Ladmiraal, D. E. Milkie, J. M. Kikkawa, R. J. Composto, *Macromolecules* 2009, **42**, 1219-1228.
- [7] A. Tercjak, J. Gutierrez, C. J. Ocando, L. Peponi, I. Mondragon, *Acta Mater.* 2009, **57**, 4624-4631.

- [8] J. Gutierrez, A. Tercjak, I. Mondragon, *J. Am. Chem. Soc.* 2010, **132**, 873-878.
- [9] A. Türke, W. J. Fischer, H. J. Adler, A. Pich, *Polymer* 2010, **51**, 4706-4712.
- [10] L. Peponi, A. Tercjak, J. Gutierrez, H. Stadler, L. Torre, J. M. Kenny, I. Mondragon, *Macromol. Mater. Eng.* 2008, **293**, 568-573.
- [11] I. Barandiaran, G. Kortaberria, *Eur. Polym. J.* 2015, **68**, 57-67.
- [12] C. H. Liu, L. K. Chiu, J. Y. Yeh, R. C. C. Tsiang, *J. Nanomater.* 2012, **2012**, 327583/1-327583/7.
- [13] J. H. Choi, S. M. Adams, R. Ragan, *Nanotechnology* 2009, **20**, 065301/1-065301/6.
- [14] S. Kim, M. Yoo, N. Kang, B. Moon, B. J. Kim, S. H. Choi, J. U. Kim, J. Bang, *ACS Appl. Mater. Interfaces* 2013, **5**, 5659-5666.
- [15] F. Lai, T. Borca-Tasciuc, J. Plawsky, *Nanotechnology* 2015, **26**, 055301/1-055301/9.
- [16] C. C. Weng, K. H. Wei, *Chem. Mater.* 2003, **15**, 2936-2941.
- [17] J. Gutierrez, A. Tercjak, I. Garcia, I. Mondragon, *Nanotechnology* 2009, **20**, 225603/1-225603/9.
- [18] S. T. Hailu, S. Samant, C. Grabowski, M. Durstock, A. Karim, D. Raghavan, *J. Polym. Sci., Part A: Polym. Chem.* 2015, **53**, 468-478.
- [19] B. Qi, L. Wu, Y. Zhang, Q. Zeng, J. Zhi, *J. Colloid. Interf. Sci.* 2010, **345**, 181-186.
- [20] K. Tomita, V. Petrykin, M. Kobayashi, M. Shiro, M. Yoshimura, M. Kakihana, *Angew. Chem.* 2006, **45**, 2378-2381.
- [21] I. Garcia, N. E. Zafeiropoulos, A. Janke, A. Tercjak, A. Eceiza, M. Stamm, I. Mondragon, *J. Polym. Sci., Part A: Polym. Chem.* 2007, **45**, 925-932.
- [22] I. García, A. Tercjak, N. E. Zafeiropoulos, M. Stamm, I. Mondragon, *Macromol. Rapid Commun.* 2007, **28**, 2361-2365.
- [23] C. C. Chang, C. T. Lo, *J. Phys. Chem. B* 2011, **115**, 2485-2493.
- [24] C. Ocando, E. Serrano, A. Tercjak, C. Peña, G. Kortaberria, C. Calberg, B. Grignard, R. Jerome, P. M. Carrasco, D. Mecerreyes, I. Mondragon, *Macromolecules* 2007, **40**, 4068-4074.
- [25] D. W. Van Krevelen, *Properties of Polymers*, Elsevier Science B. V., Amsterdam (The Netherlands), 1990.

**4**

**Polystyrene-*block*-polymethyl  
methacrylate diblock copolymer  
and synthesized TiO<sub>2</sub> nanorods  
based nanocomposites**



## 4. Polystyrene-*block*-polymethyl methacrylate diblock copolymer and synthesized TiO<sub>2</sub> nanorods based nanocomposites

In this Chapter, the same PS-*b*-PMMA block copolymer as in the previous Chapter has been used in order to prepare and characterize novel hybrid inorganic/organic nanocomposites. In this case, the inorganic part incorporated into the self-assembled PS-*b*-PMMA block copolymer has been TiO<sub>2</sub> nanorods (TiO<sub>2</sub>NR), synthesized by means of a colloidal synthetic approach. The main interest of this approach was the specific surface chemistry of the nanorods, which consisted in an organic capping layer that makes the surface of the nanorods hydrophobic. TiO<sub>2</sub>NR/PS-*b*-PMMA nanocomposites were prepared by the incorporation of synthesized TiO<sub>2</sub> nanorods into the PS-*b*-PMMA block copolymer up to high contents of the inorganic part. Developed nanocomposites were characterized mainly from the point of view of their optical and conductive properties as in the previous Chapter, with the objective of studying the influence of the different TiO<sub>2</sub> nanorod contents on the final properties of the nanocomposites.

The work presented in this Chapter was carried out in collaboration with the Institute for Physical and Chemical Processes of the Italian National Research Council, located in Bari, Italy, where the synthesis of the TiO<sub>2</sub> nanorods was performed.

### 4.1. Introduction

As has been concluded in the previous Chapter, nanoparticles incorporated into a block copolymer matrix can significantly affect a wide range of the final material properties. However, the enhancement of such properties generally depends on the kind of nanoparticle dispersed in the block copolymer matrix and in particular on the ability to control the nanoparticle location within the host matrix. Generally, two main approaches can be followed in order to prepare nanoparticles/block copolymer nanocomposites with synthesized nanoparticles [1]. The first one is based on an *in situ* synthesis of the inorganic nanoparticles within a block copolymer domain. In the second case, the synthesis of nanoparticles is

accomplished *ex situ*, before their incorporation in the block copolymer.

Among the different types of nanomaterials, semiconducting titanium dioxide nanoparticles have attracted attention owing to their several potential applications in fields such as photocatalysts, sensors, solar cells and memory devices [2,3]. In the last years, many studies have reported the fabrication of hybrid nanocomposites based on a block copolymer acting as template for the incorporation of TiO<sub>2</sub> nanoparticles [4-11]. Many investigations report the *in situ* method for the synthesis of TiO<sub>2</sub> nanoparticles carried out by means of sol-gel technique inside the block copolymer solution [5-10], while other examples account for the *ex situ* TiO<sub>2</sub> nanoparticle synthesis prior to the incorporation into a block copolymer [4,11].

In this Chapter, semiconductor TiO<sub>2</sub> colloidal nanorods have been obtained *ex situ* by means of a colloidal chemistry procedure [12-15], which allows to control their size and shape. Oleic acid has been used as a surfactant, in order to control the nanorod growth during the synthesis, prevent their aggregation and allow to obtain their stable dispersion in organic solvents. Therefore, nanorods have been effectively dispersed in toluene and, then incorporated into the PS-*b*-PMMA block copolymer, used as a template.

The most important factor in order to get an affective confinement of nanoparticles in one phase of the block copolymer is the compatibility between nanoparticles and one block of the block copolymer, that in this case has been achieved due to the organic capping layer of nanorods. The morphological, structural and chemical characterization of TiO<sub>2</sub> nanorods, in terms of their size, shape and chemical surface, was performed by TEM and FTIR, respectively. Optical properties of nanocomposite solutions have been investigated by means of UV-vis absorption spectroscopy. Nanocomposites, with the increase of nanorod content, have been deposited as thin film and characterized by AFM in order to study the morphologies of the different TiO<sub>2</sub>NR/PS-*b*-PMMA nanocomposites as well as the dispersion and location of the incorporated nanorods within the PS-*b*-PMMA block copolymer. Conductive properties of nanocomposite films have been analyzed at nanoscale by EFM and PeakForce TUNA, while a semiconductor analyzer has been used for their conductive investigation at macroscale.

## 4.2. Materials and methods

### 4.2.1. Materials

The same block copolymer as in Chapter 3, the PS-*b*-PMMA diblock copolymer, purchased from Polymer Source, was used. In this case, its polydispersity index ( $M_w/M_n$ ) was 1.17 and the number-average molecular weights of PS and PMMA blocks were 83000 and 92500 g/mol, respectively.

For the synthesis of TiO<sub>2</sub> nanorods, titanium tetraisopropoxide (Ti(OPri)<sub>4</sub> or TTIP, 99.999 %), trimethylamino-N-oxide dihydrate ((CH<sub>3</sub>)<sub>3</sub>NO·2H<sub>2</sub>O or TMAO, 98 %) and oleic acid (C<sub>17</sub>H<sub>33</sub>CO<sub>2</sub>H or OLEA, 90 %) (**Figure 4.1**) were purchased from Aldrich. Methanol was also purchased from Aldrich and toluene was supplied by Labscan.

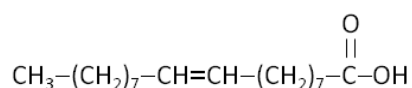


**Figure 4.1.** Chemical structure of the oleic acid.

### 4.2.2. Synthesis of TiO<sub>2</sub> nanorods

The synthesis of TiO<sub>2</sub> nanorods was performed by following a method already reported in the literature [14,16]. Organic-capped TiO<sub>2</sub> nanorods were synthesized by hydrolysis of TTIP at low temperatures using OLEA as surfactant and TMAO as catalyst for polycondensation.

First TTIP was added to previously degassed OLEA under nitrogen flow at 100 °C. Subsequently, an aqueous solution of TMAO was rapidly injected, which started the fast hydrolysis, leading to the formation of oleic acid-coated TiO<sub>2</sub> nanorods. The growth was carried out for 5 days. The obtained nanorods were precipitated from the reaction mixture upon the addition of methanol, isolated by centrifugation and re-dispersed in toluene. Obtained TiO<sub>2</sub> nanorods were 100 % anatase, as reported by the detailed structural and morphological characterization of the as-prepared oleic acid-coated crystalline TiO<sub>2</sub> nanorods found in the literature [14,16].

### 4.2.3. TiO<sub>2</sub>NR/PS-*b*-PMMA nanocomposite preparation

Firstly, PS-*b*-PMMA block copolymer solutions were prepared by dissolving a

defined amount of block copolymer in toluene to reach a concentration of 5 mg/mL. The solution was left under magnetic stirring until a homogeneous mixture was obtained. Then, an adequate volume of TiO<sub>2</sub> nanorod solution in toluene was added to the block copolymer solution in order to obtain TiO<sub>2</sub>NR/PS-*b*-PMMA nanocomposites with different TiO<sub>2</sub> nanorod contents, in the range between 1 and 50 wt %. Nanocomposite solutions were stirred for a few hours. Both neat block copolymer and nanocomposites were prepared as thin films by spin-coating the corresponding solution (same spin-coater used in Chapter 3) onto previously cleaned silicon wafer substrates at 2000 rpm for 120 s. The cleaning of the silicon wafers was carried out as described in Chapter 3. All films were kept at ambient conditions until characterization.

#### 4.2.4. Characterization techniques

##### 4.2.4.1. Fourier transform infrared spectroscopy

FTIR spectra were performed by a Varian 670-IR spectrometer equipped with a deuterated triglycine sulfate detector in attenuated total reflection (ATR) sampling mode. The internal reflection element was a one-bounce 2 mm diameter diamond microprism. Cast films were prepared directly onto the internal reflection element, by depositing the solution (3-5  $\mu$ L) on the upper face of the diamond crystal and allowing the solvent to evaporate completely. The spectral resolution used has been 4  $\text{cm}^{-1}$ .

##### 4.2.4.2. Transmission electron microscopy

TEM micrographs were obtained by a Tecnai G2 20 Twin transmission electron microscope operated at 200 kV with resolution of 2.5 Å. TiO<sub>2</sub> nanorod solution was deposited by drop casting onto carbon-coated copper grids. Size statistical analyses (nanocrystal average size and size distribution) of the samples were performed by using a freeware image analysis program (ImageJ).

##### 4.2.4.3. Atomic force microscopy

AFM measurement was performed under ambient conditions using a Dimension Icon scanning probe microscope equipped with Nanoscope V controller (Bruker). Tapping mode (TM) was employed in air using an integrated tip/cantilever (125  $\mu$ m in length with

ca. 300 kHz resonant frequency). Typical scan rates during recording were 0.9-1.1 line/s using a hybrid scan head with a maximum range of 100  $\mu\text{m}$  x 100  $\mu\text{m}$ . More than one film of each composition was analyzed and different zones of each film were measured by AFM in order to check the homogeneity of the films.

#### 4.2.4.4. Electrostatic force microscopy

EFM measurements were performed using the same Dimension Icon scanning probe microscope operating in the lift mode (lift height was  $\sim$ 100-150 nm) in ambient conditions and equipped with a Pt/Ir coating tip having a resonance frequency around 75 kHz. The secondary imaging mode derived from the tapping mode that measures the electric field gradient distribution above the film surface was detected by applying a voltage to the cantilever tip. The employment of this method allows to qualitatively characterize conductive properties at the nanometric level.

#### 4.2.4.5. Keithley semiconductor analyzer

Semiconductor characterization system (Keithley model 4200-SCS) was used to study the conductive properties of the investigated nanocomposites. Two-point experiments were carried out applying a voltage sweep from  $-4$  to  $4$  V to study the conductive properties at the macroscopic level.

#### 4.2.4.6. Tunneling atomic force microscopy

TUNA measurements were carried out with the same Dimension Icon scanning probe microscope. The measurements were carried out using PeakForce TUNA mode under ambient conditions. The PeakForce TUNA probe was equipped with the same Pt/Ir coating tip as for EFM measurement. In order to enhance the conductivity in the nanocomposite films, the organic component of the system was removed by exposing the films to 254 nm UV light (XX-15S, UVP Inc.) for 24 hours.

#### 4.2.4.7. Ultraviolet-visible spectroscopy

UV-vis absorption spectra of the solutions in toluene were obtained using a spectrophotometer (Shimadzu UV-3600) in the range between 200 and 800 nm.

### 4.3. Results and discussion

#### 4.3.1. Characterization of the synthesized TiO<sub>2</sub> nanorods

Synthesized TiO<sub>2</sub> nanorods were firstly characterized in terms of their morphology and their surface chemistry. **Figure 4.2** shows the TEM micrograph and FTIR spectrum of the TiO<sub>2</sub> nanorods. As can be clearly distinguished from the TEM image (**Figure 4.2a**), TiO<sub>2</sub> nanorods presented a rod-like shape and an average size of 3 nm in diameter and 18 nm in length [14,16], as determined by measuring the dimension of at least 100 particles for each analyzed image.

On the other hand, the surface chemistry of TiO<sub>2</sub> nanorods dispersed in toluene was investigated by FTIR spectroscopy. The FTIR spectrum of oleic acid-coated TiO<sub>2</sub> nanorods, reported in **Figure 4.2b**, exhibited specific signals corresponding to the oleic acid bands. In particular, the TiO<sub>2</sub> nanorods showed intense peaks at 2922 and 2850 cm<sup>-1</sup> attributable to the symmetric and antisymmetric C-H stretching vibrations of the -CH<sub>2</sub>- groups in the oleic acid alkyl chain, respectively.

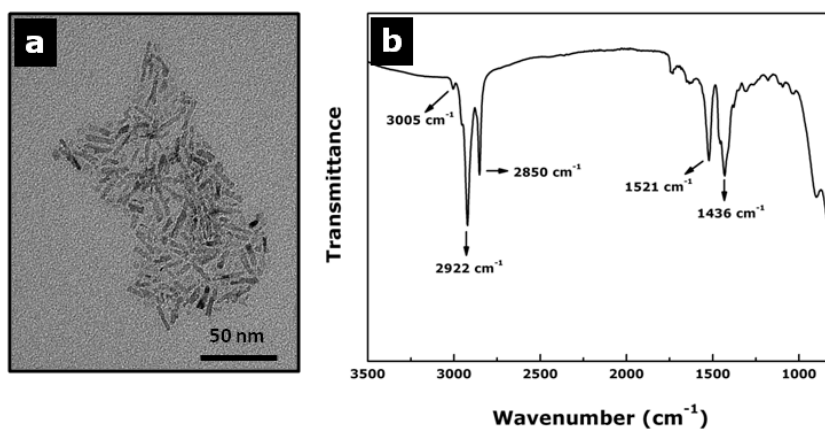


**Figure 4.2.** TEM micrograph (a) and FTIR spectrum (b) of oleic acid-coated TiO<sub>2</sub> nanorods.

In addition, the spectrum showed a shoulder at approximately 2960 cm<sup>-1</sup>, due to the asymmetric stretching of the terminal -CH<sub>3</sub> group of the alkyl chain, and the signal at 3005 cm<sup>-1</sup> that is characteristic of the olefinic C-H symmetric stretching [17]. Below 2000 cm<sup>-1</sup> two intense bands centered at 1521 and 1436 cm<sup>-1</sup> dominated the spectrum, due to the COO<sup>-</sup> antisymmetric and symmetric stretching vibrations, respectively, of carboxylate anions complexed with surface metal centers. The characteristic vibrations of the metal-oxygen bonds, below 800 cm<sup>-1</sup>, were observable in the TiO<sub>2</sub> nanorods [17].

### 4.3.2. Characterization of the TiO<sub>2</sub>NR/PS-*b*-PMMA nanocomposites

#### 4.3.2.1. Visual appearance

The visual appearance of all investigated nanocomposites, including the neat PS-*b*-PMMA block copolymer and TiO<sub>2</sub>NR/PS-*b*-PMMA nanocomposite toluene solutions, reported in **Figure 4.3**, clearly showed that all investigated solutions were transparent, although their visual appearance changed with the content of TiO<sub>2</sub> nanorods added. Thus, nanocomposites up to 10 wt % of TiO<sub>2</sub> nanorods were whitish, whereas when more than 10 wt % of TiO<sub>2</sub> nanorods was added, the solutions became yellowish.

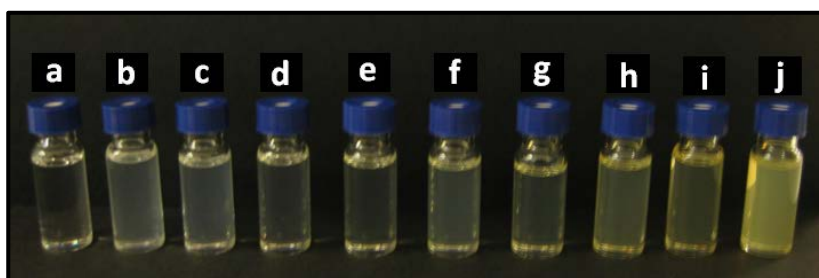


**Figure 4.3.** Visual appearance of the neat PS-*b*-PMMA block copolymer (a) and TiO<sub>2</sub>NR/PS-*b*-PMMA nanocomposite solutions containing 1 (b), 3 (c), 5 (d), 10 (e), 15 (f), 20 (g), 30 (h), 40 (i) and 50 (j) wt % TiO<sub>2</sub> nanorod contents.

#### 4.3.2.2. Morphology

The morphology of the neat PS-*b*-PMMA block copolymer film and of the TiO<sub>2</sub>NR/PS-*b*-PMMA nanocomposites was investigated by AFM. AFM phase image of the neat PS-*b*-PMMA block copolymer is shown in **Figure 4.4**. In this case, the neat block copolymer film showed a cylindrical morphology with bright microseparated cylinders in a darker matrix. The bright separated cylinders with a diameter of around 30 nm were predominantly in a parallel orientation in respect to the surface and they corresponded to the PMMA block [18] considering the contrast in the modulus and viscoelastic behavior between PS and PMMA blocks and the fact that the brighter regions in the phase image are related to the phase with higher modulus [19-21].

In addition to this, after applying the Hoftyzer and Van Krevelen method [22] to calculate the Flory-Huggins interaction parameters between toluene as solvent and each block of the block copolymer ( $\chi_{\text{PS-tol}} = 0.36$  and  $\chi_{\text{PMMA-tol}} = 0.55$ ) [20,23,24], a stronger interaction between PS block and toluene can be expected with respect to

that between PMMA block and toluene. As a result of that, PS block phase appeared as the dark matrix as a consequence of the effect of its stronger affinity with the solvent used. Therefore, the difference of the morphology obtained here for the neat block copolymer in comparison to the one obtained in Chapter 3 relies on the way of the preparation of the film, the solvent used, the block copolymer molecular weight and molar fraction of each block.

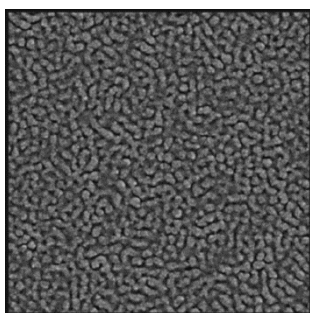


**Figure 4.4.** AFM phase image (2  $\mu\text{m}$  x 2  $\mu\text{m}$ ) of the neat PS-*b*-PMMA block copolymer.

AFM phase images of all investigated TiO<sub>2</sub>NR/PS-*b*-PMMA nanocomposites with different TiO<sub>2</sub> nanorod contents (1, 3, 5, 10, 15, 20, 30, 40 and 50 wt %) are shown in **Figure 4.5**. The content of TiO<sub>2</sub> nanorods in the nanocomposites significantly affected the morphology of the final nanocomposite films. The thin films containing up to 10 wt % TiO<sub>2</sub> nanorods maintained the same morphology as the neat block copolymer. In the case of 1 wt % of TiO<sub>2</sub>NR/PS-*b*-PMMA, the morphology was very similar to that of the neat block copolymer with slightly smaller cylinder sizes of PMMA block rich phase. TiO<sub>2</sub> nanorods, which appeared as bright spots in the phase image due to their hardness in comparison to polymeric materials, were rather uniformly dispersed located mainly in the dark phase corresponding to the PS block although always close to the interphase [25-27] between this phase and the brighter phase corresponding to the PMMA block as can be observed in the inset of **Figure 4.5a**.

Once again, the Hoftzyer and Van Krevelen method [22] was employed here to calculate the Flory-Huggins interaction parameters between TiO<sub>2</sub> nanorods and each block of the block copolymer [28,29]. For such estimation, the nanorod capping layer consisting of oleic acid was taken into account. Therefore, the interaction parameter between PS block and oleic acid resulted to be 0.45 and between PMMA block and oleic acid was 1.07, indicating that TiO<sub>2</sub> nanorods had a stronger affinity with the PS block than with the PMMA block, due to the presence of the oleic acid layer covering

the nanorod surface. Such a feature is in good agreement with AFM images, which showed a preferential location of TiO<sub>2</sub> nanorods in the PS block rich phase, and also with the behavior observed in Chapter 3 for the commercial TiO<sub>2</sub> nanocrystals, which resulted to be more compatible with the PS block of the block copolymer too.

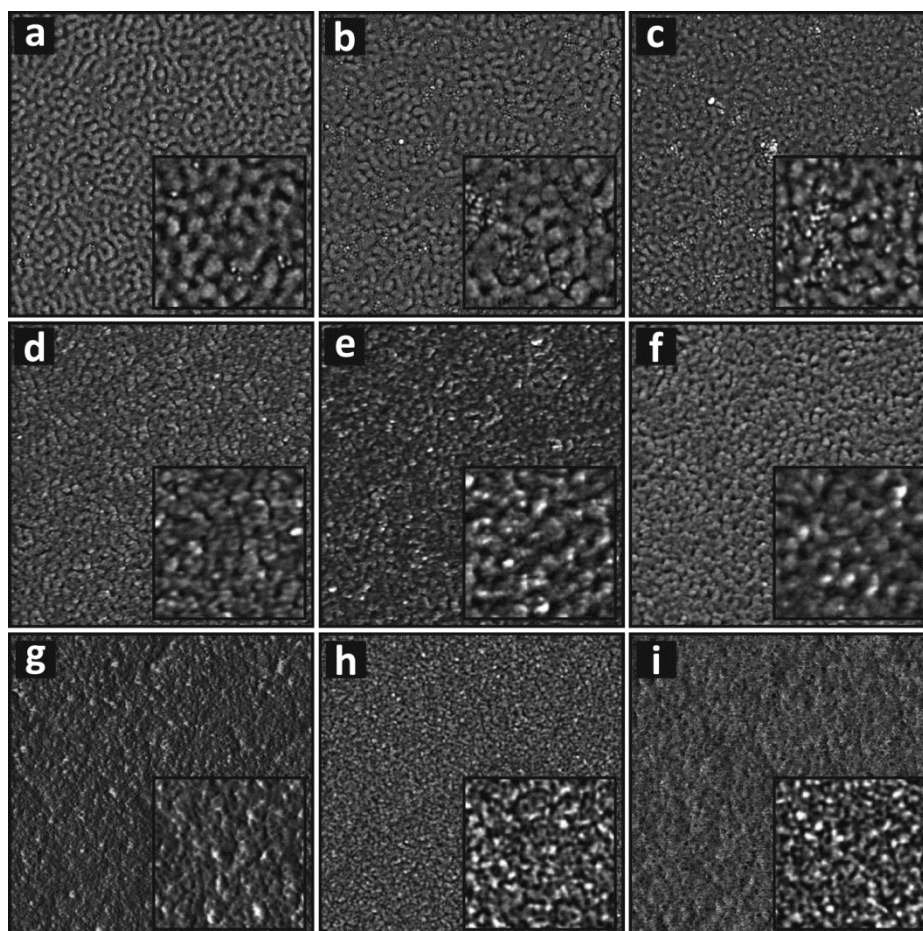


**Figure 4.5.** AFM phase images (2  $\mu\text{m}$  x 2  $\mu\text{m}$  and inset of 0.5  $\mu\text{m}$  x 0.5  $\mu\text{m}$ ) of TiO<sub>2</sub>NR/PS-*b*-PMMA nanocomposites containing 1 (a), 3 (b), 5 (c), 10 (d), 15 (e), 20 (f), 30 (g), 40 (h) and 50 (i) wt % TiO<sub>2</sub> nanorod contents.

Images in **Figures 4.5b, 4.5c and 4.5d** (3, 5 and 10 wt % TiO<sub>2</sub> nanorods) also presented cylindrical morphologies with different size of the microseparated phase, which showed closer packed cylindrical domains with increasing the TiO<sub>2</sub> nanorod content. For nanocomposite films containing 3 and 5 wt % TiO<sub>2</sub> nanorods, only some dispersed nanorods, or small nanorod aggregates appeared in the PS-*b*-PMMA matrix. Nevertheless, a cylindrical morphology of bright cylinders in a dark matrix was still present.

When nanorod content increased, they formed larger aggregates, thus resulting in a continuous bright matrix of the nanocomposite films with nanorod content

starting from 10 wt %. In the 10 wt % TiO<sub>2</sub>NR/PS-*b*-PMMA nanocomposite film, the extent of the bright phase to almost the whole film surface can be observed. Such a bright phase can be ascribed not only to the PMMA block, but also to harder inorganic TiO<sub>2</sub> nanorods confined in the PS block of the block copolymer and preferably localized in this phase close to the interphase between blocks [25-27]. Therefore, the bright phase became predominant for this nanocomposite film and for nanocomposites with TiO<sub>2</sub> nanorod content higher than 10 wt %, preventing to clearly discern between PMMA rich phase and TiO<sub>2</sub>/PS rich phase. Conversely, the small dark regions in the film can be safely ascribed to the PS block without TiO<sub>2</sub> nanorods.

Nanocomposite films at high TiO<sub>2</sub> nanorod content (higher than 10 wt %) showed completely different morphologies with respect to those obtained at lower nanorod content. The images of these nanocomposite films showed a rather uniform and regular surface. However, in these cases, the typical block copolymer microphase separation, especially at high TiO<sub>2</sub> nanorod content, cannot be clearly discerned. Such evidence can be accounted for by the fact that PS block could be completely filled by TiO<sub>2</sub> nanorods, thus inducing a full TiO<sub>2</sub>NR/PS phase coverage of the film surface, preventing the detection of PMMA block domains [30]. Nevertheless, PS-*b*-PMMA block copolymer apparently acts as a template for the TiO<sub>2</sub> nanorods, providing an overall regular surface containing uniformly dispersed TiO<sub>2</sub> nanorod assemblies. It should be noted that as a result of the colloidal synthesis approach carried out to synthesize these TiO<sub>2</sub> nanorods, nanocomposites with much higher contents of nanorods were achieved in comparison to the nanocomposites obtained with the commercial TiO<sub>2</sub> nanocrystals in Chapter 3, keeping good nanorod dispersion and maintaining the self-assembly of the block copolymer up to high contents.

#### 4.3.2.3. Conductive properties

Conductive properties of the prepared nanocomposite films composed of synthesized colloidal TiO<sub>2</sub> nanorods and PS-*b*-PMMA block copolymer were investigated by EFM, Keithley semiconductor analyzer and TUNA.

In the case of EFM measurements, positive and negative voltages were applied to the EFM tip and the different responses were analyzed. In **Figure 4.6**, the EFM phase

images corresponding to -9, -6, 0, 6 and 9 V voltages applied to surfaces of the neat PS-*b*-PMMA block copolymer and 3, 10 and 20 wt % TiO<sub>2</sub>NR/PS-*b*-PMMA nanocomposites are reported.

Remarkably, it should be mentioned that, no nanocomposite showed any response when 0 V voltage was applied to the surface. Moreover, as expected, the surface of neat PS-*b*-PMMA block copolymer did not present any bright domain at any applied voltage, which indicated that the block copolymer did not respond to the voltage, confirming that block copolymer is an uncharged material, as was already proved in Chapter 3. Consequently, in TiO<sub>2</sub>NR/PS-*b*-PMMA nanocomposites, the only conductive component could be TiO<sub>2</sub> nanorods [2,7]. In fact, when voltage values different from zero were applied, all investigated nanocomposites showed a specific response dependent on the value of the applied voltage and the content of TiO<sub>2</sub> nanorods.

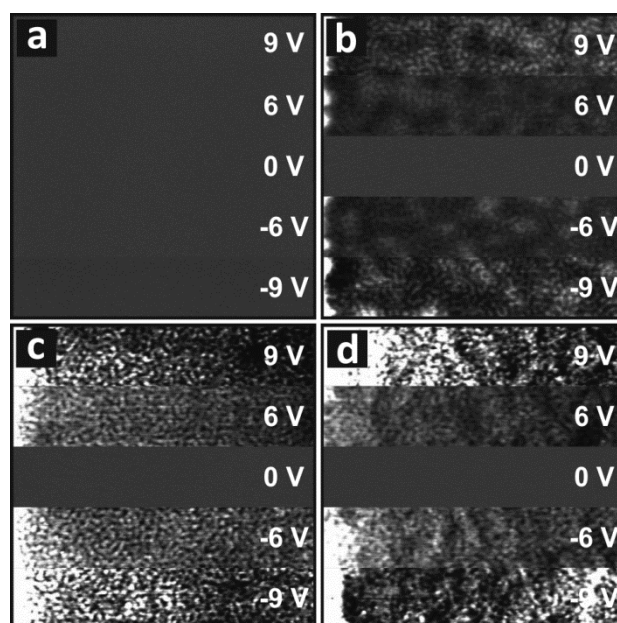


**Figure 4.6.** EFM phase images (3  $\mu\text{m}$  x 3  $\mu\text{m}$ ) of the neat PS-*b*-PMMA block copolymer (a) and TiO<sub>2</sub>NR/PS-*b*-PMMA nanocomposites containing 3 (b), 10 (c) and 20 (d) wt % TiO<sub>2</sub> nanorod contents obtained by applying 0, 6, 9, -6 and -9 V.

In the cases of 3, 10 and 20 wt % TiO<sub>2</sub>NR/PS-*b*-PMMA nanocomposite films, some bright domains appeared showing a structure similar to that visible in the corresponding AFM images. The bright domains were indicative of the presence of a conductive material confined in such domains. In particular, these bright domains can be related to the presence of TiO<sub>2</sub> nanorods, which proves confinement of the

nanorods and the conductive character of the nanocomposite films. Furthermore, it can be seen that the intensity of the bright domains as well as the amount of bright conductive domains changed with the increase in the TiO<sub>2</sub> nanorod content in the nanocomposite films, thus confirming that the incorporation of the TiO<sub>2</sub> nanorods affected to the conductive behavior of the nanocomposite films.

On the other hand, conductive properties at macroscale of fabricated TiO<sub>2</sub>NR/PS-*b*-PMMA nanocomposites were measured by means of a Keithley semiconductor analyzer. Current-voltage curves (I-V) for each nanocomposite were recorded by applying a voltage sweep between -4 and 4 V. **Figure 4.7** shows the current-voltage curves corresponding to all investigated nanocomposites. This analysis offers a qualitative tool to investigate the electrical response of prepared nanocomposites to the applied voltage. First it can be seen that the curve of the neat PS-*b*-PMMA block copolymer appeared almost horizontal, confirming, as expected, no conductivity. On the contrary, all investigated nanocomposites showed non-horizontal curves, with a slight general trend of higher slope, and consequently higher intensity values for the voltage range, for higher TiO<sub>2</sub> nanorod content in the nanocomposites, especially for higher than 15 wt % contents.

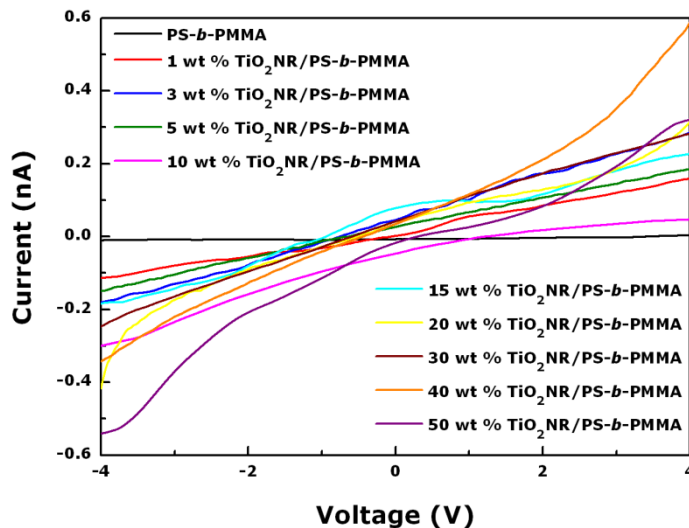


**Figure 4.7.** Current-voltage curves (I-V) of the neat PS-*b*-PMMA block copolymer and TiO<sub>2</sub>NR/PS-*b*-PMMA nanocomposites containing different TiO<sub>2</sub> nanorod contents obtained by applying a voltage sweep between -4 and 4 V.

This fact indicates that TiO<sub>2</sub> nanorods are responsible for the conductive properties of the nanocomposites [7,8]. However, in spite of a sort of slight trend, no

significant difference can be observed as a function of nanorod content. This evidence could be due to the fact that even for the highest TiO<sub>2</sub> nanorod content, still the 50 wt % of the nanocomposite was composed of non-conductive PS-*b*-PMMA. However, it should be pointed out that the performance of the colloidal synthesis approach employed to obtain oleic acid-coated TiO<sub>2</sub> nanorods allowed to reach higher TiO<sub>2</sub> nanorod content nanocomposites, which resulted in higher conductive properties in comparison with the nanocomposites prepared with commercial TiO<sub>2</sub> nanocrystals, as proved in Chapter 3. Such results make these nanocomposite materials good potential candidates for semiconductor applications.

Taking into account these promising results obtained using EFM and Keithley semiconductor analyzer, the quantitative conductive properties of the TiO<sub>2</sub>NR/PS-*b*-PMMA nanocomposites with higher nanorod content were analyzed by atomic force microscopy in the PeakForce TUNA mode. The TUNA measurements allow us to investigate the conductivity of TiO<sub>2</sub> based nanocomposites [30-33]. Images corresponding to 30, 40 and 50 wt % TiO<sub>2</sub>NR/PS-*b*-PMMA nanocomposites are shown in **Figures 4.8a, 4.8b and 4.8c**. Nanocomposites were then exposed to UV light for 24 hours in order to degrade the organic components in the nanocomposite films, including both block copolymer and nanorod organic surfactant, and thus obtaining TiO<sub>2</sub> nanorods based structures on the substrate [34-36]. These results are also reported in **Figures 4.8d, 4.8e and 4.8f**. All images exhibit the TUNA current map when applying voltages of -6, 0 and 6 V. In addition to this, the current profiles corresponding to a horizontal section of the images of -6 and 6 V are included to give more detailed information about current values passing through the investigated films.

First of all, when a voltage of 0 V was applied, no current was detected in any of the nanocomposites, as expected. In the case of non-UV-treated nanocomposites (**Figures 4.8a, 4.8b and 4.8c**), the images obtained after applying a positive voltage of 6 V showed mainly the same absence of current as observed in the case of 0 V applied, whereas when a negative voltage of -6 V was applied some dark spheres appeared in the images, indicating a current response. In general, these three analyzed nanocomposites presented a current near to zero (dark surface) when a positive voltage was applied and, conversely, a current up to -1.2 pA and some almost black

spheres when a negative voltage was applied. This evidence indicates that the application of a negative voltage has a stronger influence on the conductive behavior of the colloidal TiO<sub>2</sub> nanorods, as also observed in the resulting data from semiconductor analyzer measurements. Differences in the responses to positive or negative voltages have been reported before in literature [35].

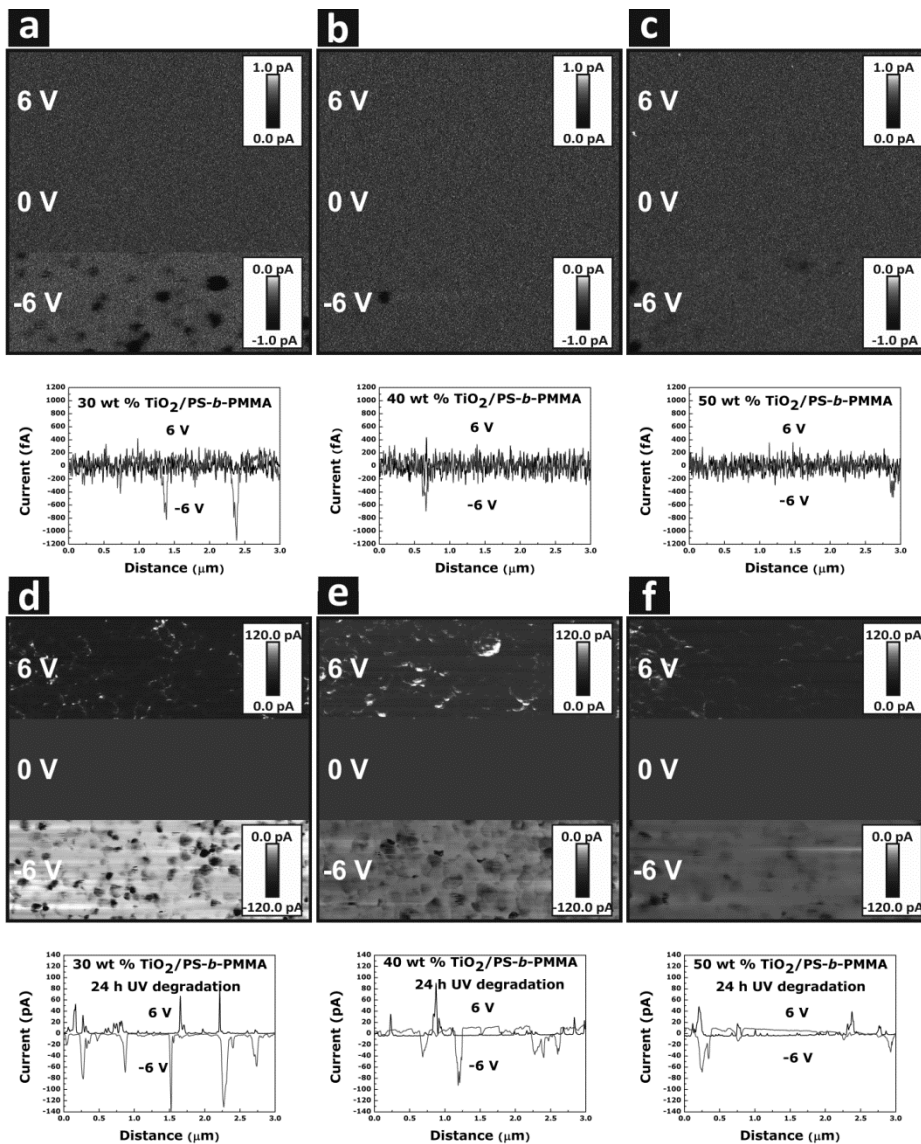


**Figure 4.8.** TUNA current images (3 μm × 3 μm) taken at voltages of -6, 0 and 6 V for 30 (a), 40 (b) and 50 (c) wt % TiO<sub>2</sub>NR/PS-*b*-PMMA nanocomposites and same contents 30 (d), 40 (e) and 50 (f) wt % TiO<sub>2</sub>NR/PS-*b*-PMMA after being exposed to UV light for 24 hours. The graphs correspond to horizontal section profiles of each -6 and 6 V images.

In addition, the 30 wt % TiO<sub>2</sub>NR/PS-*b*-PMMA nanocomposite presented a higher current values passing throughout the film and a more regular distribution of the local currents on the whole surface in comparison to nanocomposites with 40 and 50 wt % TiO<sub>2</sub>

nanorod contents, which only displayed isolated local currents in whole film. The 50 wt % TiO<sub>2</sub>NR/PS-*b*-PMMA nanocomposite image exhibited some small white dots in the image corresponding to the positive bias, which could be related to the presence of the semiconductive TiO<sub>2</sub> nanorods. Taking into account the profiles obtained from the current maps, it can be clearly seen that generally the response is higher to inverse bias, as observed in the images. The 30 wt % TiO<sub>2</sub>NR/PS-*b*-PMMA nanocomposite reached the highest current values, approximately up to -1.2 pA, whereas 40 and 50 wt % TiO<sub>2</sub>NR/PS-*b*-PMMA nanocomposites had lower values, up to -0.7 and -0.4 pA, respectively, and also more isolated local currents. Such current values are in the same order of magnitude of the values obtained in previous works for polymeric nanocomposites modified with TiO<sub>2</sub> nanoparticles [30]. However, the current does not follow a clear trend with the nanorod content. This result can be explained considering that even at a higher nanorod content in the nanocomposite, in the analyzed surface, nanorods were embedded in the block copolymer block, which could affect the conductivity.

On the other hand, as can be observed from the comparison between **Figures 4.8a, 4.8b, 4.8c and 4.8d, 4.8e, 4.8f**, the exposure to UV light of the nanocomposites caused a significant change in the TUNA current passing throughout the films when both direct and inverse voltages were applied. This phenomenon could be explained taking into account that the exposure to UV light led to the degradation of the organic components of the nanocomposites and consequently to investigate surface covered by TiO<sub>2</sub> nanorod based structures.

Nanocomposites containing 30, 40 and 50 wt % TiO<sub>2</sub> nanorods treated with UV showed considerably higher TUNA currents (**Figures 4.8d, 4.8e and 4.8f**) in comparison to the same 30, 40 and 50 wt % TiO<sub>2</sub>NR/PS-*b*-PMMA nanocomposites before their exposure to UV light. As a result of degradation of the organic components of the nanocomposites, the measured current increased, indicating more conductive surfaces. This evidence is consistent with the reported consideration that TiO<sub>2</sub> nanorods are the only component in the nanocomposite with a conductive behavior [2,7]. Therefore, the degradation of the organic components enhanced the conductive properties of these films.

In the case of the nanocomposites treated with UV, when 0 V were applied, no response was detected in the surfaces similarly as for untreated

nanocomposites. On the contrary, as can be seen in the TUNA images of 30, 40 and 50 wt %  $\text{TiO}_2\text{NR}/\text{PS-}b\text{-PMMA}$  nanocomposites, these investigated nanocomposites responded to the application of both direct and inverse bias. It should be taken into account that even if the scale bars in the case of positive and negative voltages are the same, the corresponding profiles indicated that, once again, the responses were higher in the case of the negative voltage. From these profiles it could be determined the highest TUNA currents of these nanocomposites. With the application of 6 V, around 80, 90 and 50 pA were reached for the 30, 40 and 50 wt % of  $\text{TiO}_2$  nanorod contents, respectively, and for the -6 V bias, around -140, -90 and -70 pA for the same nanocomposites. Comparing the three investigated nanocomposite films, in the case of the positive voltage, the white areas of the surface became brighter with the addition of 40 wt % and less evident with the addition of 50 wt %  $\text{TiO}_2$  nanorods.

Additionally, the darker area of these images also became slightly clearer at higher nanorod content. On the other hand, the dark spots corresponding to the inverse voltage were fewer and less intense in the cases of 40 and 50 wt %  $\text{TiO}_2$  nanorods, whereas the background of the images was darker with the increase of nanorod content. Then at higher amount of  $\text{TiO}_2$  nanorods, after UV treatment, the local detected current is lower, but the darker background suggests that the whole surface is more conductive. This finding can be explained taking into account that after UV treatment, charge percolation paths formed through the film thus leading to high currents. The schematic representation in **Figure 4.9** helps to visualize this behavior. Interestingly, after UV treatment, a clear dependence of the conductivity on the nanorod content was found, as a more conductive film was obtained at higher nanorod content.

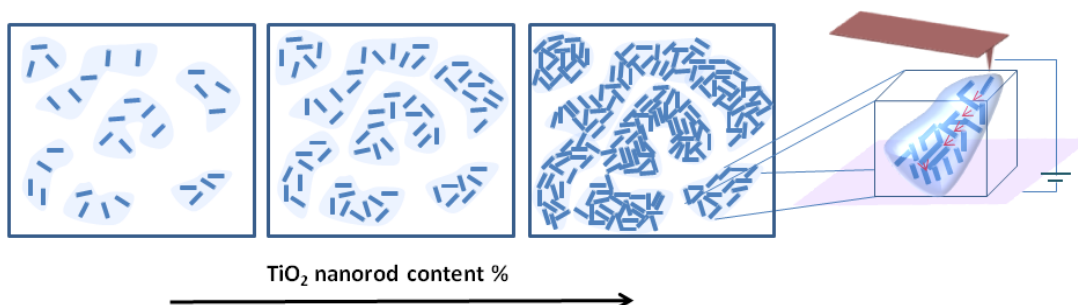


**Figure 4.9.** Schematic representation of the conductive behavior of  $\text{TiO}_2\text{NR}/\text{PS-}b\text{-PMMA}$  nanocomposites containing different  $\text{TiO}_2$  nanorod contents.

## 4.3.2.4. Optical properties

The neat PS-*b*-PMMA block copolymer and TiO<sub>2</sub>NR/PS-*b*-PMMA nanocomposite toluene solutions were investigated by means of UV-vis absorption spectroscopy. **Figure 4.10** shows the spectrum of the neat PS-*b*-PMMA block copolymer solution, which was characterized by an intense absorption in the UV region, below 300 nm.

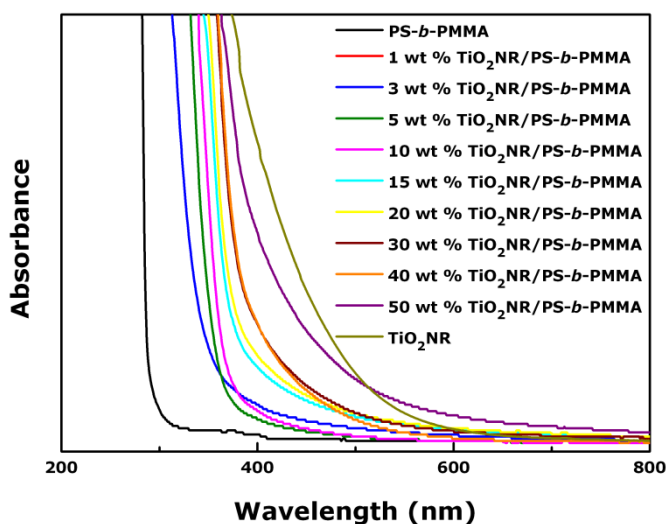


**Figure 4.10.** UV-vis absorption spectra of the neat PS-*b*-PMMA block copolymer and TiO<sub>2</sub>NR/PS-*b*-PMMA nanocomposites containing different TiO<sub>2</sub> nanorod contents.

For the spectra of TiO<sub>2</sub>NR/PS-*b*-PMMA nanocomposites, increasing the nanorod content, the absorption onset started at a wavelength higher and higher, namely between 350 and 500 nm, than that of the neat block copolymer [37], with a simultaneous broadening of the absorption tail at low energy, as was also observed in the UV absorption spectra obtained in Chapter 3 for the nanocomposites based on commercial TiO<sub>2</sub> nanocrystals. Such evidence of absorption onset starting from 350 nm can be definitely accounted for by the presence of the nanosized TiO<sub>2</sub>, which, as can be seen in its absorption curve, has a characteristic UV spectrum in such a spectral range, which defines its UV shielding properties [38-40]. Consequently, the addition of TiO<sub>2</sub> nanorods provided the nanocomposites with UV shielding properties, as a function of nanorod content. The absorption tail detected in the visible region of the nanocomposite absorption curves can be ascribed to scattering losses induced by the high amount of nanorods dispersed in block copolymer [13] as further supported by the increasing extent of the shoulder at higher content.

## 4.4. Conclusions

In summary, nanocomposites with high optical and conductive properties were obtained by means of the incorporation of synthesized colloidal TiO<sub>2</sub> nanorods into the self-assembled PS-*b*-PMMA block copolymer.

The optical properties of the nanocomposites solutions were confirmed by the UV-vis absorption behavior shown by all investigated nanocomposites.

The TiO<sub>2</sub> nanorod capping layer consisting of oleic acid molecules, allowed us to disperse high content of TiO<sub>2</sub> nanorods in the nanocomposites, up to 50 wt % in respect to the block copolymer content. TiO<sub>2</sub>NR/PS-*b*-PMMA nanocomposites with low contents of TiO<sub>2</sub> nanorods presented a clear cylindrical morphology as confirmed by AFM, whereas when the content of TiO<sub>2</sub> nanorods increased, the presence of high nanorod quantity hindered the detection of the typical morphologies attributed to block copolymers. TiO<sub>2</sub> nanorods had a stronger affinity with the PS block of the block copolymer and consequently they were located mainly in this phase changing the ratio between blocks upon the addition of nanorods. When TiO<sub>2</sub> nanorod content higher than 30 wt % was added to the block copolymer, the extended coverage of TiO<sub>2</sub> nanorods on the surface was achieved.

In addition, EFM results indicated that domains where TiO<sub>2</sub> nanorods were located, namely the TiO<sub>2</sub>NR/PS rich phase, resulted to be conductive, whereas the PMMA rich phase did not show any conductivity. In addition, PeakForce TUNA results proved high conductivity of nanocomposites with 30, 40 and 50 wt % of TiO<sub>2</sub> nanorods, when the organic component of the film was removed by exposure to UV light, leaving TiO<sub>2</sub> nanorods based structures. Such evidence can be accounted for by the occurrence of percolation paths through the nanorod based assembly in the film. Additionally, the conductive properties at macroscale, studied by applying a sweep voltage, demonstrated to be dependent on TiO<sub>2</sub> nanorod content.

The optical and semiconductive properties of the TiO<sub>2</sub> nanorods based nanocomposites, along with the opportunity offered by the block copolymer for the fabrication of TiO<sub>2</sub> based structures, open the venue to the integration of such functional nanostructured materials for applications in memory and optoelectronic devices, catalysts and sensors, as well as in energy conversion fields.

## 4.5. References

- [1] M. R. Bockstaller, R. A. Mickiewicz, E. L. Thomas, *Adv. Mater.* 2005, **17**, 1331-1349.
- [2] J. H. Pan, X. S. Zhao, W. I. Lee, *Chem. Eng. J.* 2011, **170**, 363-380.
- [3] C. Burda, Y. Lou, X. Chen, A. C. S. Samia, J. Stout, J. L. Gole, *Nano Lett.* 2003, **3**, 1049-1051.
- [4] C. C. Weng, K. H. Wei, *Chem. Mater.* 2003, **15**, 2936-2941.
- [5] Z. Sun, D. H. Kim, M. Wolkenhauer, G. G. Bumbu, W. Knoll, J. S. Gutmann, *ChemPhysChem* 2006, **7**, 370-378.
- [6] J. Gutierrez, A. Tercjak, I. Garcia, L. Peponi, I. Mondragon, *Nanotechnology* 2008, **19**, 155607/1-155607/8.
- [7] J. Gutierrez, A. Tercjak, L. Peponi, I. Mondragon, *J. Phys. Chem. C* 2009, **113**, 8601-8605.
- [8] W. C. Yen, Y. H. Lee, J. F. Lin, C. A. Dai, U. S. Jeng, W. F. Su, *Langmuir* 2011, **27**, 109-115.
- [9] D. Scalarone, J. Tata, F. Caldera, M. Lazzari, O. Chiantore, *Mater. Chem. Phys.* 2011, **128**, 166-171.
- [10] J. Xiao, W. Chen, F. Wang, J. Du, *Macromolecules* 2013, **46**, 375-383.
- [11] I. Gurevitch, R. Buonsanti, A. A. Teran, B. Gludovatz, R. O. Ritchie, J. Cabana, N. P. Balsara, *J. Electrochem. Soc.* 2013, **160**, A1611-A1617.
- [12] A. Convertino, G. Leo, M. Striccoli, G. Di Marco, M. L. Curri, *Polymer* 2008, **49**, 5526-5532.
- [13] C. Sciancalepore, T. Cassano, M. L. Curri, D. Mecerreyes, A. Valentini, A. Agostiano, R. Tommasi, M. Striccoli, *Nanotechnology* 2008, **19**, 205705/1-205705/8.
- [14] F. Petronella, E. Fanizza, G. Mascolo, V. Locaputo, L. Bertinetti, G. Martra, S. Coluccia, A. Agostiano, M. L. Curri, R. Comparelli, *J. Phys. Chem. C* 2011, **115**, 12033-12040.
- [15] A. Convertino, M. Tamborra, M. Striccoli, G. Leo, A. Agostiano, M. L. Curri, *Thin Solid Films* 2011, **519**, 3931-3938.
- [16] P. D. Cozzoli, A. Kornowski, H. Weller, *J. Am. Chem. Soc.* 2003, **125**, 14539-14548.
- [17] E. Fanizza, P. D. Cozzoli, M. L. Curri, M. Striccoli, E. Sardella, A. Agostiano, *Adv. Funct. Mater.* 2007, **17**, 201-211.

- [18] W. A. Lopes, H. M. Jaeger, *Nature* 2001, **414**, 735-738.
- [19] S. Ham, C. Shin, E. Kim, D. Y. Ryu, U. Jeong, T. P. Russel, C. J. Hawker, *Macromolecules* 2008, **41**, 6431-6437.
- [20] P. Yang, S. Wang, X. Teng, W. Wei, V. P. Dravid, L. Huang, *J. Phys. Chem. C* 2012, **116**, 23036-23040.
- [21] E. Kim, H. Ahn, S. Park, H. Lee, M. Lee, S. Lee, T. Kim, E. Kwak, J. H. Lee, X. Lei, J. Huh, J. Bang, B. Lee, D. Y. Ryu, *ACS Nano* 2013, **7**, 1952-1960.
- [22] D. W. Van Krevelen, *Properties of Polymers*, Elsevier Science B. V., Amsterdam (The Netherlands), 1990.
- [23] Y. Xuan, J. Peng, L. Cui, H. Wang, B. Li, Y. Han, *Macromolecules* 2004, **37**, 7301-7307.
- [24] G. Venugopal, S. Krause, *Macromolecules* 1992, **25**, 4626-4634.
- [25] A. Tercjak, J. Gutierrez, L. Peponi, L. Rueda, I. Mondragon, *Macromolecules* 2009, **42**, 3386-3390.
- [26] S. S. Lamarre, C. Lemay, C. Labrecque, A. M. Ritcey, *Langmuir* 2013, **29**, 10891-10898.
- [27] J. J. Chiu, B. J. Kim, E. J. Kramer, D. J. Pine, *J. Am. Chem. Soc.* 2005, **127**, 5036-5037.
- [28] M. Rawolle, E. V. Braden, M. A. Niedermeier, D. Magerl, K. Sarkar, T. Fröschl, *ChemPhysChem* 2012, **13**, 2412-2417.
- [29] J. Perlich, M. Memesa, A. Diethert, E. Metwalli, W. Wang, S. V. Roth, J. S. Gutmann, P. Müller-Buschbaum, *Colloid. Polym. Sci.* 2012, **290**, 119-126.
- [30] J. Gutierrez, A. Tercjak, I. Mondragon, *J. Am. Chem. Soc.* 2010, **132**, 873-878.
- [31] C. Prastani, A. Vetushka, A. Fejfar, M. Nanu, D. Nanu, J. K. Rath, R. E. I. Schropp, *Appl. Phys. Lett.* 2012, **101**, 083107/1-083107/4.
- [32] A. Tercjak, J. Gutierrez, C. Ocando, I. Mondragon, *Langmuir* 2010, **26**, 4296-4302.
- [33] J. Gutierrez, I. Mondragon, A. Tercjak, *J. Phys. Chem. C* 2014, **118**, 1206-1212.
- [34] T. Thurn-Albrecht, R. Steiner, J. DeRouchey, C. M. Stafford, E. Huang, M. Bal, M. Tuominen, C. J. Hawker, T. P. Russell, *Adv. Mater.* 2000, **12**, 787-791.
- [35] H. Y. Hsueh, H. Y. Chen, M. S. She, C. K. Chen, R. M. Ho, S. Gwo, H. Hasegawa, E. L. Thomas, *Nano Lett.* 2010, **10**, 4994-5000.
- [36] H. Y. Hsueh, R. M. Ho, *Langmuir* 2012, **28**, 8518-8529.
- [37] J. Gutierrez, A. Tercjak, I. Garcia, I. Mondragon, *Nanotechnology* 2009, **20**, 225603/1-225603/9.

[38] X. Meng, Z. Zhang, N. Luo, S. Cao, M. Yang, *Polym. Sci., Ser. A* 2011, **53**, 977-983.

[39] A. Tercjak, J. Gutierrez, M. D. Martin, I. Mondragon, *Eur. Polym. J.* 2012, **48**, 16-25.

[40] H. S. Lee, S. M. Koo, J. W. Yoo, *J. Ceram. Process. Res.* 2012, **13**, 300-303.



# **5** **Polystyrene-*block*-polymethyl methacrylate diblock copolymer and synthesized TiO<sub>2</sub> nanorods based nanocomposites for solar cell application**



## **5. Polystyrene-*block*-polymethyl methacrylate diblock copolymer and synthesized TiO<sub>2</sub> nanorods based nanocomposites for potential solar cell application**

Taking into account the promising results obtained in terms of the conductive and optical properties of the hybrid inorganic/organic nanocomposites based on PS-*b*-PMMA block copolymer and synthesized TiO<sub>2</sub> nanorods analyzed in the previous Chapter, in this Chapter, novel electro-devices were fabricated employing a layer of this TiO<sub>2</sub>NR/PS-*b*-PMMA nanocomposite. Taking advantage of the TiO<sub>2</sub> nanorod organic coating and consequently the high TiO<sub>2</sub> nanorod content that was dispersed in the PS-*b*-PMMA matrix, in this case, the TiO<sub>2</sub> nanorod content was increased up to 70 wt %, in order to enhance the effect of the semiconductive TiO<sub>2</sub> nanorods on the devices. The main goal is to characterize the fabricated electro-devices from the point of view of a first approach to a potential application in optoelectronic devices.

As in the previous Chapter, the work presented in this Chapter was carried out in collaboration with the Institute for Physical and Chemical Processes of the Italian National Research Council, located in Bari, Italy, where the synthesis of the TiO<sub>2</sub> nanorods was performed.

### **5.1. Introduction**

Organic photovoltaic devices are an attractive alternative to achieve a low cost, light weight and environmentally friendly solar energy source [1-5]. Organic solar cells based on polymers, in particular, have been widely investigated owing to their ease of fabrication in comparison to conventional solar cell devices. However, the main drawback of polymer based photovoltaic devices is their lower solar power efficiencies generally up to 10 % [3,5,6] as a consequence of the absence of components with high electron mobility. Consequently, this point is being extensively studied in order to achieve organic photovoltaic devices with higher carrier transport. One of the ways to enhance the charge transfer in an organic solar cell is the combination of polymers with inorganic semiconductors, resulting in hybrid inorganic/organic optoelectronic devices, such as photovoltaic systems [3,7,8].

Among different inorganic semiconductors, TiO<sub>2</sub> inorganic nanocrystals are frequently used as semiconductor in solar cell devices [3,4,7-14] since they deliver the highest energy conversion efficiency comparing to other available semiconductors. Moreover, semiconductor inorganic nanocrystals can also strengthen the optical properties of polymers in the energy conversion device, especially for photovoltaic applications, since that can extend the overall absorption range. In this perspective, synthetic protocol for fabrication of TiO<sub>2</sub> nanocrystals is particularly crucial, as it is required to enable a suitable control on the nanocrystal size, shape and surface properties, all characteristics that strongly affect the nanomaterial efficiency as active components of solar energy conversion systems. In addition, the device performances are strongly dependent on the hybrid active layer morphology on the nanometer scale.

Many research works have focused on nanostructured composites and hybrid layers, which are widely used for a variety of technological applications, including energy conversion in organic solar cells [8,15,16]. In Chapter 4, nanostructured hybrid composites were developed, by using PS-*b*-PMMA block copolymer as a template for the dispersion of synthesized colloidal TiO<sub>2</sub> nanorods, which were incorporated into the polymer matrix up to high contents resulting in conductive nanocomposites. In this Chapter, the objective is to characterize novel electro-devices fabricated with a layer of TiO<sub>2</sub>NR/PS-*b*-PMMA nanocomposite as a first approach to consider their potential application in optoelectronic devices.

As already explained in Chapter 4, the synthesis of TiO<sub>2</sub> nanorods carried out by the colloidal route based on the hydrolysis of titanium tetraisopropoxide in oleic acid as surfactant gave the possibility to manipulate the nanocrystal growth kinetics and achieve size and shape control over resulting nanocrystals. The fabricated electro-devices were investigated by means of AFM in order to analyze the morphology of the nanocomposite layer on the top of the devices. The conductive properties of the fabricated electro-devices were performed by PeakForce TUNA to measure the current at nanoscale level passing through the electro-devices and by Keithley semiconductor analyzer to determine the surface conductivity at macroscale. Finally, UV-vis spectroscopy was employed to investigate the UV-vis absorption of the fabricated electro-devices.

## 5.2. Materials and methods

### 5.2.1. Materials

For the preparation of TiO<sub>2</sub>NR/PS-*b*-PMMA nanocomposites, the same materials as in Chapter 4 were used. On the other hand, for the fabrication of electro-devices, apart from the inorganic/organic nanocomposites, indium tin oxide (ITO) coated glass (sheet resistivity 8-12 Ω/sq, Aldrich), poly(3,4-ethylenedioxythiophene)-poly(styrenesulfonate) (PEDOT:PSS, Clevios™ Al 4083) and Poly(3-hexylthiophene-2,5-diyl) (P3HT, Aldrich) were used. Acetone, supplied by Oppac, and 2-propanol and chlorobenzene, supplied by Panreac, were used as solvent.

### 5.2.2. ITO-glass/PEDOT:PSS/P3HT/(TiO<sub>2</sub>NR/PS-*b*-PMMA) electro-devices fabrication

Following exactly the same procedure described in Chapter 4, firstly nanocomposite solutions consisting of synthesized oleic acid-coated TiO<sub>2</sub> nanorods (3 nm in diameter and 18 nm in length as described in Chapter 4) and PS-*b*-PMMA block copolymer were prepared, in this case with 50, 60 and 70 wt % TiO<sub>2</sub> nanorod contents.

ITO coated glass substrate was firstly cleaned by sonication in deionized water for 15 min, followed by sonication in acetone for 30 min, sonication in 2-propanol for 30 min and finally sonication in deionized water again for 30 min. Electro-devices were fabricated as follows. Two PEDOT:PSS layers were spin-coated onto previously cleaned ITO glass substrate and subsequently dried at 120 °C for 10 min under vacuum. Then, the P3HT layer was deposited by spin-coating a 15 mg/mL P3HT solution in chlorobenzene onto the PEDOT:PSS layer. The films were dried at 140 °C for 15 min. Finally, the TiO<sub>2</sub>NR/PS-*b*-PMMA nanocomposite layer was spin-coated. For comparison, electro-devices based on pristine TiO<sub>2</sub> nanorods, as last active layer of electro-device, were also fabricated. All layers were deposited at 2000 rpm for 120 s.

### 5.2.3. Characterization techniques

#### 5.2.3.1. Atomic force microscopy

AFM images were obtained with a Nanoscope IIIa scanning probe microscope (Multimode, Digital Instruments). Tapping mode (TM) was employed in air using an

integrated tip/cantilever (125  $\mu\text{m}$  in length with ca. 300 kHz resonant frequency). Typical scan rates during recording were 0.7 to 1 line/s using a scan head with a maximum range of 15  $\mu\text{m}$   $\times$  15  $\mu\text{m}$ . Several replicates were prepared per each electro-device and different zones per each electro-device were investigated by AFM, in order to assess the uniformity of the films.

#### 5.2.3.2. Keithley semiconductor analyzer

Semiconductor characterization system (Keithley model 4200-SCS) was used to study the surface conductive properties of the investigated electro-devices. Two-point experiments were carried out applying a voltage sweep from -6 to 6 V to study the conductive properties at the macroscopic level. The sheet resistivity was measured by the four-point collinear probe method with 100 mA current.

#### 5.2.3.3. Tunneling atomic force microscopy

Quantitative nanoconductive properties of the investigated electro-devices were measured by using tunneling atomic force microscopy (TUNA) with a Dimension Icon scanning probe microscope equipped with Nanoscope V controller (Bruker). The measurements were carried out using PeakForce TUNA mode under ambient conditions and applying -6 V and 6 V voltages. The PeakForce TUNA probe was equipped with a Pt/Ir coating tip.

#### 5.2.3.4. Ultraviolet-visible spectroscopy

UV-vis absorption spectra of the fabricated devices were recorded by using a spectrophotometer (Shimadzu UV-3600) in the range between 200 and 800 nm.

### 5.3. Results and discussion

#### 5.3.1. Characterization of ITO-glass/PEDOT:PSS/P3HT/(TiO<sub>2</sub>NR/PS-*b*-PMMA) electro-devices

In the fabricated electro-devices [3,4], TiO<sub>2</sub> acts as the carrier transport material, whereas P3HT is an effective hole transport material in its regioregular form [5]. The

combination of polymers with inorganic semiconductors like TiO<sub>2</sub> nanocrystals favors the charge transfer between the high electron affinity inorganic semiconductor and the relatively low ionization potential organic molecules and polymers [17-19]. The top layer of the devices was the one that was varied in order to investigate the effect of the TiO<sub>2</sub> nanorod content on the conductive properties of the electro-devices.

#### 5.3.1.1. Morphology

Apart from the study of the electro-devices based on TiO<sub>2</sub>NR/PS-*b*-PMMA nanocomposites, a system based on pristine TiO<sub>2</sub> nanorods, as top layer, was preliminarily investigated as a reference. The morphology of the electro-devices fabricated with the pristine TiO<sub>2</sub> nanorods as well as with TiO<sub>2</sub>NR/PS-*b*-PMMA nanocomposites with 50, 60 and 70 wt % TiO<sub>2</sub> nanorods was studied by AFM. The phase images of all investigated electro-devices can be seen in **Figure 5.1**.

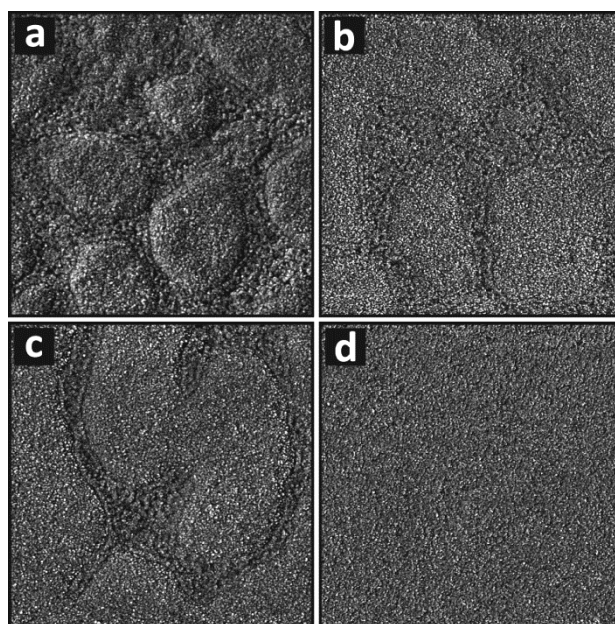


**Figure 5.1.** AFM phase images (3  $\mu\text{m}$  x 3  $\mu\text{m}$ ) of ITO-glass/PEDOT:PSS/P3HT/(TiO<sub>2</sub>NR/PS-*b*-PMMA) electro-devices fabricated with 50 (a), 60 (b) and 70 (c) wt % TiO<sub>2</sub>NR/PS-*b*-PMMA nanocomposite layer and of ITO-glass/PEDOT:PSS/P3HT/TiO<sub>2</sub>NR electro-device (d).

The AFM images showed regular and homogeneous surfaces where TiO<sub>2</sub> nanorods appeared well-dispersed visible as small white spots. In the case of the electro-devices with a layer of TiO<sub>2</sub>NR/PS-*b*-PMMA nanocomposite (**Figures 5.1a, 5.1b and 5.1c**), the surfaces presented a distinctive nanostructured morphology. Indeed, some brighter zones present on the surface and ascribable mostly to TiO<sub>2</sub> nanorods

show different shape and size in each analyzed device. In any case, the surfaces appear homogeneously covered by the TiO<sub>2</sub> nanorods. The AFM phase image for the electro-device based on pristine TiO<sub>2</sub> nanorods (**Figure 5.1d**) exhibited white spots, ascribable to TiO<sub>2</sub> nanorods, well dispersed on the surface.

Clearly, while the overall morphology of the systems accounts for all the layers forming the system, the top layer nanocomposite morphology particularly affects the electro-device characteristics.

In addition to this, AFM investigation was also carried out on purposely scratched electro-devices to measure the thickness of various systems. Therefore the thickness of the prepared systems resulted of 175±5 nm for those based on pristine TiO<sub>2</sub> nanorods, whereas it was 93±5 nm for the TiO<sub>2</sub>NR/PS-*b*-PMMA nanocomposite films. All the measured films were deposited onto an ITO layer, which is about 120-160 nm thick according to the supplier specifications.

#### 5.3.1.2. Conductive properties

Conductive properties of the fabricated electro-devices were investigated by Keithley semiconductor analyzer and TUNA. First, it should be pointed out that, as was detailed in Chapter 2, these two techniques account for different phenomena, which are the current on the investigated film surfaces, hence a macroscale measurement, in the case of the semiconductor analyzer, and the current through the whole electro-devices, that is detected at local nanoscale, in the case of TUNA.

Conductive properties at macroscale of fabricated electro-devices were measured by means of a Keithley semiconductor analyzer operating in two-point mode. Current-voltage (I-V) curves for each electro-device were recorded by applying a voltage sweep between -6 and 6 V. **Figure 5.2** shows the current-voltage curves corresponding to all investigated electro-devices.

Devices based on TiO<sub>2</sub>NR/PS-*b*-PMMA nanocomposites displayed intensity currents that increase up to 30 nA with higher TiO<sub>2</sub> nanorod contents. This indicates that TiO<sub>2</sub> nanorods present a conductive behavior, as was observed in Chapter 4, but the current values measured for electro-devices based on nanocomposites are much higher than the values obtained in Chapter 4 for TiO<sub>2</sub>NR/PS-*b*-PMMA nanocomposites.

In addition, it should be noted that the conductive behavior of such nanorods can be attributed to the geometry of the nanorod that enables more effective percolation paths for electrical transport in comparison to other geometries, in agreement with Huynh et al [5]. This evidence confirms the efficiency of  $\text{TiO}_2$  nanorods as charge carriers [5,20].

On the other hand, the reference system electro-device based on pristine  $\text{TiO}_2$  nanorods, as a top layer, points out very low currents, not higher than 200 pA, in comparison with the ones fabricated using the hybrid inorganic/organic nanocomposites. Therefore, these evidences strongly highlight the role of the PS-*b*-PMMA block copolymer in directing the organization of the nanorods into superstructures able to enhance the inter-particle connection, and thus generate effective percolating networks for charge carrier transport, ultimately affecting the conductivity of the systems [19,21].

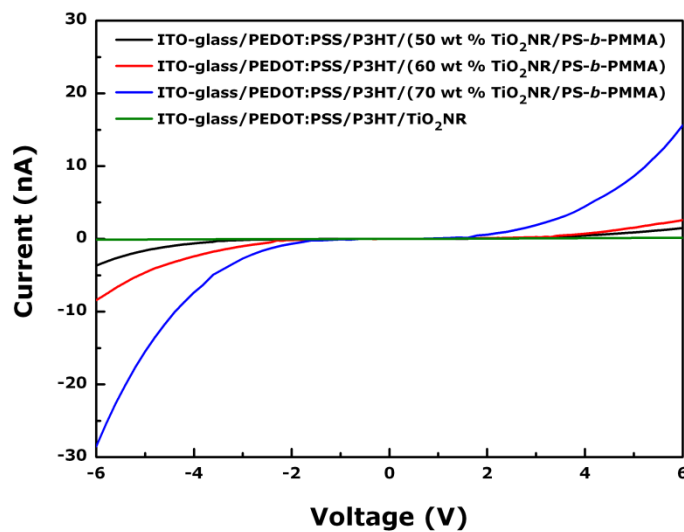


**Figure 5.2.** Current-voltage (I-V) curves of ITO-glass/PEDOT:PSS/P3HT/( $\text{TiO}_2\text{NR}/\text{PS-}b\text{-PMMA}$ ) electro-devices fabricated with 50, 60 and 70 wt %  $\text{TiO}_2\text{NR}/\text{PS-}b\text{-PMMA}$  nanocomposite layer and of ITO-glass/PEDOT:PSS/P3HT/ $\text{TiO}_2\text{NR}$  electro-device, by applying a voltage sweep between -6 and 6 V.

The electro-devices based on  $\text{TiO}_2\text{NR}/\text{PS-}b\text{-PMMA}$  nanocomposites, that presented the highest intensity currents, were then also analyzed by the four-point collinear probe method with the Keithley semiconductor analyzer in order to determine the sheet resistivity of the devices [22,23]. Sheet resistivity allows to easily calculate the electrical resistivity as well as the electrical conductivity of the investigated devices (**Table 5.1**). The lowest sheet resistivity and the highest

conductivity values were found for the 60 wt % TiO<sub>2</sub>NR/PS-*b*-PMMA nanocomposite based electro-device, whereas the highest sheet resistivity and the lowest conductivity was for the 50 wt % TiO<sub>2</sub>NR/PS-*b*-PMMA nanocomposite device. In general the values obtained for sheet resistivity are of the same order of magnitude of the values reported in literature for composite films containing TiO<sub>2</sub> nanoparticles [24].

**Table 5.1.** Sheet resistivity, thickness, electrical resistivity and conductivity values calculated for the selected electro-devices.

Electro-device	Sheet resistivity <sup>a</sup> (Ω/sq)	Thickness (cm)	Electrical resistivity <sup>b</sup> (Ω·cm)	Conductivity <sup>c</sup> (S/cm)
ITO-glass/PEDOT:PSS/P3HT/ (50 wt % TiO <sub>2</sub> NR/PS- <i>b</i> -PMMA)	43.33 ± 10.19	2.33 × 10 <sup>-5</sup>	1.01 × 10 <sup>-3</sup>	990.57
ITO-glass/PEDOT:PSS/P3HT/ (60 wt % TiO <sub>2</sub> NR/PS- <i>b</i> -PMMA)	37.34 ± 4.77	2.33 × 10 <sup>-5</sup>	8.70 × 10 <sup>-4</sup>	1149.53
ITO-glass/PEDOT:PSS/P3HT/ (70 wt % TiO <sub>2</sub> NR/PS- <i>b</i> -PMMA)	38.94 ± 6.28	2.33 × 10 <sup>-5</sup>	9.07 × 10 <sup>-4</sup>	1102.20

<sup>a</sup>Values directly calculated from the four-point collinear probe measurements.

<sup>b</sup> $\rho = R_s \cdot t$  ( $\rho$ : electrical resistivity,  $R_s$ : sheet resistivity,  $t$ : thickness)

<sup>c</sup> $\sigma = 1/\rho$  ( $\sigma$ : conductivity)

Regarding the conductive properties at nanoscale, these were investigated by TUNA. TUNA images and TUNA current profiles corresponding to a horizontal cross section of the TUNA images of the ITO-glass/PEDOT:PSS/P3HT/(TiO<sub>2</sub>NR/PS-*b*-PMMA) electro-devices with different TiO<sub>2</sub> nanorod contents and of the ITO-glass/PEDOT:PSS/P3HT/TiO<sub>2</sub>NR electro-device, applying 6 V, are reported in **Figure 5.3**.

TUNA measurements performed on the electro-devices highlighted that no response could be detected in any electro-device (results not shown) when a negative voltage (-6 V) was applied to the TUNA tip. On the contrary, applying a positive voltage (6 V) to the tip, all the analyzed electro-devices exhibited TUNA currents passing through the system. TUNA images clearly showed bright conductive areas almost on the whole surface of the electro-devices based on the nanocomposites containing 50, 60 and 70 wt % TiO<sub>2</sub> nanorods, respectively. These bright areas appeared as islands on the investigated surfaces, and their position is in agreement with the morphology detected in the AFM images, as the areas with the highest TUNA currents correspond

to those where aggregated of  $\text{TiO}_2$  nanorods are present, while dark areas do not provide any response to the applied voltage. In the case of the electro-device based on the pristine  $\text{TiO}_2$  nanorods, the presence of TUNA currents was also clearly related to the presence of  $\text{TiO}_2$  nanorods since the conductive spots are noticeably in accordance with the bright spots in the AFM phase image of this electro-device. Thus, conductive spots appeared uniformly dispersed on the surface of the device.

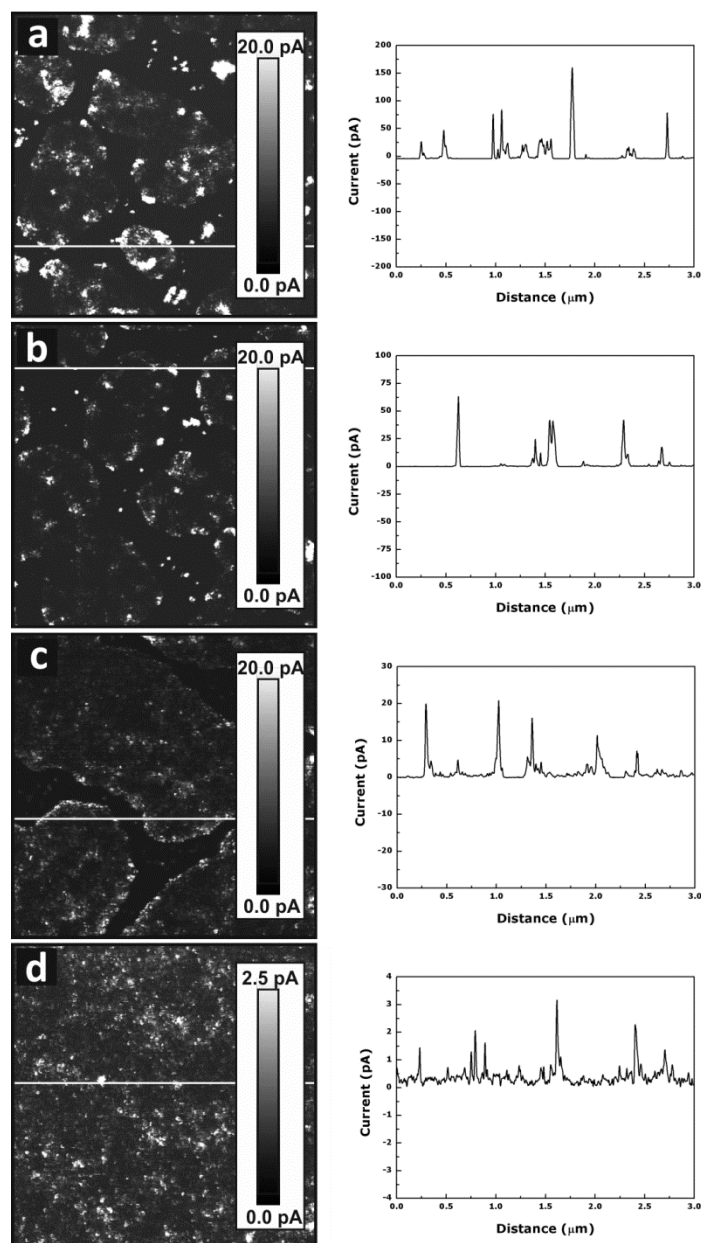


**Figure 5.3.** TUNA images ( $3 \mu\text{m} \times 3 \mu\text{m}$ ) taken at 6 V of ITO-glass/PEDOT:PSS/P3HT/ $(\text{TiO}_2\text{NR}/\text{PS}-b\text{-PMMA})$  electro-devices fabricated with 50 (a), 60 (b) and 70 (c) wt %  $\text{TiO}_2\text{NR}/\text{PS}-b\text{-PMMA}$  nanocomposite layer and of ITO-glass/PEDOT:PSS/P3HT/ $\text{TiO}_2\text{NR}$  electro-device (d). The graphs correspond to the current profiles marked on the TUNA images.

Moreover, the current values reported in the TUNA current profiles did not show a dependence on the  $\text{TiO}_2$  nanorod content in the top layer of each nanocomposite based electro-device. In fact, the 50 wt %  $\text{TiO}_2\text{NR}/\text{PS-}b\text{-PMMA}$  based electro-device showed the highest current value, while the lowest value was recorded for the 70 wt %  $\text{TiO}_2\text{NR}/\text{PS-}b\text{-PMMA}$  based one. This feature could be explained by the fact that a very high nanorod content can turn in a more extended formation of large aggregates, and, consequently in less efficient conductive paths.

However, TUNA measurements showed significant current values for electro-devices based on nanocomposites, 20-300 pA approximately, in comparison to the currents passing through the electro-device based on pristine  $\text{TiO}_2$  nanorods, that were lower than 5 pA. This evidence, on the one hand, confirms the high conductive behavior of these electro-devices as a result of the beneficial effect of the rod-like shape nanoparticles in forming effective percolating pathways, and thus improving charge transport in electro-devices such as in particular photovoltaic devices [5,20,25]. On the other hand, this suggests that the incorporation of the nanorods into the host block copolymer results to effectively direct the nanorod organization in a highly interconnected structure, which turns much more effective in electrical transport and hence ultimately in a device with higher currents [19,21]. Interestingly the trends of the results obtained by TUNA measurements and by using the semiconductor analyzer are in agreement, in spite of the fact that the two techniques accounts, actually, for different phenomena, as pointed out above.

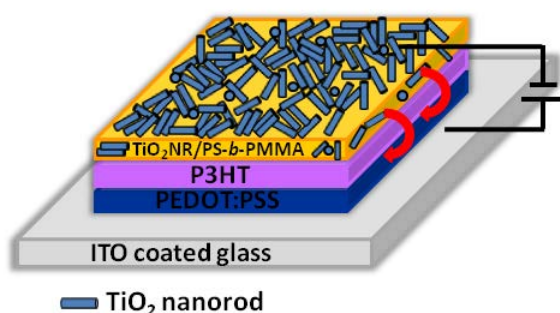


**Figure 5.4.** Schematic representation of the fabricated electro-devices based on  $\text{TiO}_2\text{NR}/\text{PS-}b\text{-PMMA}$  nanocomposites.

Finally, **Figure 5.4** describes the conductive behavior of fabricated electro-devices, with  $\text{TiO}_2\text{NR}/\text{PS-}b\text{-PMMA}$  nanocomposites. The geometry of the  $\text{TiO}_2$  nanorods make them clearly prone to assemble in the host polymer to form effective

pathway, as demonstrated by the current values detected for TiO<sub>2</sub>NR/PS-*b*-PMMA nanocomposite based electro-devices.

### 5.3.1.3. Optical properties

The absorption spectra of all fabricated electro-devices are shown in **Figure 5.5**. UV-vis spectra exhibited an absorption in the region below 650 nm, which can be ascribed to the  $\pi$ - $\pi^*$  transition of the P3HT, and an intense feature can be detected in the UV region below 400 nm, attributed to the TiO<sub>2</sub> nanorods. The influence of the content of TiO<sub>2</sub> nanorods can be noticed in the absorbance intensity in the range 400-650 nm, which can be found proportional to the TiO<sub>2</sub> content. Therefore, it can be claimed that these electro-devices have an absorption range from visible to ultraviolet, which agrees well with solar irradiation [26]. It is worthwhile to point out that the presence of nanocrystalline TiO<sub>2</sub> strengthens the UV absorption of P3HT, thus making the nanocomposites more suited for solar energy conversion based application.

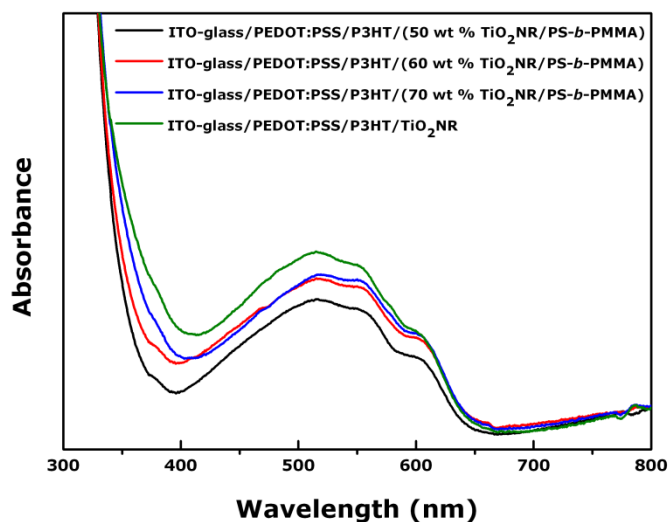


**Figure 5.5.** UV-vis absorption spectra of ITO-glass/PEDOT:PSS/P3HT/(TiO<sub>2</sub>NR/PS-*b*-PMMA) electro-devices fabricated with 50, 60 and 70 wt % TiO<sub>2</sub>NR/PS-*b*-PMMA nanocomposite layer and of ITO-glass/PEDOT:PSS/P3HT/TiO<sub>2</sub>NR electro-device.

## 5.4. Conclusions

Different electro-devices were successfully fabricated using TiO<sub>2</sub> nanorods embedded in the PS-*b*-PMMA host matrix in order to investigate the influence of the

TiO<sub>2</sub> nanorod content on the conductive properties of the resulting systems. For this purpose, organic capped TiO<sub>2</sub> nanorods were prepared in rod-like shape, and embedded in PS-*b*-PMMA block copolymer at increasing contents and using such nanocomposites as top layers in electro-devices. In addition, a reference system was prepared by using pristine TiO<sub>2</sub> nanorods.

The AFM surface characterization of the top layer of all prepared electro-devices showed nanorods dispersed on the whole investigated surface, and, in particular, the nanocomposites based systems display nanostructured morphology, accounting for the templating role of PS-*b*-PMMA host in directing the organization of TiO<sub>2</sub> nanorods.

UV-vis absorption spectra assessed the optical characteristics of the prepared electro-devices, showing that the TiO<sub>2</sub> strengthens the absorption in the UV range, thus widening the range of solar spectrum available for energy conversion applications. The conductive properties of electro-devices were investigated at nanoscale by TUNA and at macroscale by Keithley semiconductor analyzer. Results indicated that the presence of block copolymer improved the conductive response in comparison to the system prepared with the pristine nanorods.

The conductive and optical properties of the TiO<sub>2</sub>NR/PS-*b*-PMMA nanocomposites based electro-devices proved that the use of block copolymer leads to a morphological control on the inorganic semiconductor nanorods organization, resulting in a more effective percolation path, particularly beneficial for enhancing carrier transport and thus conductivity, features that can be conveniently exploited in a variety of energy conversion applications, including innovative solar cell fabrication.

## 5.5. References

- [1] S. Günes, H. Neugebauer, N. S. Sariciftci, *Chem. Rev.* 2007, **107**, 1324-1338.
- [2] Y. J. Cheng, S. H. Yang, C. S. Hsu, *Chem. Rev.* 2009, **109**, 5868-5923.
- [3] J. Xiong, B. Yang, C. Zhou, J. Yang, H. Duan, W. Huang, X. Zhang, X. Xia, L. Zhang, H. Huang, Y. Gao, *Org. Electron.* 2014, **15**, 835-843.
- [4] K. Sasaki, T. Yamanari, S. Takano, Y. Yoshida, Y. Ueda, *Jpn. J. Appl. Phys.* 2012, **51**, 090203/1-090203/3.
- [5] W. U. Huynh, J. J. Dittmer, A. P. Alivisatos, *Science* 2002, **295**, 2425-2427.

- [6] A. C. Mayer, S. R. Scully, B. E. Hardin, M. W. Rowell, M. D. McGehee, *Mater. Today* 2007, **10**, 28-33.
- [7] Y. S. Kim, T. Kim, B. Kim, D. K. Lee, H. Kim, B. K. Ju, K. Kim, *Org. Electron.* 2013, **14**, 1749-1754.
- [8] J. Gutierrez, A. Tercjak, M. D. Martin, I. Mondragon, *Electrochim. Acta* 2011, **56**, 5582-5586.
- [9] W. Maiaugree, S. Pimanpang, M. Towannang, S. Saekow, W. Jarernboon, V. Amornkitbamrung, *J. Non-Cryst. Solids* 2012, **358**, 2489-2495.
- [10] N. N. Dinh, D. N. Chung, T. T. Thao, D. Hui, *J. Nanomater.* 2012, **2012**, 190290/1-190290/6.
- [11] I. Okada, S. Shiratori, *ACS Appl. Mater. Interfaces* 2013, **5**, 4144-4149.
- [12] E. Gondek, Y. Djaoued, J. Robichaud, P. Karasinski, I. V. Kityk, A. Danel, K. J. Plucinski, *J. Mater. Sci.: Mater. Electron* 2012, **23**, 2057-2064.
- [13] J. T. Park, R. Patel, H. Jeon, D. J. Kim, J. S. Shin, J. H. Kim, *J. Mater. Chem.* 2012, **22**, 6131-6138.
- [14] S. K. Pathak, A. Abate, P. Ruckdeschel, B. Roose, K. C. Gödel, Y. Vaynzof, A. Santhala, S. I. Watanabe, D. J. Hollman, N. Noel, A. Sepe, U. Wiesner, R. Friend, H. J. Snaith, U. Steiner, *Adv. Funct. Mater.* 2014, **24**, 6046-6055.
- [15] B. P. Nguyen, T. Kim, C. R. Park, *J. Nanomater.* 2014, **2014**, 243041/1-243041/20.
- [16] R. Liu, *Materials* 2014, **7**, 2747-2771.
- [17] N. C. Greenham, X. Peng, A. P. Alivisatos, *Phys. Rev. B Condens. Matter.* 1996, **54**, 17628-17637.
- [18] D. S. Ginger, N. C. Greenham, *Phys. Rev. B Condens. Matter.* 1999, **59**, 10622-10629.
- [19] M. Nedelcu, S. Guldin, M. C. Orilall, J. Lee, S. Hüttner, E. J. W. Crossland, S. C. Warren, C. Ducati, P. R. Laity, D. Eder, U. Wiesner, U. Steiner, H. J. Snaith, *J. Mater. Chem.* 2010, **20**, 1261-1268.
- [20] P. D. Cozzoli, A. Kornowski, H. Weller, *J. Am. Chem. Soc.* 2003, **125**, 14539-14548.
- [21] E. J. W. Crossland, M. Nedelcu, C. Ducati, S. Ludwigs, M. A. Hillmyer, U. Steiner, H. J. Snaith, *Nano Lett.* 2009, **9**, 2813-2819.
- [22] N. Politakos, E. Grana, I. Zalakain, D. Katsigiannopoulos, A. Eceiza, G. Kortaberria, A. Avgeropoulos, *J. Appl. Polym. Sci.* 2014, **131**, 40084/1-40084/10.

- [23] S. Kim, S. Y. Kim, J. Kim, J. H. Kim, *J. Mater. Chem. C* 2014, **2**, 5636-5643.
- [24] X. Zhao, M. Li, D. Song, P. Cui, Z. Zhang, Y. Zhao, C. Shen, Z. Zhang, *Nanoscale Res. Lett.* 2014, **9**, 202/1-202/5.
- [25] A. Petrella, M. Tamborra, M. L. Curri, P. Cosma, M. Striccoli, P. D. Cozzoli, A. Agostiano, *J. Phys. Chem. B* 2005, **109**, 1554-1562.
- [26] H. Wei, H. Gong, Y. Wang, X. Hu, L. Chen, H. Xu, P. Liu, B. Cao, *CrystEngComm* 2011, **13**, 6065-6070.

**6**

**Polystyrene-*block*-polymethyl  
methacrylate diblock copolymer  
and synthesized  $\gamma$ -Fe<sub>2</sub>O<sub>3</sub> nanocrystals  
based nanocomposites**



## 6. Polystyrene-*block*-polymethyl methacrylate diblock copolymer and synthesized $\gamma\text{-Fe}_2\text{O}_3$ nanocrystals based nanocomposites

In this Chapter, the same PS-*b*-PMMA block copolymer as in the previous Chapters has been used in order to prepare novel hybrid inorganic/organic nanocomposites. In this case, the inorganic part incorporated into the self-assembled PS-*b*-PMMA block copolymer has been  $\gamma\text{-Fe}_2\text{O}_3$  nanocrystals ( $\gamma\text{-Fe}_2\text{O}_3\text{NC}$ ), which were synthesized, as in Chapters 4 and 5, by means of a surfactant-assisted colloidal synthetic approach. The colloidal synthesis led to organic-coated magnetic  $\gamma\text{-Fe}_2\text{O}_3$  maghemite nanocrystals, which resulted to be well-dispersed in the block copolymer up to high contents. Thus,  $\gamma\text{-Fe}_2\text{O}_3\text{NC}/\text{PS-}b\text{-PMMA}$  nanocomposites were obtained containing different amounts of  $\gamma\text{-Fe}_2\text{O}_3$  nanocrystals, and were characterized mainly from the point of view of their morphology at nanoscale and their magnetic properties, analyzing the influence of the different  $\text{TiO}_2$  nanorod content on the final properties of the nanocomposites.

The work presented in this Chapter was carried out during a three months research period spent at the Institute for Physical and Chemical Processes of the Italian National Research Council, located in Bari, Italy, under the supervision of the Dr. Lucia Curri, and financed by the COST Action CM1101 Colloidal Aspects of Nanoscience for Innovative Processes and Materials.

### 6.1. Introduction

Among different kinds of inorganic nanoparticles, iron oxide nanoparticles, in particular, are of great interest due to their several applications, in high density magnetic recording media, sensors, catalysts, and pharmaceutical and biomedical fields [1,2]. However, several factors, such as nanoparticle shape, size distribution, surface chemistry as well as magnetization value, are critical and have to be taken into account for using iron oxide nanoparticles for specific applications. For instance, pharmaceutical and biomedical applications require magnetic nanoparticles characterized by very small size and narrow size distribution, along with high magnetization values [3,4]. Both magnetite ( $\text{Fe}_3\text{O}_4$ ) and maghemite ( $\gamma\text{-Fe}_2\text{O}_3$ ) are the

most employed iron oxide nanoparticles. They are biocompatible and biodegradable, and very similar materials in terms of structure and magnetic properties, which makes them difficult to be distinguished, although maghemite has a higher chemical stability with respect to magnetite.

Recently, many researchers have studied the employment of magnetic nanoparticles as nanofillers in block copolymer matrices [5-10]. Beside a wide range of different synthesis methods, which result in different types of iron oxide nanoparticles, also, a series of diverse block copolymer host matrices have been considered as self-assembled templates for the preparation of nanocomposites.

In this sixth Chapter, a simple preparation procedure based on the thermal decomposition of  $\text{Fe}(\text{CO})_5$  was followed for the synthesis of maghemite nanoparticles, which allowed to obtain monodisperse oleic acid- and oleylamine-capped  $\gamma\text{-Fe}_2\text{O}_3$  nanocrystals with a narrow size distribution. Interestingly the used preparative route allowed to synthesize organic-coated nanocrystals, with a surface chemistry compatible with one of the blocks in the block copolymer, as in Chapters 4 and 5, without the need of any post synthetic treatment devoted to the chemical functionalization of the nanocrystal surface. Indeed the use of oleic acid and oleylamine as surfactants, while essential for the control of the nanocrystal size and shape during the synthesis, enabled their prompt incorporation into the PS-*b*-PMMA block copolymer, used as a host template. Thus,  $\gamma\text{-Fe}_2\text{O}_3$  nanocrystal colloidal solutions in toluene were prepared *ex situ* and subsequently incorporated into the PS-*b*-PMMA block copolymer matrix. The self-assembly ability of the block copolymer, with absence of any thermal or solvent treatments, led to well nanostructured nanocomposites.

The morphological, structural and chemical characterization of  $\gamma\text{-Fe}_2\text{O}_3$  nanocrystals, in terms of their size, shape and chemical surface, was performed by TEM and FTIR, respectively. Nanocomposites based on PS-*b*-PMMA block copolymer were investigated at increasing  $\gamma\text{-Fe}_2\text{O}_3$  nanocrystal content by AFM and SEM to study their nanoscale morphology. The ensemble of characterization tools allowed to define the nanocrystal location within the block copolymer template. Finally, magnetic properties of nanocomposites were studied by using MFM technique, pointing out that the magnetic nanocrystals dispersed in the PS phase led to the detection of magnetic nanodomains.

## 6.2. Materials and methods

### 6.2.1. Materials

PS-*b*-PMMA diblock copolymer, with the same polydispersity index ( $M_w/M_n = 1.17$ ) and number-average molecular weights ( $M_{nPS} = 83000$  g/mol and  $M_{nPMMA} = 92500$  g/mol) as the one employed in Chapters 4 and 5, was purchased from Polymer Source and used.

For the synthesis of  $\gamma$ -Fe<sub>2</sub>O<sub>3</sub> nanocrystals, iron pentacarbonyl (Fe(CO)<sub>5</sub>, 99.99 %), oleic acid (C<sub>17</sub>H<sub>33</sub>CO<sub>2</sub>H or OLEA, 90 %), dodecan-1,2-diol (C<sub>12</sub>H<sub>24</sub>(OH)<sub>2</sub> or DDIOL, 90 %), 1-octadecene (C<sub>18</sub>H<sub>36</sub> or ODE, 90 %) and oleylamine (C<sub>18</sub>H<sub>35</sub>NH<sub>2</sub> or OLEAM, 70 %) were purchased from Aldrich. Acetone, 2-propanol, chloroform and toluene were purchased from Aldrich too.

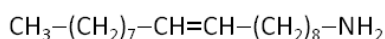


**Figure 6.1.** Chemical structure of the oleylamine.

### 6.2.2. Synthesis of $\gamma$ -Fe<sub>2</sub>O<sub>3</sub> nanocrystals

$\gamma$ -Fe<sub>2</sub>O<sub>3</sub> nanocrystals were synthesized by following a procedure previously reported in the literature [11,12]. A mixture containing ODE (20 mL), DDIOL (2.5 mmol), OLEAM (1.5 mmol) and OLEA (3 mmol) was loaded into a three-necked flask connected to a reflux condenser. It was stirred for 30 min at 110 °C under vacuum and then heated under N<sub>2</sub> flow to 250 °C. Subsequently, 1 mL of Fe(CO)<sub>5</sub> solution (1M) in degassed ODE was quickly added to the vigorously stirred mixture. A change in the solution color from yellowish to black was observed. After 1 h stirring at 250 °C, the temperature was lowered to 130 °C and the flask was exposed to air and kept at this temperature for 1 h. Finally, the reaction mixture was cooled to room temperature. The obtained iron oxide nanocrystals were precipitated from the reaction mixture upon the addition of a solution containing 2-propanol and acetone (1:1), isolated by centrifugation and redispersed in chloroform. This washing procedure was repeated several times and finally the nanocrystals were dispersed in toluene. The iron oxide nanocrystals obtained by this synthesis procedure were reported to be mainly formed of  $\gamma$ -Fe<sub>2</sub>O<sub>3</sub> maghemite nanocrystals [11].

### 6.2.3. $\gamma$ -Fe<sub>2</sub>O<sub>3</sub> NC/PS-*b*-PMMA nanocomposite preparation

Block copolymer solution was prepared by dissolving a specific quantity of PS-*b*-PMMA block copolymer in toluene. The solution was stirred for few hours at ambient temperature, then  $\gamma$ -Fe<sub>2</sub>O<sub>3</sub>NC/PS-*b*-PMMA nanocomposite solutions were prepared by adding adequate volumes of  $\gamma$ -Fe<sub>2</sub>O<sub>3</sub> nanocrystal dispersion to the block copolymer solution (concentration 5 mg/mL), in order to achieve  $\gamma$ -Fe<sub>2</sub>O<sub>3</sub> nanocrystal content in the range from 1 to 60 wt % with respect to the block copolymer. All investigated nanocomposite solutions were stirred for 4 hours and then both nanocomposite and block copolymer solutions were spin-coated (Headway Research EC101DT spin-coater) onto freshly cleaned silicon wafer substrates at 2000 rpm for 120 s. The obtained thin films were dried in ambient conditions.

The silicon wafers were previously cleaned by means of sonication at room temperature in methanol for 10 min and in acetone for further 10 min, rinsing them with 2-propanol after each sonication. Subsequently, the substrates were dried under N<sub>2</sub> flow and soaked for 10 min in Piranha solution (3:1 sulphuric acid/hydrogen peroxide). Afterwards they were rinsed with ultrapure water (Millipore, 18.2 M $\Omega$ ·cm, organic carbon content  $\leq$ 4  $\mu$ g/L) and 2-propanol, dried again under N<sub>2</sub> flow and directly used as substrates.

### 6.2.4. Characterization techniques

#### 6.2.4.1. Fourier transform infrared spectroscopy

Infrared spectra were carried out using a Nicolet Nexus FTIR spectrometer equipped with ATR Golden Gate, with a 2 cm<sup>-1</sup> resolution in a wavenumber range between 4000 and 400 cm<sup>-1</sup>. The solution was deposited on the diamond crystal allowing the evaporation of the solvent before doing the measurement.

#### 6.2.4.2. Transmission electron microscopy

TEM measurements were carried out by using a JEOL JEM-1011 microscope, working at an accelerating voltage of 100 kV. The images were acquired using a Quemesa Olympus CCD 11 Mp Camera. The  $\gamma$ -Fe<sub>2</sub>O<sub>3</sub> nanocrystals were deposited by drop casting onto carbon-coated copper grids. Size statistical analyses (nanocrystal

average size and size distribution) of the samples were performed by using a freeware image analysis program (ImageJ).

#### 6.2.4.3. Atomic force microscopy

AFM images were obtained under ambient conditions with a Nanoscope IIIa scanning probe microscope (Multimode, Digital Instruments). Tapping mode (TM) was employed in air using an integrated tip/cantilever (125  $\mu\text{m}$  in length with ca. 300 kHz resonant frequency). Typical scan rates during recording were 0.7 to 1 line/s using a scan head with a maximum range of 15  $\mu\text{m}$   $\times$  15  $\mu\text{m}$ . Several replicates were prepared per each composition and different zones per each thin film were investigated by AFM, in order to assess the uniformity of the films.

#### 6.2.4.4. Scanning electron microscopy

Scanning electron microscopy (SEM) micrographs were acquired with a ZEISS SUPRA-55 VP Field Emission SEM, equipped with SmartSEM V 05.00 software, using secondary electrons. A low accelerating voltage of about 1.5 kV was applied, allowing to reduce the charging on the surface of the insulating block copolymer, thus enabling to image the block copolymer based samples without deposition of conductor materials.

#### 6.2.4.5. Magnetic force microscopy

MFM measurements were performed using a Dimension Icon scanning probe microscope equipped with Nanoscope V controller (Bruker). Measurements were performed using a Lift-Mode (lift height was around 100 nm) equipped with an integrated Co/Cr-coated MESP tip having a resonance frequency around 75 kHz and a nominal radius of curvature of 25 nm. The secondary imaging mode derived from the tapping mode that measures the magnetic field gradient distribution above the thin film surface was detected by magnetizing the tip prior to MFM measurement. Locally magnetized domains on the thin film surface were qualitatively mapped simultaneously with the height and phase AFM images. In order to degrade the organic part of the sample and thus possibly enhance the magnetic response of samples upon MFM investigation, selected nanocomposite thin films were exposed to a 254 nm UV light (XX-15S, UVP Inc.) for 24 hours.

## 6.3. Results and discussion

### 6.3.1. Characterization of the synthesized $\gamma$ -Fe<sub>2</sub>O<sub>3</sub> nanocrystals

$\gamma$ -Fe<sub>2</sub>O<sub>3</sub> nanocrystals employed for the fabrication of nanocomposites based on PS-*b*-PMMA block copolymer were synthesized by thermal decomposition of iron pentacarbonyl precursor in octadecene, in presence of a mixture of surfactants, namely oleic acid and oleylamine, followed by oxidation under air. The  $\gamma$ -Fe<sub>2</sub>O<sub>3</sub> nanocrystals, prepared by following such a synthetic procedure [11,12] are capped with oleic acid and oleylamine, which are responsible for controlling the growth of the nanocrystals during the synthesis and, at the same time, make them dispersible and stable in organic solvents. Remarkably the surfactant agents coordinating nanocrystal surface impart them chemical compatibility with the polymeric matrix in which they may be incorporated [11].

**Figure 6.2** shows the TEM image and FTIR spectrum of the  $\gamma$ -Fe<sub>2</sub>O<sub>3</sub> nanocrystals. As can be clearly distinguished from TEM image (**Figure 6.2a**), the nanocrystals have a mean particle size of around 7 nm and a percentage relative standard deviation ( $\sigma$  %) of about 20 %, and present a shape between triangular and spherical.

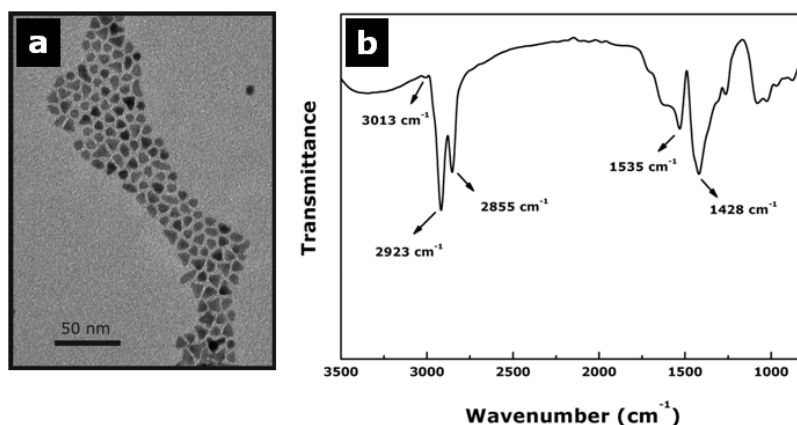


**Figure 6.2.** TEM micrograph (a) and FTIR spectrum (b) of oleic acid- and oleylamine-coated  $\gamma$ -Fe<sub>2</sub>O<sub>3</sub> nanocrystals.

The infrared spectrum of  $\gamma$ -Fe<sub>2</sub>O<sub>3</sub> nanocrystals in toluene, shown in **Figure 6.2b**, confirmed the presence of an organic capping layer surrounding the inorganic nanocrystals.  $\gamma$ -Fe<sub>2</sub>O<sub>3</sub> nanocrystals presented a weak signal at 3013 cm<sup>-1</sup> attributable to the olefinic C-H stretching vibrations of the oleic acid and the oleylamine [13-15], as was also seen in the spectrum of the TiO<sub>2</sub> nanorods in Chapter 4, which indicated that

such coordinating molecules are present on the nanocrystal surface. The two intense peaks at 2923 and 2855  $\text{cm}^{-1}$  corresponded, respectively, to asymmetric and symmetric C-H stretching vibrations of the  $-\text{CH}_2-$  groups in the alkyl chain of the oleic acid and oleylamine [15]. Moreover, the spectrum showed other two characteristic bands at 1535 and 1428  $\text{cm}^{-1}$ , which can be assigned to stretching vibrations of carboxylate ( $\text{COO}^-$ ) anions linked to surface metal centers [13-15]. The strength of these ( $\text{COO}^-$ ) peaks, and the lack of a definite signal related to the amine group, suggested that the surface of synthesized  $\gamma\text{-Fe}_2\text{O}_3$  nanocrystals is mainly covered by the oleic acid, which coordinates the nanocrystal surface more strongly than oleylamine as previously reported [16,17].

### 6.3.2. Characterization of the $\gamma\text{-Fe}_2\text{O}_3\text{NC/PS-}b\text{-PMMA}$ nanocomposites

#### 6.3.2.1. Visual appearance

PS-*b*-PMMA block copolymer based nanocomposites were prepared by means of the incorporation of different contents of  $\gamma\text{-Fe}_2\text{O}_3$  nanocrystals into the PS-*b*-PMMA block copolymer. Nanocrystal content was varied in the range between 1 and 60 wt % in respect to the block copolymer content in the fabricated nanocomposites.

The visual appearance of the neat block copolymer solution as well as all investigated nanocomposite solutions is reported in **Figure 6.3**. The aspect of the nanocomposite solutions changed with the increase in the nanocrystal content, showing yellow color for low contents of nanocrystals and almost black color for high contents of nanocrystals. Remarkably even at high  $\gamma\text{-Fe}_2\text{O}_3$  nanocrystal content, nanocomposite solutions formed stable suspensions of  $\gamma\text{-Fe}_2\text{O}_3$  nanocrystals in PS-*b*-PMMA/toluene mixture.

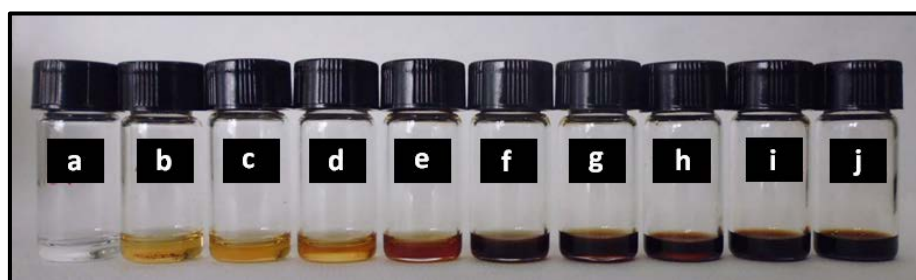


**Figure 6.3.** Visual appearance of the neat PS-*b*-PMMA block copolymer and  $\gamma\text{-Fe}_2\text{O}_3\text{NC/PS-}b\text{-PMMA}$  nanocomposite solutions containing 1, 3, 5, 10, 20, 30, 40, 50 and 60 wt %  $\gamma\text{-Fe}_2\text{O}_3$  nanocrystal contents.

### 6.3.2.2. Morphology

The morphology of the neat PS-*b*-PMMA block copolymer and  $\gamma$ -Fe<sub>2</sub>O<sub>3</sub>NC/PS-*b*-PMMA nanocomposites was studied by AFM and SEM. The AFM phase image corresponding to the neat block copolymer is presented in **Figure 6.4**.

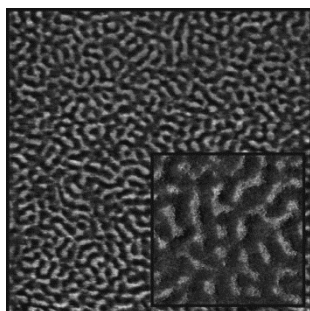


**Figure 6.4.** AFM phase image (2 μm x 2 μm and inset of 0.5 μm x 0.5 μm) of the neat PS-*b*-PMMA block copolymer.

The neat PS-*b*-PMMA block copolymer exhibits exactly the same morphology shown in Chapter 4, namely a cylindrical morphology, consisting of bright cylinders in a darker matrix, where cylinders can be found mostly in a parallel orientation in respect to the surface. The different contrasts in the phase image can be attributed to the difference in the mechanical and viscoelastic properties between blocks of the block copolymer [8]. Therefore, taking into account that a brighter color in the phase image corresponds to a higher modulus material, in this case the brighter phase corresponded to the PMMA phase whereas the darker matrix corresponded to the PS phase, which was already observed in Chapter 4 and is in good agreement with the literature [5,6,8].

Another point to consider is the Flory-Huggins interaction parameter between each block of the block copolymer and the solvent employed for the preparation of nanocomposites, which is toluene. As calculated in Chapter 4, the Flory-Huggins interaction parameters values between these two component pairs suggest a stronger interaction between toluene and PS phase (lower interaction parameter) than between toluene and PMMA phase (higher interaction parameter), which could also have an influence on the difference in the contrast between phases perceived in the phase image. In addition to this, the interaction between each block of the block copolymer and the silicon wafer used as substrate could also have an effect on the obtained morphology.

AFM phase images of  $\gamma\text{-Fe}_2\text{O}_3\text{NC}/\text{PS-}b\text{-PMMA}$  nanocomposites at increasing  $\gamma\text{-Fe}_2\text{O}_3$  nanocrystal content, varying from 1 to 60 wt %, are shown in **Figure 6.5**. It should be noted that the block copolymer retains its ability to self-assemble up to high nanocrystal content, even without any thermal or solvent vapor treatment applied to the prepared nanocomposites. The morphology of the investigated materials appeared well nanostructured up to 40 wt % nanocrystal content.

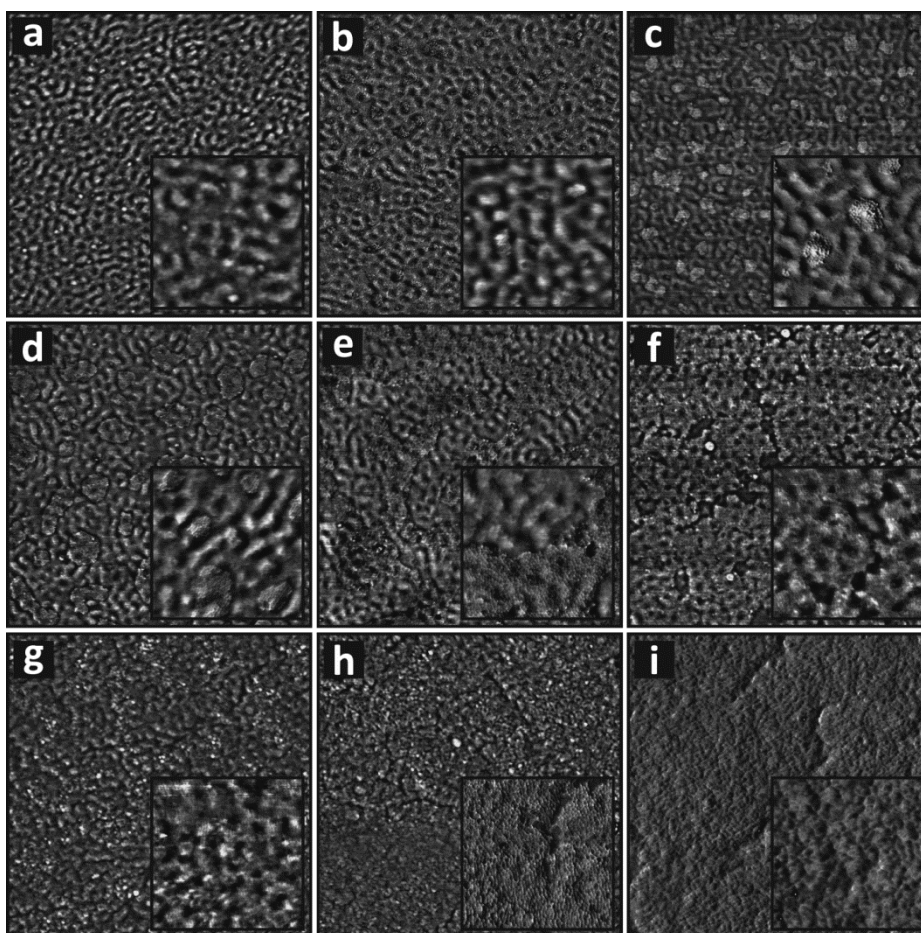


**Figure 6.5.** AFM phase images ( $2\ \mu\text{m} \times 2\ \mu\text{m}$  and inset of  $0.5\ \mu\text{m} \times 0.5\ \mu\text{m}$ ) of  $\gamma\text{-Fe}_2\text{O}_3\text{NC}/\text{PS-}b\text{-PMMA}$  nanocomposites containing 1 (a), 3 (b), 5 (c), 10 (d), 20 (e), 30 (f), 40 (g), 50 (h) and 60 (i) wt %  $\gamma\text{-Fe}_2\text{O}_3$  nanocrystal contents.

It can be observed that nanocomposites at low nanocrystal content presented the same morphology of the neat block copolymer, where PMMA phase appeared as bright cylinders while PS domain corresponded to the darker matrix. The 1 and 3 wt %  $\gamma\text{-Fe}_2\text{O}_3\text{NC}/\text{PS-}b\text{-PMMA}$  nanocomposites (**Figures 6.5a** and **6.5b**) showed identical structure of the neat block copolymer, apart from the presence of some nanocrystals clearly located in the darker microseparated phase of the  $\text{PS-}b\text{-PMMA}$  block copolymer, which

corresponds to the PS rich phase. The  $\gamma$ -Fe<sub>2</sub>O<sub>3</sub> nanocrystals appeared distributed or forming aggregates having a size that increases in function of the nanocrystal content.

The preferential location of  $\gamma$ -Fe<sub>2</sub>O<sub>3</sub> nanocrystals in the PS block rich phase can be explained considering that the synthetic route led to nanocrystals coated by organic surfactant, hence with a hydrophobic surface chemistry, as indicated by the FTIR spectroscopy, that made them specifically compatible with the less polar PS phase. The calculation of the Flory-Huggins interaction parameters between the oleic acid surfactant and each block of the block copolymer confirmed also a higher affinity between oleic acid and PS block, as was already reported in Chapter 4.

Thus, increasing  $\gamma$ -Fe<sub>2</sub>O<sub>3</sub> nanocrystal content in the nanocomposites to 5-10 wt %, they appeared more as aggregates than individually, being the size of these aggregates dependent on the nanocrystal content, although always preferentially situated in the PS block rich phase [6]. It is known that magnetic nanoparticles can cluster very effectively, much more than not magnetic counterparts, due to the strong magnetic interaction among nanoparticles [8,18-20]. In addition, in this case, cluster formation can be even more favored due to the specific geometry of the magnetic nanocrystals, which are able to hexagonally pack, as also observed by Crisan et al [21].

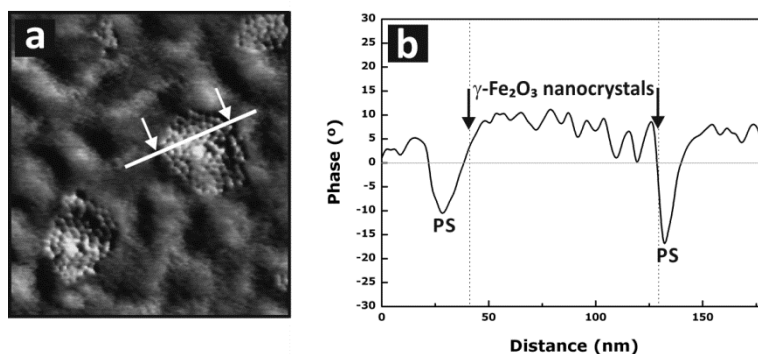


**Figure 6.6.** Detailed AFM phase image (400 nm x 400 nm) (a) of the  $\gamma$ -Fe<sub>2</sub>O<sub>3</sub> nanocrystal clusters present in the 5 wt %  $\gamma$ -Fe<sub>2</sub>O<sub>3</sub>NC/PS-*b*-PMMA nanocomposite. AFM phase profile (b) corresponds to the white line of the AFM phase image.

A clear image of such type of nanocrystal self-assembly can be found in the higher resolution AFM phase image of a single nanocrystal cluster in a 5 wt %  $\gamma$ -Fe<sub>2</sub>O<sub>3</sub>NC/PS-*b*-PMMA nanocomposite film shown in **Figure 6.6a**, along with its own AFM phase profile (**Figure 6.6b**), where the different nanocrystals that composed the cluster were identified by uniform peaks with high phase value in the profile graphic.

Here it is worth to mention that, in spite of the nanocrystal aggregation in clusters, the nanocomposites retained the morphology of the neat block copolymer.

As the nanocrystal content increased to 20, 30 and 40 wt % (Figures 6.5e, 6.5f and 6.5g), clusters became larger and larger, thus occupying a surface increasingly wider. Simultaneously, the initial nanostructure of the neat block copolymer was still visible not only in the cluster free regions, but also in the areas where nanocrystals clusters can be detected. At these high values of nanocrystal content, the brightest phase was mainly composed of PS block rich phase with  $\gamma\text{-Fe}_2\text{O}_3$  nanocrystals, being the PMMA also bright, whereas the darker phase was ascribed mainly to neat PS block. This description can be rationalized considering that  $\gamma\text{-Fe}_2\text{O}_3$  represent the hardest component and accordingly the PS block where they were located ended up even brighter than the PMMA block.

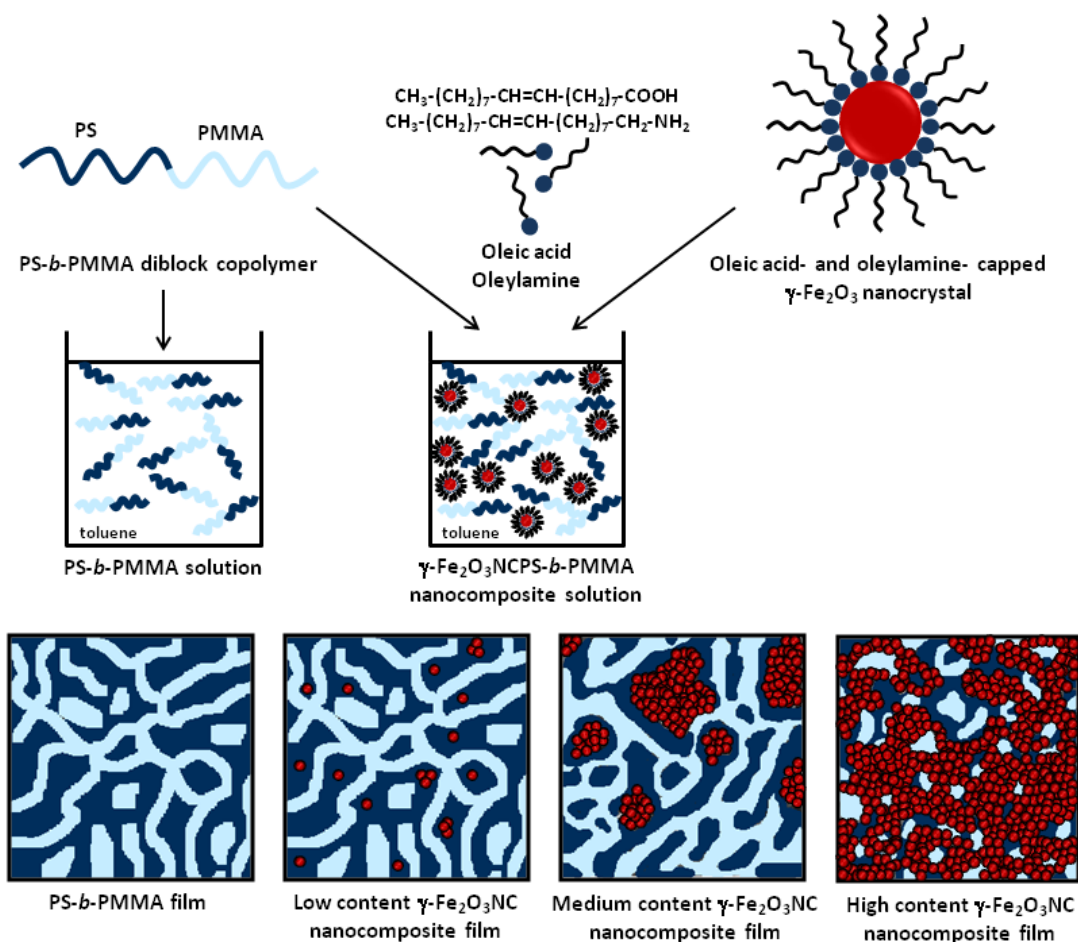


**Figure 6.7.** Schematic representation of the main components of the system, the neat PS-*b*-PMMA block copolymer and  $\gamma\text{-Fe}_2\text{O}_3$  nanocrystals, the neat block copolymer and nanocomposite solutions in toluene and the neat block copolymer and nanocomposite films with low, medium and high nanocrystal contents.

Finally, at the highest nanocrystal contents, 50 and 60 wt %  $\gamma$ -Fe<sub>2</sub>O<sub>3</sub> nanocrystals (**Figures 6.5h** and **6.5i**), almost the whole nanocomposite surface appeared covered by nanocrystal clusters, being the original nanostructure of the self-assembled block copolymer mostly hindered, apart from some small regions that still disclose the original block copolymer morphology, especially in the 50 wt %  $\gamma$ -Fe<sub>2</sub>O<sub>3</sub>NC/PS-*b*-PMMA nanocomposite. The microphase separation of block copolymer and nanocrystal cluster formation at increasing of  $\gamma$ -Fe<sub>2</sub>O<sub>3</sub> nanocrystal content has been schematically represented in **Figure 6.7**. This scheme shows how the main components of the investigated nanocomposites behave in toluene solution and in thin film, respectively, at increasing nanocrystal content, low, medium and high. The thickness of each film, as measured by profilometry, was found to be of around 22 nm both for the neat block copolymer and nanocomposites investigated thin films.

The morphology of the neat PS-*b*-PMMA block copolymer and  $\gamma$ -Fe<sub>2</sub>O<sub>3</sub>NC/PS-*b*-PMMA nanocomposites was also studied by SEM. SEM image of the neat PS-*b*-PMMA block copolymer is shown in the **Figure 6.8**. As in the case of AFM image, the phase separation between the two phases of the block copolymer was clearly distinguished, showing a morphology similar to the one observed by AFM, although in the case of SEM, the darker area corresponded to PMMA block, whereas the brighter area corresponded to the PS block [6,9,22]. In effect, in spite of the fact that PS and PMMA blocks have similar electron densities [23], the use of an in lens secondary electron detector allowed to record a contrast between PS and PMMA, arising from the surface topography of the block copolymer film. In both AFM and SEM images the PS phase is the larger domain.

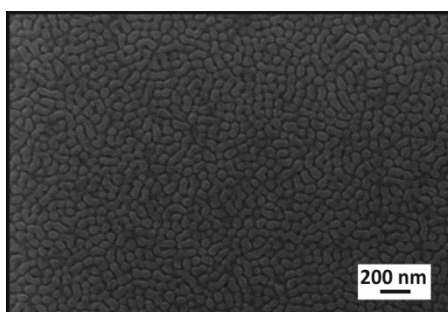


**Figure 6.8.** SEM image of the neat PS-*b*-PMMA block copolymer.

The difference detected in the ratio PS to PMMA domain size, which is higher in the SEM micrograph than in the AFM image, has been accounted to the lower surface

tension of PS ( $\gamma = 38$  mN/m) compared to that of PMMA ( $\gamma = 41$  mN/m) which results in a large SEM signal from the PS block at the film surface [24,25]. In the case of AFM, the diameter of the PMMA cylinders is in the range 25-35 nm, whereas in SEM this range is between 15-20 nm.

The  $\gamma$ -Fe<sub>2</sub>O<sub>3</sub>NC/PS-*b*-PMMA nanocomposites with amounts of  $\gamma$ -Fe<sub>2</sub>O<sub>3</sub> nanocrystals between 1 and 60 wt % were also investigated by SEM and the resulting images are shown in **Figure 6.9**. The structures presented in **Figure 6.9** are in good agreement with the nanostructures determined by AFM. In this case, the brighter objects corresponded to  $\gamma$ -Fe<sub>2</sub>O<sub>3</sub> nanocrystals and their clusters, while, among the other two gray domains, the brightest one corresponded to the PS block and the darkest to the PMMA block [6,9,22]. A detailed image of a  $\gamma$ -Fe<sub>2</sub>O<sub>3</sub> cluster formed at 5 wt % nanocrystal content is shown in **Figure 6.9c**.

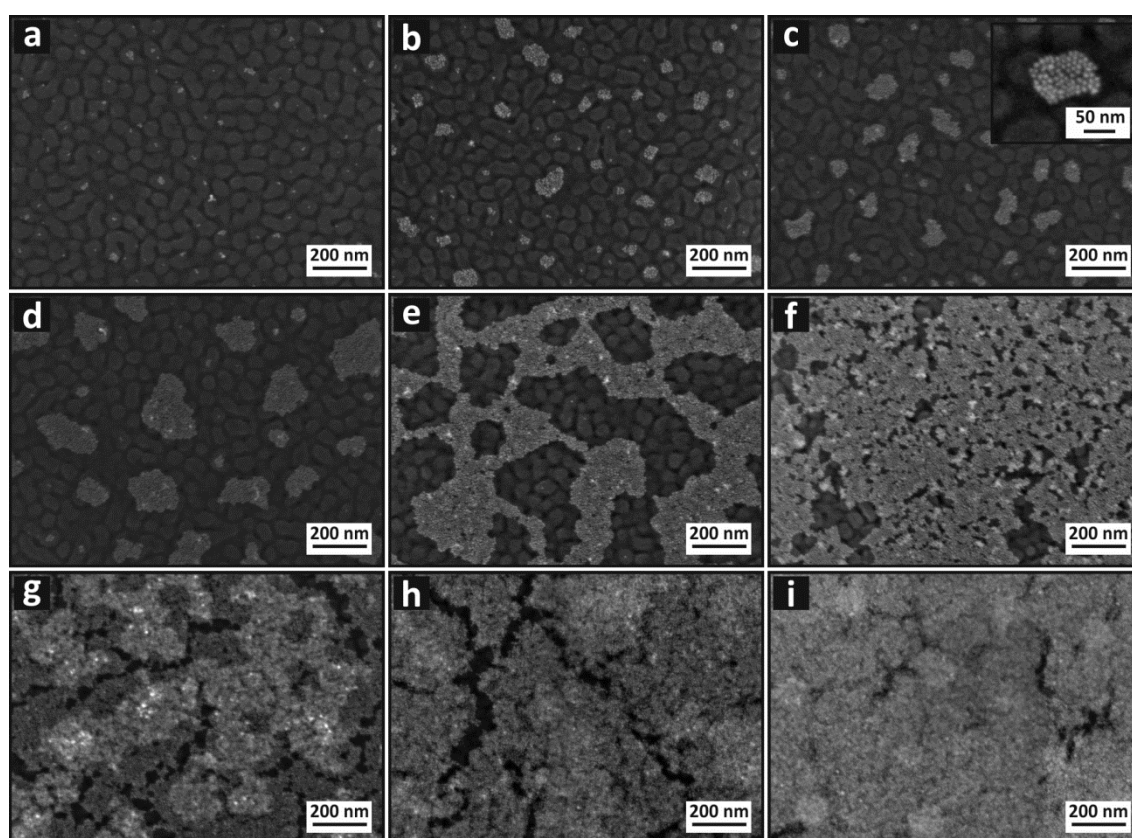


**Figure 6.9.** SEM images of  $\gamma$ -Fe<sub>2</sub>O<sub>3</sub>NC/PS-*b*-PMMA nanocomposites containing 1 (a), 3 (b), 5 (c), 10 (d), 20 (e), 30 (f), 40 (g), 50 (h) and 60 (i) wt %  $\gamma$ -Fe<sub>2</sub>O<sub>3</sub> nanocrystal contents. The inset in c shows a  $\gamma$ -Fe<sub>2</sub>O<sub>3</sub> nanocrystal cluster present in the 5 wt %  $\gamma$ -Fe<sub>2</sub>O<sub>3</sub>NC/PS-*b*-PMMA nanocomposite with higher magnification.

It can be clearly observed that, as confirmed also by AFM results,  $\gamma$ -Fe<sub>2</sub>O<sub>3</sub> nanocrystals were mainly located in the PS block rich phase of the block copolymer.

This fact is more evident in the nanocomposites containing low nanocrystal content, namely 1 and 3 wt %  $\gamma$ -Fe<sub>2</sub>O<sub>3</sub> (**Figures 6.9a** and **6.9b**), where the size of nanocrystal aggregates was smaller than PS block domains, and they were undoubtedly placed inside the PS block. However, at higher nanocrystal content, the location of nanocrystals in the nanostructured composite was not so evident anymore, as nanocrystals formed clusters larger than the PS block domain size. Moreover, the presence of nanocrystal clusters induced the selective enlargement of the PS block rich phase in respect to the PMMA block rich phase [6,9]. In nanocomposites at low nanocrystal content, while some isolated nanocrystals can be still detected dispersed in the host domain, the formation of small clusters can be also noticed. However, when the  $\gamma$ -Fe<sub>2</sub>O<sub>3</sub> nanocrystal content increased, they formed mostly clusters, having a size that increases as a function of the nanocrystal content, up to the almost extensive coverage of the film surface, as clearly visible in nanocomposites at 50-60 wt % nanocrystal contents (**Figures 6.9h** and **6.9i**).

The nanostructure of the block copolymer was evidently detected up to 10 wt %  $\gamma$ -Fe<sub>2</sub>O<sub>3</sub> content, while it can be still distinguished in some areas of the surfaces for the 20, 30 and 40 wt %  $\gamma$ -Fe<sub>2</sub>O<sub>3</sub>NC/PS-*b*-PMMA nanocomposites (**Figures 6.9e**, **6.9f** and **6.9g**), although nanocrystal clusters occupied most of the surface. In nanocomposites with the highest nanocrystal content, 50 and 60 wt %, the nanostructured area of the films considerably decreased.

### 6.3.2.3. Magnetic properties

In order to study the magnetic properties of the prepared nanocomposites, MFM technique was employed. As it is well known, iron oxide nanoparticles, and  $\gamma$ -Fe<sub>2</sub>O<sub>3</sub> maghemite nanocrystals in particular, possess magnetic properties that have been widely investigated [1,7,11,12].

Here it should be pointed out that the as-prepared nanocomposites, independent of the nanocrystal content, did not respond to the magnetic field by the magnetized MFM tip. This evidence could be explained by the fact that  $\gamma$ -Fe<sub>2</sub>O<sub>3</sub> nanocrystals are surrounded by organic components, given not only by the oleic acid and oleylamine acting as surfactants, but also by the PS block of the PS-*b*-PMMA block

copolymer, which can hinder the response to the applied magnetic field [26]. This effect in terms of magnetic response of the organic component was somehow expected, as an analogous behavior was observed when electrical properties of TiO<sub>2</sub>NR/PS-*b*-PMMA nanocomposites were investigated in Chapter 4. As it is well known and proved in Chapter 4, organic compounds, especially PS-*b*-PMMA block copolymer, could be partially degraded by exposure to UV light [27,28], and consequently such a treatment was carried out in order to possibly improve the detection of the magnetic response of the investigated nanocomposites.

Therefore, four films have been selected to be irradiated with UV light for 24 hours and then the magnetic properties of the nanocomposites were investigated by MFM. The AFM phase images of UV treated pristine  $\gamma$ -Fe<sub>2</sub>O<sub>3</sub> nanocrystals and 5, 30 and 60 wt %  $\gamma$ -Fe<sub>2</sub>O<sub>3</sub>NC/PS-*b*-PMMA nanocomposites as well as their MFM images are shown in **Figure 6.10**. Here it should be pointed out that the bright domains in the MFM images of investigated nanocomposites indicate the presence of domains which respond to the magnetic field applied by MFM tip [7,29]. Thus, it can be observed that the nanocomposite with the lowest nanocrystal content (**Figure 6.10b**) presented very weak response and few bright domains, whereas at higher nanocrystal content, the number and intensity of the bright domains was higher. In addition, the appearance of bright domains in the MFM images were clearly related to bright domains in the AFM images as is marked in **Figure 6.10**, thus confirming that the  $\gamma$ -Fe<sub>2</sub>O<sub>3</sub> nanocrystals, located in PS block rich phase, are responsible for the magnetic response in the investigated nanocomposites.

Regarding the pristine  $\gamma$ -Fe<sub>2</sub>O<sub>3</sub> nanocrystals and 30 and 60 wt %  $\gamma$ -Fe<sub>2</sub>O<sub>3</sub>NC/PS-*b*-PMMA nanocomposites, no considerable difference between the intensity of the magnetic response in investigated materials was detected. This evidence could be ascribed to the fact that MFM technique is only a qualitative method to detect domains which respond to the magnetic field applied by MFM tip. Consequently, the results clearly proved that the magnetic properties of the iron oxide nanocrystals are retained in the nanocomposites [7]. On the other hand, the digital pictures in the **Figures 6.10i, 6.10j, 6.10k and 6.10l** show the behavior of 5, 30 and 60 wt %  $\gamma$ -Fe<sub>2</sub>O<sub>3</sub>NC/PS-*b*-PMMA nanocomposite and pristine  $\gamma$ -Fe<sub>2</sub>O<sub>3</sub> nanocrystal solutions, respectively, upon exposure to a magnet. The picture

confirms the magnetic character of iron oxide nanocrystals and their ability to provide the nanocomposites based on PS-*b*-PMMA block copolymer with their magnetic properties. In this case, it should be noted that at the lowest iron oxide nanocrystal content, the nanocomposites do not exhibit any significant evidence of magnetization upon exposure to a magnet, whereas the effect of the magnet was evident for higher nanocrystal contents.

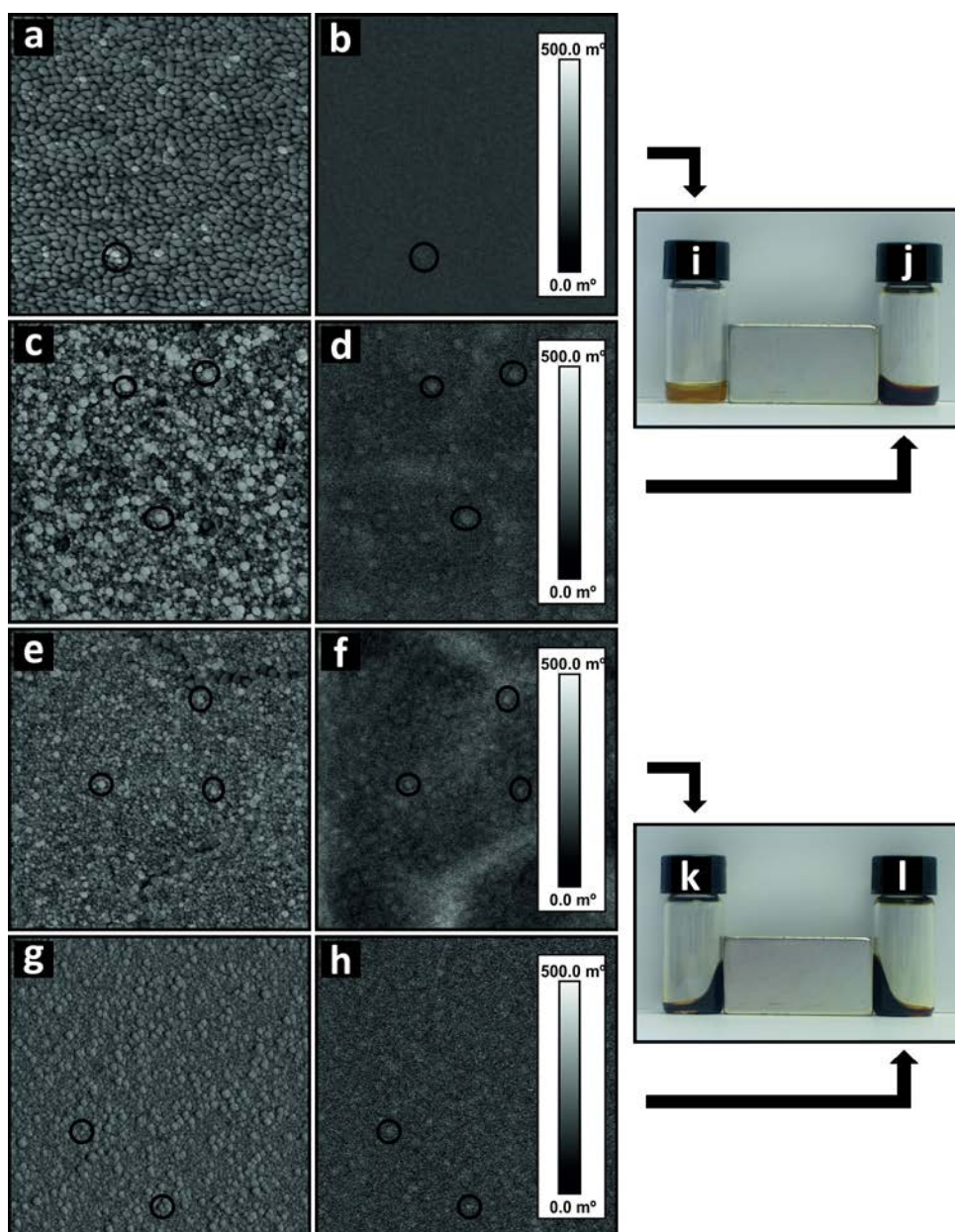


**Figure 6.10.** AFM phase (a, c, e and g) and MFM images (b, d, f and h) of 5, 30 and 60 wt %  $\gamma$ -Fe<sub>2</sub>O<sub>3</sub>NC/PS-*b*-PMMA nanocomposites and pristine  $\gamma$ -Fe<sub>2</sub>O<sub>3</sub> nanocrystals films, respectively, after being exposed to UV light for 24 hours (2  $\mu$ m x 2  $\mu$ m). Digital images of 5 (i), 30 (j) and 60 (k) wt %  $\gamma$ -Fe<sub>2</sub>O<sub>3</sub>NC/PS-*b*-PMMA nanocomposites and pristine  $\gamma$ -Fe<sub>2</sub>O<sub>3</sub> nanocrystals (l) solutions in presence of a magnet.

## 6.4. Conclusions

The incorporation of synthesized colloidal iron oxide maghemite nanocrystals into the self-assembled PS-*b*-PMMA block copolymer allowed to obtain nanocomposites with magnetic properties.

The synthesis procedure resulted in organic-capped  $\gamma$ -Fe<sub>2</sub>O<sub>3</sub> nanocrystals as confirmed by FTIR measurements. In the obtained nanocrystals, the surfactants, acting as coordinating agents, enabled the dispersibility of nanocrystals in a suitable medium. Such high dispersibility allowed to obtain high nanocrystal content in PS-*b*-PMMA block copolymer based nanocomposites (up to 60 wt %). The final morphologies of the nanocomposites, studied by AFM and SEM, were clearly dependent on the nanocrystal content. Thus, the nanostructured morphology of the self-assembled PS-*b*-PMMA block copolymer, obtained with absence of any treatment of as-prepared films, was found to be retained in the prepared nanocomposite films up to 40 wt % content, presenting a cylindrical morphology. Such main morphology was verified to coexist with  $\gamma$ -Fe<sub>2</sub>O<sub>3</sub> nanocrystals, which aggregated in clusters with the increase of the nanocrystal content.  $\gamma$ -Fe<sub>2</sub>O<sub>3</sub> nanocrystals were confirmed to be preferentially located in the PS block rich phase of the block copolymer, consistently with the high compatibility between the long alkyl chain surfactants, oleic acid and oleylamine, and such a domain in the copolymer.

While an evidence of the magnetic character of nanocomposites in solution at macroscale was successfully proven, the magnetic characterization of the nanocomposite films, carried out using MFM, demonstrated that the magnetic properties of the nanocomposite films can be significantly enhanced by a preliminary UV light treatment. Indeed,  $\gamma$ -Fe<sub>2</sub>O<sub>3</sub> nanocrystals located in PS rich phase in the treated films successfully responded to the magnetic field applied by the MFM tip, confirming that nanocrystals retained their magnetic property in the designed  $\gamma$ -Fe<sub>2</sub>O<sub>3</sub>NC/PS-*b*-PMMA nanocomposites. The achieved nanostructured nanocomposite materials are good candidate as functional components in potential applications ranging from magnetic sensors to magnetic information storage.

## 6.5. References

- [1] K. Woo, J. Hong, S. Choi, H. W. Lee, J. P. Ahn, C. S. Kim, S. W. Lee, *Chem. Mater.* 2004, **16**, 2814-2818.
- [2] L. H. Reddy, J. L. Arias, J. Nicolas, P. Couvreur, *Chem. Rev.* 2012, **12**, 5818-5878.
- [3] A. K. Gupta, M. Gupta, *Biomaterials* 2005, **26**, 3995-4021.
- [4] S. Sun, H. Zeng, *J. Am. Chem. Soc.* 2002, **124**, 8204-8205.
- [5] C. Xu, K. Ohno, V. Ladmiral, D. E. Milkie, J. M. Kikkawa, R. J. Composto, *Macromolecules* 2009, **42**, 1219-1228.
- [6] X. Xia, E. Metwalli, M. A. Ruderer, V. Körstgens, P. Busch, P. Böni, P. Müller-Buschbaum, *J. Phys.: Condens. Matter.* 2011, **23**, 254203/1-254203/9.
- [7] A. Horechyy, N. E. Zafeiropoulos, B. Nandan, P. Formanek, F. Simon, A. Kiriy, M. Stamm, *J. Mater. Chem.* 2010, **20**, 7734-7741.
- [8] P. Yang, S. Wang, X. Teng, W. Wei, V. P. Dravid, L. Huang, *J. Phys. Chem. C* 2012, **116**, 23036-23040.
- [9] M. M. A. Kashem, J. Perlich, A. Diethert, W. Wang, M. Memesa, J. S. Gutmann, E. Majkova, I. Capek, S. V. Roth, W. Petry, P. Müller-Buschbaum, *Macromolecules* 2009, **42**, 6202-6208.
- [10] Y. Yao, E. Metwalli, M. A. Niedermeier, M. Opel, C. Lin, J. Ning, J. Perlich, S. V. Roth, P. Müller-Buschbaum, *ACS Appl. Mater. Interfaces* 2014, **6**, 5244-5254.
- [11] R. Buonsanti, V. Grillo, E. Carlino, C. Giannini, M. L. Curri, C. Innocenti, C. Sangregorio, K. Achterhold, F. G. Parak, A. Agostiano, P. D. Cozzoli, *J. Am. Chem. Soc.* 2006, **128**, 16953-16970.
- [12] N. Depalo, P. Carrieri, R. Comparelli, M. Striccoli, A. Agostiano, L. Bertinetti, C. Innocenti, C. Sangregorio, M. L. Curri, *Langmuir* 2011, **27**, 6962-6970.
- [13] A. L. Willis, N. J. Turro, S. O'Brien, *Chem. Mater.* 2005, **17**, 5970-5975.
- [14] E. Fanizza, P. D. Cozzoli, M. L. Curri, M. Striccoli, E. Sardella, A. Agostiano, *Adv. Funct. Mater.* 2007, **17**, 201-211.
- [15] M. Bloemen, W. Brullot, T. T. Luong, N. Geukens, A. Gils, T. Verbiest, *J. Nanopart. Res.* 2012, **14**, 1100/1-1100/10.
- [16] F. J. Douglas, D. A. MacLaren, C. Renero-Lecuna, R. D. Peacock, R. Valiente, M. Murrie, *CrystEngComm* 2012, **14**, 7110-7114.

- [17] P. D. Cozzoli, E. Snoeck, M. A. Garcia, C. Giannini, A. Guagliardi, A. Cervellino, F. Gozzo, A. Hernando, K. Achterhold, N. Ciobanu, F. G. Parak, R. Cingolani, L. Manna, *Nano Lett.* 2006, **6**, 1966-1972.
- [18] J. F. Berret, N. Schonbeck, F. Gazeau, D. El Kharrat, O. Sandre, A. Vacher, M. Airiau, *J. Am. Chem. Soc.* 2006, **128**, 1755-1761.
- [19] M. J. Pavan, R. Shenhar, *J. Mater. Chem.* 2011, **21**, 2028-2040.
- [20] Z. Lu, Y. Yin, *Chem. Soc. Rev.* 2012, **41**, 6874-6887.
- [21] O. Crisan, K. Von Haeften, A. M. Ellis, C. Binns, *J. Nanopart. Res.* 2008, **10**, 193-199.
- [22] S. O. Kim, H. H. Solak, M. P. Stoykovich, N. J. Ferrier, J. J. de Pablo, P. F. Nealey, *Nature* 2003, **424**, 411-414.
- [23] C. H. Liu, L. K. Chiu, J. Y. Yeh, R. C. C. Tsiang, *J. Nanomater.* 2012, **2012**, 327583/1-327583/7.
- [24] D. Borah, T. Ghoshal, M. T. Shaw, A. Chaudhari, N. Petkov, A. P. Bell, J. D. Holmes, M. A. Morris, *Nanomater. Nanotechnol.* 2014, **4**, 1-13.
- [25] C. Harrison, M. Park, P. M. Chaikin, R. A. Register, D. H. Adamson, N. Yao, *Polymer* 1998, **39**, 2733-2744.
- [26] D. Kumar, H. Singh, S. Jouen, B. Hannyer, S. Banerjee, *RSC Adv.* 2015, **5**, 7138-7150.
- [27] D. A. Olson, L. Chen, M. A. Hillmyer, *Chem. Mater.* 2008, **20**, 869-890.
- [28] I. Vukovic, G. Brinke, K. Loos, *Polymer* 2013, **54**, 2591-2605.
- [29] I. García, A. Tercjak, N. E. Zafeiropoulos, M. Stamm, I. Mondragon, *Macromol. Rapid Comm.* 2007, **28**, 2361-2365.



**7**

**Epoxy based thermosetting system  
modified with polystyrene-*block*  
polymethyl methacrylate diblock  
copolymer**



## 7. Epoxy based thermosetting system modified with polystyrene-*block*-polymethyl methacrylate diblock copolymer

In this Chapter, the same PS-*b*-PMMA block copolymer as in the previous Chapters has been used, in this case in order to modify an epoxy based thermosetting system with the aim to improve its properties, in particular its mechanical properties. The neat thermosetting system is composed of a diglycidyl ether of bisphenol A (DGEBA) resin cured with the 4,4'-methylene-bis(3-chloro-2,6-diethylaniline) (MCDEA) curing agent. For the preparation of the thermosetting systems modified with the PS-*b*-PMMA block copolymer two different methods were used, without and with a solvent for the previous solution of the PS-*b*-PMMA block copolymer. The final obtained cured materials obtained were characterized in terms of their morphology, the thermal behavior and the mechanical properties at macroscale and nanoscale, investigating the influence of the modifier content as well as the preparation method on the final properties of the PS-*b*-PMMA/(DGEBA-MCDEA) cured systems.

### 7.1. Introduction

In recent years, many researchers have focused their work on the enhancement of the toughness of the epoxy resins [1,2]. One of the efficient ways to make the epoxy based thermosets tougher is to modify the original epoxy resin by the incorporation of a second phase into the continuous matrix of epoxy based thermoset through physical blending or chemical reactions. The addition of modifiers can convert the epoxy based thermoset into multiphase systems and in the case when the modifier is suitably dispersed through the matrix, the fracture toughness could be significantly increased.

Many kinds of modifiers have been employed for this purpose, although here the attention is focused on block copolymers as modifiers to produce nanostructured domains in thermoset materials [3-5]. The blocks of a block copolymer usually present different affinity towards a solvent, and also, they show a tendency to avoid the mixing of dissimilar blocks between each other. Consequently, they form well ordered structures such as spheres, worm-like micelles, vesicles and core-shell structures with domain sizes typically on the scale of nanometers and this makes block copolymers

excellent materials to create nanostructured thermosetting systems with improved toughness and without any considerable negative effect on the own properties of the epoxy resins.

PS-*b*-PMMA block copolymer has already been employed in the literature to nanostructure thermosetting systems. Some authors have already investigated the miscibility and phase behavior of PS-*b*-PMMA block copolymers with different epoxy systems [6-8] and also the effect of PS-*b*-PMMA content [7,9], PS-*b*-PMMA topological and sequential structures [10] and curing conditions [6] on the morphologies obtained when modifying an epoxy resin. Zucchi et al. also studied the mechanical properties of an epoxy based thermoset modified with PS-*b*-PMMA block copolymer, in terms of the elastic modulus and yield stress [11].

In this Chapter, PS-*b*-PMMA block copolymer has been investigated as a modifier of a DGEBA based epoxy matrix with the aim of obtaining nanostructured thermoset cured systems with improved mechanical properties. Two different ways of preparing the epoxy based thermosets modified with PS-*b*-PMMA block copolymer were analyzed and compared between each other, one by using a solvent for the solution of the block copolymer and the second by dissolving the block copolymer directly in the epoxy resin. The effect of the solvent as well as the effect of the PS-*b*-PMMA block copolymer content on the final properties of the materials has been investigated. The morphologies of all cured thermosetting systems obtained with varying the content of the PS-*b*-PMMA block copolymer from 5 to 50 wt % were analyzed by AFM. The glass transition temperatures were determined by DSC. The mechanical properties at macroscale were studied by the MTS in terms of the flexural behavior and fracture toughness measurements, about which no evidence was found in the literature. Additionally, QNM of the designed thermosetting systems at nanoscale were studied using the PeakForce mode of AFM.

## **7.2. Materials and methods**

### **7.2.1. Materials**

Diglycidyl ether of bisphenol A (DGEBA) (DER 330) epoxy resin (**Figure 7.1**), with an epoxy equivalent weight between 176-185 g/eq, was provided by Dow Chemical

Company. The curing agent used to cure this epoxy resin was 4,4'-methylene-bis(3-chloro-2,6-diethylaniline) (MCDEA) (**Figure 7.2**), supplied by Lonza.

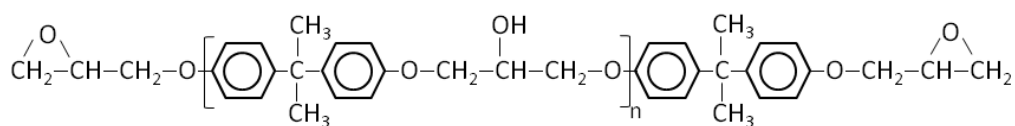


**Figure 7.1.** Chemical structure of the DGEBA epoxy resin.

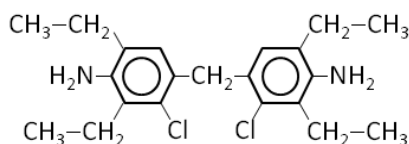


**Figure 7.2.** Chemical structure of the MCDEA curing agent.

PS-*b*-PMMA diblock copolymer, with a polydispersity index ( $M_w/M_n$ ) of 1.09 and number-average molecular weight of each PS and PMMA block of 80000 g/mol, was purchased from Polymer Source. Chloroform was purchased from Labscan and used as solvent.

### 7.2.2. PS-*b*-PMMA/(DGEBA-MCDEA) cured thermosetting system preparation

The DGEBA-MCDEA cured system was prepared by adding the stoichiometric amount of MCDEA to the DGEBA at 150 °C and by mixing manually for 5 minutes. PS-*b*-PMMA/(DGEBA-MCDEA) cured systems were prepared by two different methods. In the first method (from now denoted as non-solvent method), a certain amount of PS-*b*-PMMA block copolymer was dissolved in DGEBA resin, by manual mixing and by heating the blend at 150 °C, in order to ease the solution. When a complete homogenization was achieved, after some hours, a stoichiometric amount of MCDEA was added and manually stirred for 5 minutes.

In the second protocol (from now denoted as solvent method), the PS-*b*-PMMA block copolymer was first dissolved in chloroform at 10 mg/mL concentration at ambient temperature and then mixed with DGEBA resin. The mixture was heated at 150 °C until the evaporation of the solvent was reached. At this point, as in the non-solvent method, a stoichiometric amount of MCDEA was added and manually stirred for 5 minutes.

The neat DGEBA-MCDEA homogeneous mixture as well as PS-*b*-PMMA/(DGEBA-MCDEA) system homogeneous mixtures (prepared by both non-solvent and solvent

methods) obtained after the addition of the curing agent were poured into a glass mold and degassed at 150 °C under vacuum. All the thermosetting systems were cured at 190 °C for 6 h. Apart from the neat DGEBA-MCDEA cured system, four thermosetting systems were prepared with each of both protocols, with 5, 15, 25 and 50 wt % of PS-*b*-PMMA block copolymer. All the plates were 1.5 mm thick.

### 7.2.3. Characterization techniques

#### 7.2.3.1. Differential scanning calorimeter

DSC measurements were performed using a Mettler Toledo DSC 822<sup>e</sup> differential scanning calorimeter. Dynamic scans were performed from 20 to 200 °C with a heating rate of 5 °C/min. Prior to this scan, a heating from 20 to 200 °C followed by a cooling from 200 to 20 °C was carried out in order to delete the thermal history of the investigated materials. All experiments were conducted under a nitrogen flow of 10 mL/min using 10-15 mg samples in aluminum pans.

#### 7.2.3.2. Atomic force microscopy

AFM images were obtained under ambient conditions using a scanning probe microscope (Nanoscope IIIa Multimode™, Digital Instruments). Tapping mode (TM) was employed in air using an integrated tip/cantilever (125 μm in length with ca. 300 kHz resonant frequency). Typical scan rates during recording were 0.7-1 line/s using a scan head with a maximum range of 16 μm x 16 μm. Transverse cross section surface of each investigated thermosetting cured system was cut using an ultramicrotome Leica Ultracut R with a diamond blade.

#### 7.2.3.3. Materials testing system

Flexural tests were carried out using the MTS (model Insight 10) provided with a 250 N load cell and following the ASTM D790-10 standard test method, as detailed in Chapter 2. The support span was 22 mm, the crosshead rate 0.5 mm/min and specimen dimensions 27 mm x 6 mm x 1.5 mm (rectangular shape).

Fracture toughness tests were performed according to ASTM D5045-99 standard test method using the same MTS as for flexural tests, also as detailed in Chapter 2. The

support scan was 24 mm, the crosshead rate 10 mm/min and single edge notched specimens (SENB) with dimensions of 27 mm × 6 mm × 1.5 mm were used. Initially a sharp notch of around 2.7 mm was made by machining, and subsequently a natural crack was initiated using a razor blade.

For both flexural and fracture toughness tests more than five specimens for each system were tested. The 50 wt % PS-*b*-PMMA/(DGEBA-MCDEA) cured systems could not be analyzed in terms of its mechanical properties due to the difficulty in obtaining a continuous sheet after the curing.

#### 7.2.3.4. PeakForce quantitative nanomechanical mapping

PeakForce QNM modulus images were captured using Dimension Icon AFM microscope from Bruker. Measurements were carried out in PeakForce mode under ambient conditions. A silicon tip with nominal radius of 10 nm, cantilever length of 125 μm, and resonance frequency of 150 kHz was used. The measurements were performed with a calibrated optical sensitivity. The exact spring constant of the tip was calculated using the Thermal Tune option and a defined tip radius was adjusted using PS as standard.

### 7.3. Results and discussion

#### 7.3.1. Characterization of the neat DGEBA-MCDEA cured system and PS-*b*-PMMA/(DGEBA-MCDEA) cured systems

##### 7.3.1.1. Transparency

Different contents of the PS-*b*-PMMA block copolymer were incorporated into the DGEBA-MCDEA system by following two different procedures. Before curing, all the mixtures of the epoxy resin and the block copolymer were transparent and homogeneous, suggesting that there was no macrophase separation. It should be pointed out that in the case where no solvent was used, the DGEBA resin acted as the solvent for the block copolymer, being a good solvent for low contents of block copolymer, whereas for the highest contents the stirring had to be kept longer in time to reach a homogeneous solution.

After the curing, all investigated thermosetting cured systems continued to be transparent and homogeneous, except for the thermosetting systems containing

50 wt % content of PS-*b*-PMMA block copolymer. The visual appearance of the neat DGEBA-MCDEA cured system and of PS-*b*-PMMA/(DGEBA-MCDEA) cured systems up to 25 wt % content of the block copolymer is shown in **Figure 7.3**, where it is clearly seen that the transparency of the thermosetting cured systems only undergoes a slight decrease with the addition of PS-*b*-PMMA block copolymer, but in all cases they are still transparent.



**Figure 7.3.** Visual appearance of the neat DGEBA-MCDEA cured system (a) and 5 (b), 15 (d) and 25 (f) wt % PS-*b*-PMMA/(DGEBA-MCDEA) cured systems prepared by the non-solvent method and 5 (c), 15 (e) and 25 (g) wt % PS-*b*-PMMA/(DGEBA-MCDEA) cured systems prepared by the solvent method.

On the other hand, in the case of 50 wt % PS-*b*-PMMA/(DGEBA-MCDEA) cured systems, it was not possible to obtain a continuous sheet after the curing as the thermosetting systems prepared by both procedures had a high viscosity which prevented the formation of a continuous and homogeneous plate. However, it should be pointed out that the prepared non continuous sheets were also transparent, indicating the absence of macrophase separation.

In the cases of the cured systems with 15 wt % PS-*b*-PMMA (solvent method) and 25 wt % PS-*b*-PMMA (non-solvent method), it should be noted that, even if they are still transparent, a darker color is observed on them. This fact did not have any relation with the structure of the cured system, but with the superficial effect of the curing when the mould was not hermetically sealed.

#### 7.3.1.2. Miscibility and thermal behavior

The miscibility and thermal transitions of the neat DGEBA-MCDEA cured system and PS-*b*-PMMA/(DGEBA-MCDEA) cured systems were studied by DSC analysis. **Figure 7.4** shows the DSC thermograms of the second heating scan applied to each cured system. As can be seen, the neat DGEBA-MCDEA cured system presented one glass

transition temperature ( $T_g$ ) at 174 °C, whereas the neat block copolymer presented two  $T_g$ s, one at 105 °C corresponding to the PS block and the other one at 131 °C corresponding to the PMMA block.

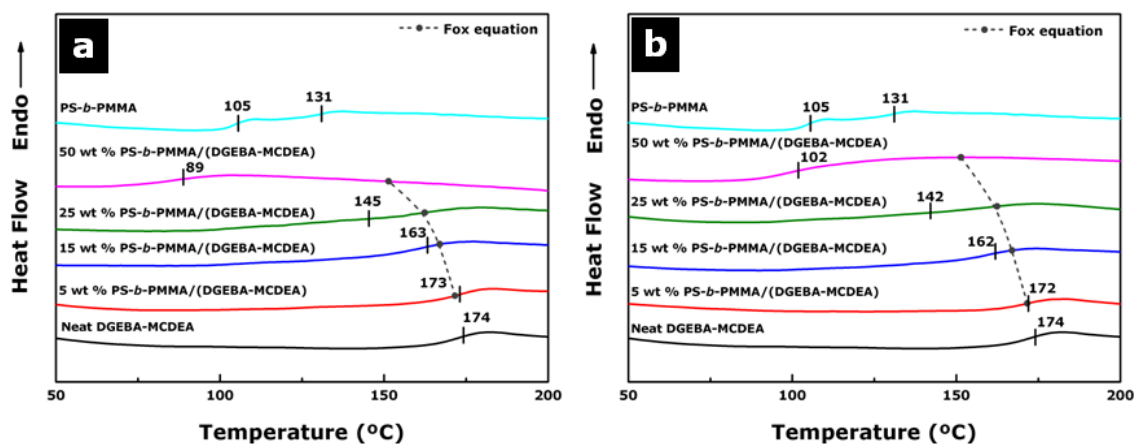


**Figure 7.4.** DSC thermograms of the neat DGEBA-MCDEA cured system, neat PS-*b*-PMMA block copolymer and 5, 15, 25 and 50 wt % PS-*b*-PMMA/(DGEBA-MCDEA) cured systems prepared by the non-solvent method (a) and by the solvent method (b). The dot line in each graph indicates the theoretical  $T_g$  values calculated by the Fox equation.

The DSC thermograms obtained for all the thermosetting cured systems prepared by the two employed methods presented only one  $T_g$ , which indicated that the block copolymer is partially miscible with the thermosetting system and consequently the cured systems exhibited one  $T_g$  located somewhere between the one of the neat DGEBA-MCDEA cured system and the one of the block copolymer. In addition, the miscibility of the components was also confirmed by the fact that the  $T_g$  of the PMMA block/(DGEBA-MCDEA) rich phase shifted to lower temperatures when the addition of the block copolymer increased, as is expected from a system based on a thermosetting system modified with a block copolymer [9].

Some authors have already reported that the miscibility of the PMMA block with the epoxy is higher than that of the PS block with the epoxy [7,8,10] and this suggests that PMMA will be mixed with the epoxy whereas the PS block could probably microseparate. Moreover, the Fox theoretical equation ( $\frac{1}{T_g} = \frac{x_1}{T_{g1}} + \frac{x_2}{T_{g2}}$ ) was used for the calculation of the theoretical  $T_g$  values of the PS-*b*-PMMA/(DGEBA-MCDEA) cured systems [12] and these values are also shown in **Figure 7.4**. First it should be pointed out that the employment of this equation is just an approximation, since it only

considers binary mixtures and for this calculation only PMMA block and neat DGEBA-MCDEA cured system were contemplated, since as it is mentioned above the PMMA block is the one that is partially miscible with the thermosetting system. The fact that the PS  $T_g$  was not taken into account for the estimation could lead to an error in the calculated values. Nevertheless, here it should be pointed out that the main goal of this calculation was just to compare the tendency of the  $T_g$  values with the theory, and in this case it was observed that as well as in the experimental results, the theoretical values tended also to decrease with the addition of the block copolymer. For low contents of the block copolymer the experimental values fitted well with the theoretical ones. However, for the highest contents like 50 wt %, the experimental values differed quite a lot from the theoretical ones, mainly due to the error in the application of the Fox equation commented above.

On the other hand, comparing the cured systems prepared by the two methods, it should be pointed out that there is no significant difference between the  $T_g$ s measured for both methods up to the 50 wt % content of block copolymer, being the measured values quite similar between both methods. In the case of 50 wt % PS-*b*-PMMA, however, the  $T_g$  of the non-solvent cured system was 13 °C lower than the  $T_g$  of the cured system prepared using the solvent, probably due to the fact that the solution of the cured system without solvent was not as homogeneous as the one using the solvent at such high PS-*b*-PMMA block copolymer contents.

### 7.3.1.3. Morphology

The neat DGEBA-MCDEA cured system as well as PS-*b*-PMMA/(DGEBA-MCDEA) cured systems were analyzed in terms of their morphology by means of AFM. The AFM phase image of the neat DGEBA-MCDEA cured system is shown in **Figure 7.5**. It can be clearly observed that the morphology is regular and uniform with no visible separation at micro and macroscale as is expected from the neat DGEBA-MCDEA cured system.

The morphologies of the PS-*b*-PMMA/(DGEBA-MCDEA) cured systems containing 5, 15, 25 and 50 wt % of block copolymer and prepared by following the two different procedures are presented in **Figure 7.6**. The four images on the left

correspond to the non-solvent method, whereas the images on the right correspond to the method that employs solvent for the mixing of block copolymer and DGEBA resin.

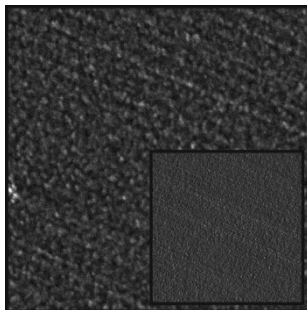


**Figure 7.5.** AFM phase image (1  $\mu\text{m}$  x 1  $\mu\text{m}$  and inset of 3  $\mu\text{m}$  x 3  $\mu\text{m}$ ) of the neat DGEBA-MCDEA cured system.

It can be seen that all analyzed thermosetting cured systems containing from 5 to 50 wt % PS-*b*-PMMA block copolymer content exhibited nanostructured morphologies. Before the curing reaction, it was observed that the PS-*b*-PMMA block copolymer was partially miscible with the DGEBA epoxy resin. As mentioned above, DGEBA resin has a higher miscibility with PMMA block than with PS block [7,8,10], as also was determined by the calculation of the Flory-Huggins interaction parameters of both pairs of compounds by means of the Hoftyzer and Van Krevelen method ( $\chi_{\text{PS-DGEBA}} = 0.42$  and  $\chi_{\text{PMMA-DGEBA}} = 0.39$ ) [13]. Therefore, during the curing reaction, PS block started to separate from the DGEBA-MCDEA matrix while PMMA block remained partially miscible with it. In this case, for PS-*b*-PMMA block copolymer contents up to 50 wt %, owing to the existence of the chemical bond between both PS and PMMA blocks of the block copolymer, the macrophase separation of the PS block did not take place, occurring in its stead only a microphase separation.

Looking at **Figure 7.6**, it should be first mentioned that all images presented some dark domains, of varying shape and size depending on the content of PS-*b*-PMMA block copolymer, separated from a clearer continuous phase, being the separated domains attributed to the PS block and the continuous matrix to the DGEBA-MCDEA cured phase partially miscible with the PMMA block [9]. The difference between the contrasts of the two phases is related to the difference in the viscoelastic character of them. Therefore, it can be claimed that the PMMA block/(DGEBA-MCDEA) rich phase is the one that presents the highest modulus.

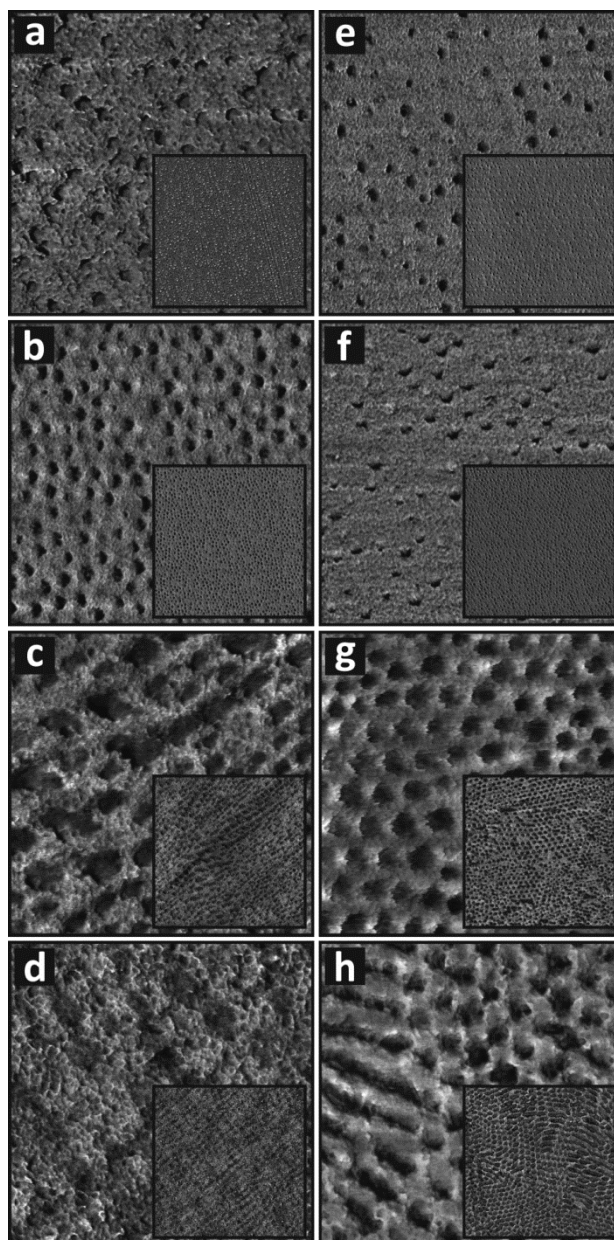


**Figure 7.6.** AFM phase images (1  $\mu\text{m}$  x 1  $\mu\text{m}$  and inset of 3  $\mu\text{m}$  x 3  $\mu\text{m}$ ) of 5 (a), 15 (b), 25 (c) and 50 (d) wt % PS-*b*-PMMA/(DGEBA-MCDEA) cured systems prepared by the non-solvent method and 5 (e), 15 (f), 25 (g) and 50 (h) wt % PS-*b*-PMMA/(DGEBA-MCDEA) cured systems prepared by the solvent method.

The morphology started to be spherical for the lowest contents of the block copolymer, namely for the 5 and 15 wt % PS-*b*-PMMA contents, being the number of domains slightly higher in the case of 15 wt % PS-*b*-PMMA content and also in the thermosetting cured systems prepared by the non-solvent method in comparison to the thermosetting cured systems prepared by the solvent method. Regarding the size of the nanodomains, the ones in the thermosetting cured systems prepared by the non-solvent method (30-40 nm for 5 wt % PS-*b*-PMMA and 35-45 nm for 15 wt % PS-*b*-PMMA) were also slightly larger than those prepared with solvent (20-35 nm for 5 wt

% PS-*b*-PMMA and 30-45 nm for 15 wt % PS-*b*-PMMA). These differences between the two preparation methods were somehow expected since the use of the solvent could have helped to achieve a better solution of the block copolymer and therefore a better miscibility between the block copolymer and the epoxy resin was reached, leading to less separated number of domains and smaller ones.

On the other hand, when the incorporated block copolymer amount increased to 25 and 50 wt %, the spherical morphology disappeared in the case where no solvent was used, showing a coexistence of bigger spheres and interconnected domains like cylinders for 25 wt % content and a less clearly nanostructured morphology for the 50 wt % content of PS-*b*-PMMA. The increase in the size of the domains was due to the higher content of block copolymer and consequently higher amount of PS block tending to separate from the matrix, taking with it some part of the PMMA block present in the matrix, but always without reaching a macrophase separation as was confirmed by the transparency of the systems with 50 wt % block copolymer content (not shown here) and by the DSC results.

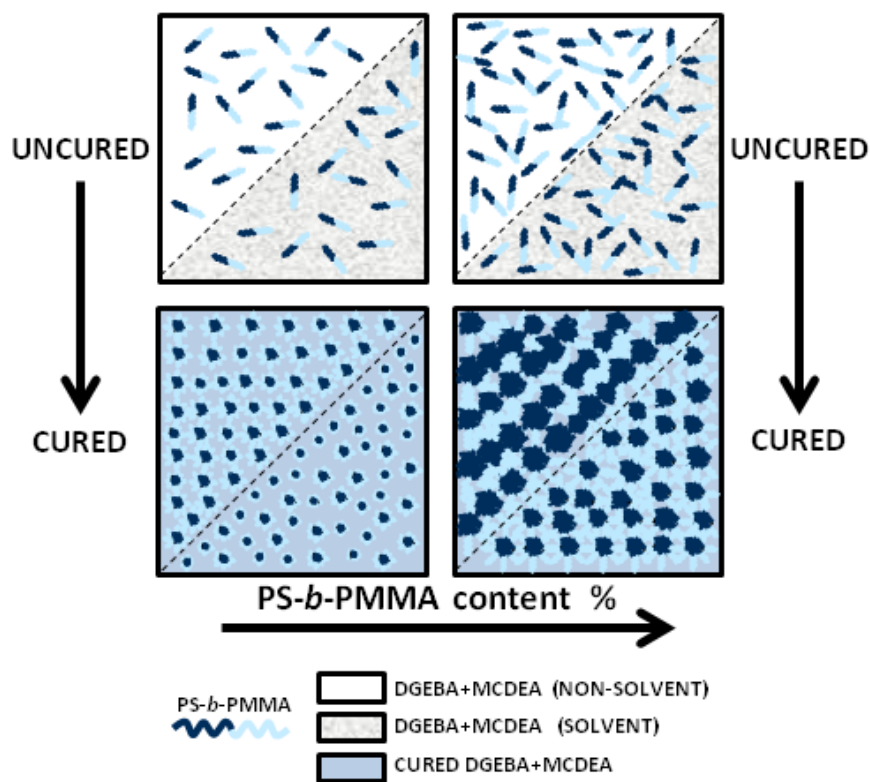


**Figure 7.7.** Schematic representation of the morphologies obtained for thermosetting systems modified with low and high PS-*b*-PMMA block copolymer contents.

However, the employment of solvent in the preparation of the thermosetting systems led to a still uniform and spherical structure for high contents of block copolymer like 25 wt % (with bigger spheres of 55-75 nm) and almost spherical with some interconnected domains like cylinders for 50 wt % contents. Consequently, it should be pointed out that the use of the solvent maintained the regular nanostructured morphology up to higher contents of the block copolymer in comparison with the non-solvent method. The morphologies obtained by the addition of the PS-*b*-PMMA block copolymer to the thermosetting matrix by both employed methods have been schematically represented in **Figure 7.7**.

#### 7.3.1.4. Mechanical properties

The mechanical properties at macroscale of all thermosetting cured systems, except for the 50 wt % PS-*b*-PMMA/(DGEBA-MCDEA) cured systems, were studied in terms of the flexural modulus ( $E$ ), the critical stress intensity factor ( $K_{IC}$ ) and the critical strain energy release rate ( $G_{IC}$ ). The flexural moduli of the neat DGEBA-MCDEA cured system and of the DGEBA-MCDEA cured systems modified with different contents of PS-*b*-PMMA block copolymer are presented in **Figure 7.8**.

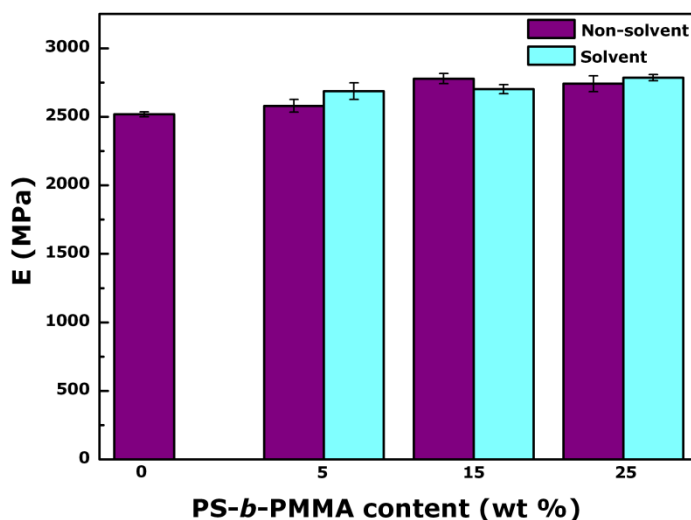


**Figure 7.8.** Flexural modulus ( $E$ ) of the neat DGEBA-MCDEA cured system and 5, 15 and 25 wt % PS-*b*-PMMA/(DGEBA-MCDEA) cured systems prepared by the non-solvent and the solvent method.

It is observed that the neat DGEBA-MCDEA cured system presented a flexural modulus of 2500 MPa which is in accordance with the values reported in the literature

for this system [14,15]. Moreover, the flexural modulus value increased when the thermosetting system was modified with the PS-*b*-PMMA block copolymer. In the case of the method without solvent, the highest value of the modulus was obtained for the 15 wt % PS-*b*-PMMA content, whereas in the case of the method using solvent, the 25 wt % PS-*b*-PMMA/(DGEBA-MCDEA) cured system was the one that reached the highest value of flexural modulus. Taking into account the AFM phase images of these two cured systems (**Figure 7.6**), it could be claimed that both systems were the ones that presented the most regular spherical morphology among all the studied systems, reaching a quasi hexagonal morphology.

In any case, it should be also taken into account that the differences among the moduli obtained by the two employed methods and with the different concentrations of the block copolymer are not so relevant if the error bars are taken into account. However, the general tendency is that the higher the amount of block copolymer, the higher the modulus of the investigated system. In general, the opposite effect has been observed in the literature, since it is well-known that the addition of a block copolymer in contents higher than 10 wt % tends to plasticize the thermoset matrix leading to a lower flexural modulus [12,14,16,17]. In this case, an improvement in the flexural modulus occurred at least up to 25 wt % PS-*b*-PMMA content, probably due to the fact that even if the addition of the PS-*b*-PMMA block copolymer reduced the cross-linking density of the epoxy network, the modifier employed in this case did not have a modulus much lower than the neat DGEBA-MCDEA cured system [11] and it had a positive contribution in the flexural behavior of the epoxy.

In addition, the increase in the flexural modulus could be also related to a decrease in the free volume provoked by the incorporation of the block copolymer [12]. Therefore, these results confirm the miscibility between PMMA block and the epoxy resin, which is high enough to reach such increase in the flexural behavior of the epoxy matrix.

Regarding the toughness of these analyzed systems, the values of  $K_{IC}$  and  $G_{IC}$  were calculated and are shown in **Figure 7.9**, respectively. The toughness in terms of  $K_{IC}$  (**Figure 7.9a**) was maintained in respect to the neat DGEBA-MCDEA cured system with the addition of 5 wt % PS-*b*-PMMA content to the thermoset matrix. However, with higher incorporated amounts of PS-*b*-PMMA block copolymer, with both 15 and 25 wt % contents, the  $K_{IC}$  values increased considerably in respect to the toughness of

the neat DGEBA-MCDEA cured system. In this case, no appreciable difference was observed between the non-solvent and the solvent methods.

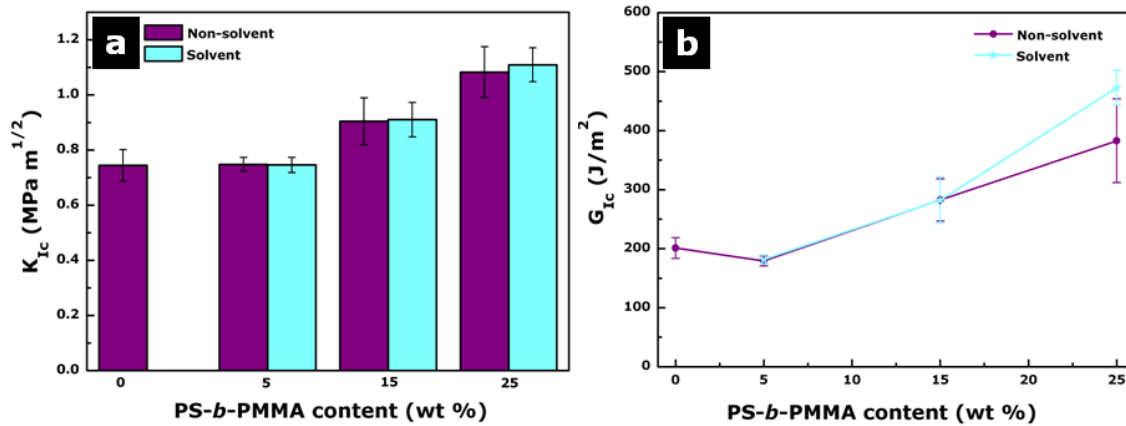


**Figure 7.9.** Critical stress intensity factor ( $K_{IC}$ ) (a) and critical strain energy release rate ( $G_{IC}$ ) (b) of the neat DGEBA-MCDEA cured system and 5, 15 and 25 wt % PS-*b*-PMMA/(DGEBA-MCDEA) cured systems prepared by the non-solvent and the solvent method.

The toughness of the cured systems not only increased with the addition of the block copolymer, but also it increased more as the content of the block copolymer was higher. This confirms that the modification of the thermosetting system with the PS-*b*-PMMA block copolymer was worthy from the point of view of an enhancement in the mechanical properties of the epoxy resin, both flexural and toughness behavior, but especially of the toughness, as the low toughness is one of the known drawbacks of epoxy matrices. Unmodified thermosetting cured systems are usually single-phase materials, meanwhile the addition of modifiers can turn them into multiphase systems, which is the case of the PS-*b*-PMMA block copolymer modifier. As reported by many authors, when the modifier domains are correctly dispersed throughout the epoxy matrix, the fracture toughness can be greatly improved [1,12,16,18].

Consequently, it is also quite known the existence of an important relation between the morphology at nanoscale and the fracture toughness [3,12,17]. In this case, the bigger spherical domains observed in the 25 wt % PS-*b*-PMMA content, which coexisted with some cylinders in the case of the non-solvent method, resulted in the highest toughness values.

In addition, as can be seen in **Figure 7.9b**, the critical strain energy release rate ( $G_{IC}$ ) showed a similar tendency in comparison to the  $K_{IC}$  values, where the  $G_{IC}$

maintained the value of the neat DGEBA-MCDEA cured system for the 5 wt % content of the block copolymer and also increased considerably for 15 and 25 wt % PS-*b*-PMMA block copolymer contents.

Quantitative nanomechanical properties (QNM) of cured thermosetting systems prepared without and with solvent were investigated using AFM in PeakForce mode. The elastic modulus PeakForce QNM images of the neat DGEBA-MCDEA cured system and of investigated cured thermosetting systems modified with PS-*b*-PMMA block copolymer are showed in **Figure 7.10** and **Figure 7.11**, respectively.

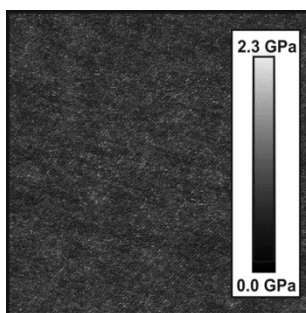


**Figure 7.10.** Elastic modulus PeakForce QNM image (1  $\mu\text{m}$  x 1  $\mu\text{m}$ ) of the neat DGEBA-MCDEA cured system.

The elastic modulus of the neat DGEBA-MCDEA cured system (**Figure 7.10**) had almost the same value in every measured point in the modulus PeakForce QNM image, being this value around 2.3 GPa. The modulus PeakForce QNM images of all cured thermosetting systems modified with PS-*b*-PMMA block copolymer without and with solvent revealed two different areas with different elastic modulus values. The highest elastic modulus corresponded to the PMMA block/(DGEBA-MCDEA) rich phase (brighter areas) and the lowest one to the microphase separated PS block domains (darker areas).

For the PS-*b*-PMMA/(DGEBA-MCDEA) cured systems prepared without solvent, the elastic modulus corresponding to PMMA block/(DGEBA-MCDEA) rich phase (around 2.5 GPa) was slightly higher than the elastic modulus of the neat DGEBA-MCDEA cured system, indicating that the PMMA block contributed positively to the elastic modulus of the PMMA block/(DGEBA-MCDEA) matrix. Simultaneously, the modulus PeakForce QNM images allowed to detect also the elastic modulus values of the microseparated PS block phase, which were much lower than the elastic modulus values of the PMMA block/(DGEBA-MCDEA) matrix for each PS-*b*-PMMA content

system. In addition, the elastic modulus values of the microseparated PS block phase did not undergo any significant variation among the different investigated thermosetting systems. In fact, its values varied between 1.2 and 1.4 GPa, confirming that the microseparated PS block had approximately two times lower modulus than the PMMA block/(DGEBA-MCDEA) rich phase.

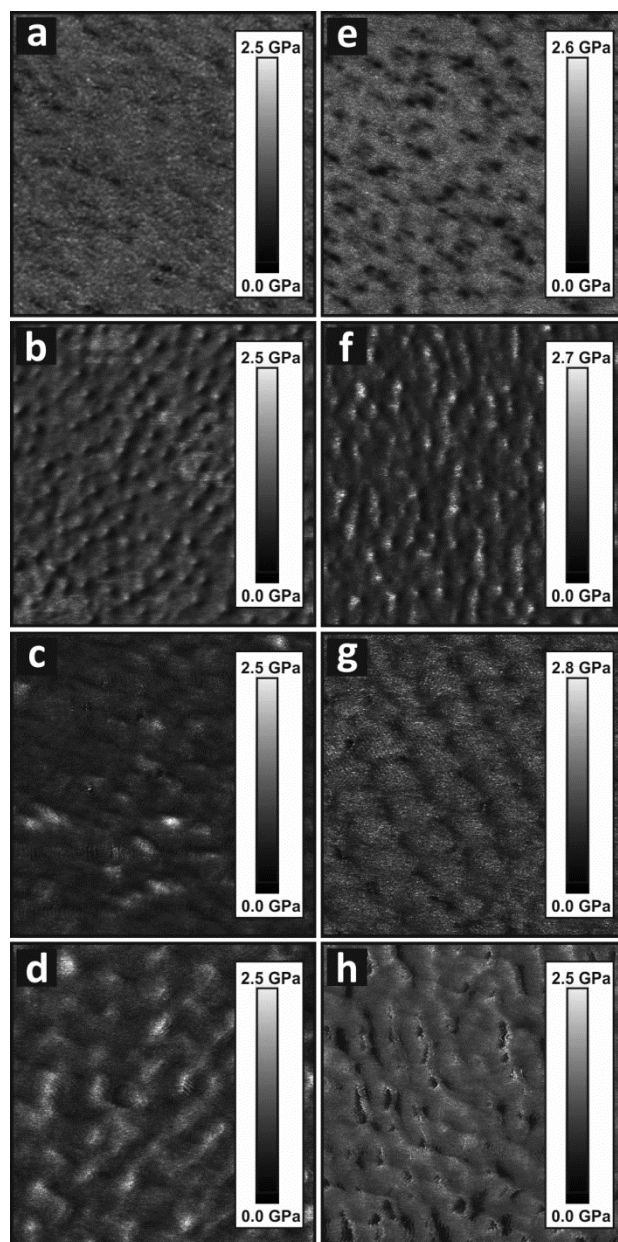


**Figure 7.11.** Elastic modulus PeakForce QNM images ( $1\ \mu\text{m} \times 1\ \mu\text{m}$ ) of 5 (a), 15 (b), 25 (c) and 50 (d) wt % PS-*b*-PMMA/(DGEBA-MCDEA) cured systems prepared by the non-solvent method and 5 (e), 15 (f), 25 (g) and 50 (h) wt % PS-*b*-PMMA/(DGEBA-MCDEA) cured systems prepared by the solvent method.

Here it should be highlighted that the elastic modulus of the PMMA block/(DGEBA-MCDEA) matrix is also higher than the elastic modulus of the neat

DGEBA-MCDEA cured system, confirming that the PMMA block is partially miscible with the thermosetting system, and that it had a strong effect on the increase of the elastic modulus at the macroscopic scale on the contrary to the microphase separated PS block domains, which resulted in lower local elastic modulus.

The elastic modulus of the PMMA block/(DGEBA-MCDEA) rich phase of the thermosetting systems modified with PS-*b*-PMMA block copolymer prepared with solvent method increased considerably with the increase of the PS-*b*-PMMA block copolymer content, being around 2.6 GPa, 2.7 GPa and 2.8 GPa for 5, 15 and 25 wt % PS-*b*-PMMA/(DGEBA-MCDEA) cured systems, respectively. However, the elastic modulus of the PMMA block/(DGEBA-MCDEA) rich phase of the 50 wt % PS-*b*-PMMA block/(DGEBA-MCDEA) cured system was lower than that of 25 wt % PS-*b*-PMMA block/(DGEBA-MCDEA) cured system, although still higher than the neat DGEBA-MCDEA cured system.

If the elastic modulus of the PMMA block/(DGEBA-MCDEA) rich phase of the cured thermosetting systems prepared by the non-solvent and the solvent method are compared among them, one can conclude that the use of the solvent for the preparation leads to higher elastic modulus of the PMMA block/(DGEBA-MCDEA) rich phase probably due to a higher miscibility between the PMMA block and the thermosetting system in these systems.

On the other hand, the elastic modulus values of PS block rich phase in cured thermosetting systems prepared with solvent varied from 1.5 GPa to 1.7 GPa, being slightly higher than the elastic modulus values of the PS block rich phases corresponding to thermosetting systems prepared without solvent. The elastic modulus of the PS block rich phase in 50 wt % PS-*b*-PMMA/(DGEBA-MCDEA) cured system with solvent decreased to 1 GPa.

#### **7.4. Conclusions**

PS-*b*-PMMA block copolymer has been effectively employed as a modifier of an epoxy based thermosetting system, leading to cured systems with clearly improved final properties. Two different methods were followed to incorporate different contents of PS-*b*-PMMA block copolymer into the DGEBA-MCDEA thermoset matrix. The visual

transparency of the prepared sheets indicated the absence of macrophase separation in all PS-*b*-PMMA/(DGEBA-MCDEA) cured systems for both preparation methods.

On the other hand, AFM results showed a clear microphase separation in all investigated cured thermosetting systems modified with PS-*b*-PMMA block copolymer, obtaining morphologies dependent on both block copolymer content and preparation method. In general, PS block microphase separated domains increased in size and quantity with higher contents of PS-*b*-PMMA block copolymer, changing from spherical domains to almost cylindrical interconnected ones. The miscibility between PMMA block and the DGEBA-MCDEA cured system was proved by DSC, where it was observed that the addition of the block copolymer to the matrix provoked a decrease in the  $T_g$  of the thermoset matrix.

The mechanical properties of the neat DGEBA-MCDEA cured system and PS-*b*-PMMA/(DGEBA-MCDEA) cured systems, investigated at macroscale and nanoscale, demonstrated that the addition of PS-*b*-PMMA block copolymer was able to enhance the mechanical properties of the investigated thermosetting system. The flexural modulus and the fracture toughness measured by MTS increased with the addition of the PS-*b*-PMMA block copolymer up to 25 wt % PS-*b*-PMMA content, being the enhancement of the fracture toughness higher than that of the flexural modulus.

The quantitative nanomechanical properties, studied by PeakForce QNM, showed an improvement in the elastic modulus of the thermosetting system, and in particular of the PMMA block/(DGEBA-MCDEA) rich phase, when the PS-*b*-PMMA block copolymer was incorporated into the epoxy based matrix up to 25 wt % PS-*b*-PMMA content. The PS-*b*-PMMA/(DGEBA-MCDEA) cured systems prepared by solvent method led to slightly higher values of fracture toughness and elastic modulus, due to a higher miscibility reached in these systems.

## 7.5. References

- [1] L. Ruiz-Pérez, G. J. Royston, J. P. A. Fairclough, A. J. Ryan, *Polymer* 2008, **49**, 4475-4488.
- [2] N. Domun, H. Hadavinia, T. Zhang, T. Sainsbury, G. H. Liaghat, S. Vahid, *Nanoscale* 2015, **7**, 10294-10329.

- [3] J. M. Dean, P. M. Lipic, R. B. Grubbs, R. F. Cook, F. S. Bates, *J. Polym. Sci. Pol. Phys.* 2001, **39**, 2996-3010.
- [4] P. Sun, Q. Dang, B. Li, T. Chen, Y. Wang, H. Lin, Q. Jin, D. Ding, *Macromolecules* 2005, **38**, 5654-5667.
- [5] N. Hameed, Q. Guo, Z. Xu, T. L. Hanley, Y. W. Mai, *Soft Matter* 2010, **6**, 6119-6129.
- [6] H. E. Romeo, I. A. Zucchi, M. Rico, C. E. Hoppe, R. J. J. Williams, *Macromolecules* 2013, **46**, 4854-4861.
- [7] E. Girard-Reydet, A. Sévignon, J. P. Pascault, C. E. Hoppe, M. J. Galante, P. A. Oyanguren, R. J. J. Williams, *Macromol. Chem. Phys.* 2002, **203**, 947-952.
- [8] T. Fine, F. Lortie, L. David, J. P. Pascault, *Polymer* 2005, **46**, 6605-6613.
- [9] M. Blanco, M. López, G. Kortaberria, I. Mondragon, *Polym. Int.* 2010, **59**, 523-528.
- [10] W. Fan, S. Zheng, *Polymer* 2008, **49**, 3157-3167.
- [11] I. A. Zucchi, M. J. Galante, R. J. J. Williams, *Polymer* 2005, **46**, 2603-2609.
- [12] M. Larrañaga, E. Serrano, M. D. Martin, A. Tercjak, G. Kortaberria, K. de la Caba, C. Riccardi, I. Mondragon, *Polym. Int.* 2007, **56**, 1392-1403.
- [13] D. W. Van Krevelen, *Properties of Polymers*, Elsevier Science B. V., Amsterdam (The Netherlands), 1990.
- [14] C. Ocando, A. Tercjak, I. Mondragon, *Compos. Sci. Technol.* 2010, **70**, 1106-1112.
- [15] M. I. Giannotti, C. R. Bernal, P. A. Oyanguren, M. J. Galante, *Polym. Eng. Sci.* 2005, **45**, 1312-1318.
- [16] C. Ocando, A. Tercjak, M. D. Martin, J. A. Ramos, M. Campo, I. Mondragon, *Macromolecules* 2009, **42**, 6215-6224.
- [17] D. H. Builes, H. Hernandez, I. Mondragon, A. Tercjak, *J. Phys. Chem. C* 2013, **117**, 3563-3571.
- [18] E. Serrano, A. Tercjak, C. Ocando, M. Larrañaga, M. D. Parellada, S. Corona-Galván, D. Mecerreyes, N. E. Zafeiropoulos, M. Stamm, I. Mondragon, *Macromol. Chem. Physic.* 2007, **208**, 2281-2292.



**8**

**Epoxy based thermosetting  
system modified with polyethylene  
oxide-*block*-polypropylene oxide-*block*-  
polyethylene oxide triblock copolymer**



## 8. Epoxy based thermosetting system modified with polyethylene oxide-*block*-polypropylene oxide-*block*-polyethylene oxide triblock copolymer

In this Chapter, the same DGEBA based epoxy resin as in Chapter 7 has been used to develop thermosetting systems cured with *m*-xylylenediamine (MXDA) and modified with polyethylene oxide-*block*-polypropylene oxide-*block*-polyethylene oxide (PEO-*b*-PPO-*b*-PEO). As in Chapter 7, the main objective of this Chapter is to modify the DGEBA based epoxy system in order to improve its properties, focusing mainly on its mechanical properties. The curing process, carried out at room temperature, led to thermosetting systems with varying modifier contents, and the effect of the addition of the PEO-*b*-PPO-*b*-PEO block copolymer was analyzed from the point of view of the morphology, the thermal behavior and mechanical properties.

### 8.1. Introduction

As confirmed in Chapter 7, the modification of epoxy thermosetting systems with block copolymers results to be an adequate method to improve epoxy toughness, which is one of the main drawbacks of epoxy thermosets [1-5]. In addition to this, block copolymers can also create ordered microphase-separated structures when they are incorporated into a thermosetting matrix.

The block copolymer PEO-*b*-PPO-*b*-PEO has been used before to modify phenolic [6], unsaturated polyester [7-9] and epoxy resins [10-17]. Already published studies related to the blend of DGEBA epoxy resin with PEO-*b*-PPO-*b*-PEO block copolymer revealed that different macroseparated or microseparated morphologies were obtained depending on the content of block copolymer in the matrix, molar ratio between blocks, molecular weight of the block copolymer and the curing cycle carried out. The miscibility of the blends and kinetics of the curing reaction were also investigated as a function of the block copolymer content. The control of nanostructures by optimizing the curing conditions resulted to be essential to control the mechanical properties of the final materials.

In this Chapter, PEO-*b*-PPO-*b*-PEO block copolymer has been employed as modifier of a DGEBA based epoxy matrix with the aim to obtain nanostructured thermoset systems with improved mechanical properties. It was demonstrated that PEO-*b*-PPO-*b*-PEO block copolymer resulted to be an effective modifier to lead to a remarkable improvement on the toughness value of an epoxy system, which was the main interest. Different contents of the block copolymer up to 50 wt % were added to the matrix in order to study the influence of the content of block copolymer on the morphology, mechanical properties and curing reaction time of the epoxy system.

The curing process was the same for all investigated systems and it was chosen taking into account the lower critical solution temperature (LCST) behavior of PEO-*b*-PPO-*b*-PEO block copolymer [13,18]. Consequently, all investigated thermosetting system curing processes were carried out at 25 °C, which is a big advantage from an industrial point of view since the low temperature allows to reach nanostructuring of the PEO-*b*-PPO-*b*-PEO/(DGEBA-MXDA) cured system with a very high PEO-*b*-PPO-*b*-PEO content and improve drastically the toughness of investigated thermosetting systems.

The morphology of the PEO-*b*-PPO-*b*-PEO/(DGEBA-MXDA) cured systems and the size of the microseparated phase were investigated by AFM and TEM. Thermal behavior of the PEO-*b*-PPO-*b*-PEO/(DGEBA-MXDA) cured systems in respect to the neat DGEBA-MXDA system was studied by DSC. The mechanical properties measurements at macroscale were carried out by the MTS and QNM at nanoscale were studied using the PeakForce mode of AFM. The optical transparency was investigated by UV-vis spectroscopy. Contact angle measurement was employed to characterize the surface properties of investigated cured thermosetting systems.

## **8.2. Materials and methods**

### **8.2.1. Materials**

The epoxy resin used in this Chapter was the same as in the previous Chapter, DGEBA resin (DER 330) provided by The Dow Chemical Company with an epoxy equivalent weight between 176-185 g/eq. The curing agent used to cure this epoxy

resin was m-xylylenediamine (MXDA) (**Figure 8.1**) supplied by Sigma-Aldrich. The employment of this curing agent allows to reach the curing at low curing temperature for the fabrication of the investigated thermosetting systems.

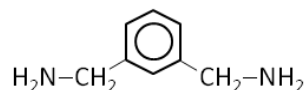


**Figure 8.1.** Chemical structure of the MXDA curing agent.

The triblock copolymer PEO-*b*-PPO-*b*-PEO (**Figure 8.2**), purchased from Sigma-Aldrich, had a number average molecular weight ( $M_n$ ) of 5800 g/mol and 30 wt % of PEO content.

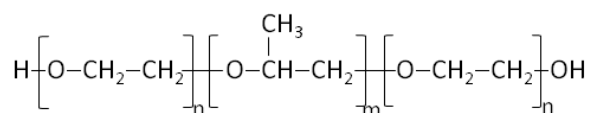


**Figure 8.2.** Chemical structure of the PEO-*b*-PPO-*b*-PEO triblock copolymer.

### 8.2.2. PEO-*b*-PPO-*b*-PEO/(DGEBA-MXDA) cured thermosetting system preparation

The neat DGEBA-MXDA cured system was prepared by mixing DGEBA resin with MXDA in stoichiometric proportions using a magnetic stirrer. After stirring it for around 10 minutes, when the mixture was homogeneous, it was degassed under vacuum at ambient temperature. Then, the mixture was poured into a glass mold to be cured.

To prepare the PEO-*b*-PPO-*b*-PEO/(DGEBA-MXDA) cured systems, firstly a certain amount of PEO-*b*-PPO-*b*-PEO block copolymer was dissolved in DGEBA resin. This mixture was heated at around 60 °C in order to melt the block copolymer and favor its solution and then continuously stirred until a complete homogenization was achieved. A stoichiometric amount of MXDA was then added and the same procedure as for the neat DGEBA-MXDA system was followed. All investigated systems were first cured at 25 °C for 12 h, followed by 9 h at 35 °C, 2 h at 50 °C and finally 1 h at 150 °C. This procedure was chosen to avoid long time curing in high temperature. Apart from the neat DGEBA-MCDEA cured system, four thermosetting systems were prepared, with 5, 15, 25 and 50 wt % of PEO-*b*-PPO-*b*-PEO block copolymer. Plates of 1 mm and 1.5 mm thick were prepared.

### 8.2.3. Characterization techniques

#### 8.2.3.1. Differential scanning calorimeter

DSC measurements were performed using a Mettler Toledo DSC 822<sup>e</sup> differential scanning calorimeter. Thermal transition temperatures of cured thermosetting systems were determined by dynamic scans performed from -25 to 220 °C with a heating rate of 5 °C/min. Prior to this scan, a heating from -25 to 220 °C followed by a cooling from 220 to -25 °C was carried out in order to delete the thermal history of the material. All experiments were conducted under a nitrogen flow of 10 mL/min using 10-15 mg samples in aluminum pans.

#### 8.2.3.2. Atomic force microscopy

AFM images were obtained under ambient conditions using a scanning probe microscope (Nanoscope IIIa Multimode™, Digital Instruments). Tapping mode (TM) was employed in air using an integrated tip/cantilever (125 µm in length with ca. 300 kHz resonant frequency). Typical scan rates during recording were 0.7–1 line/s using a scan head with a maximum range of 16 µm x 16 µm. Transverse cross section surface of each investigated thermosetting system was cut using an ultramicrotome Leica Ultracut R with a diamond blade.

#### 8.2.3.3. Transmission electron microscopy

For TEM measurements, samples were prepared by using an ultramicrotome Leica EMFCS instrument equipped with a diamond knife at room temperature. A Tecnai G2 20 Twin transmission electron microscope operated at 200 kV with resolution of 2.5 Å was used. Moreover, TEM samples were stained in RuO<sub>4</sub> vapor for 4 min in order to enhance the contrast between micro-separated PPO rich phase and epoxy rich phase.

#### 8.2.3.4. Materials testing system

Flexural tests were carried out using the MTS (model Insight 10) provided with a 250 N load cell and following the ASTM D790-10 standard test method, as detailed in Chapter 2. The support span was 24 mm, the crosshead rate 5.6 mm/min and

specimen dimensions 36 mm × 9 mm × 1.5 mm (rectangular shape).

Fracture toughness tests were performed according to ASTM D5045-99 standard test method using the same MTS as for flexural tests, also as detailed in Chapter 2. The support span was 24 mm, the crosshead rate 10 mm/min and single edge notched specimens (SENB) with dimensions of 27 mm × 6 mm × 1.5 mm were used. Initially a sharp notch of around 2.7 mm was made by machining, and subsequently a natural crack was initiated using a razor blade.

For both flexural and fracture toughness tests more than five specimens for each system were tested. The 50 wt % PEO-*b*-PPO-*b*-PEO/(DGEBA-MXDA) cured system could not be analyzed in terms of its mechanical properties as it resulted to be easily breakable.

#### 8.2.3.5. PeakForce quantitative nanomechanical mapping

PeakForce QNM modulus images were captured using Dimension Icon AFM microscope from Bruker. Measurements were carried out in PeakForce mode under ambient conditions. A silicon tip with nominal radius of 10 nm, cantilever length of 125 μm, and resonance frequency of 150 kHz was used. The measurements were performed with a calibrated optical sensitivity. The exact spring constant of the tip was calculated using the Thermal Tune option and a defined tip radius was adjusted using PS as standard.

#### 8.2.3.6. Ultraviolet-visible spectroscopy

UV-vis transmittance spectra of the thermosetting system sheets (thickness of 1 mm) were obtained using a spectrophotometer (Shimadzu UV-3600) in the range between 200 and 800 nm.

#### 8.2.3.7. Contact angle

Water contact angle measurements were carried out using Data Physics OCA 20 contact angle system at ambient temperature. 5 μL distilled water drop was used for each measurement. At least five measurements were made for each different system.

### 8.3. Results and discussion

#### 8.3.1. Characterization of the neat DGEBA-MXDA cured system and PEO-*b*-PPO-*b*-PEO/(DGEBA-MXDA) cured systems

##### 8.3.1.1. Transparency

Different contents of PEO-*b*-PPO-*b*-PEO block copolymer were dissolved in the uncured DGEBA resin resulting in transparent and homogeneous mixtures. This could indicate the partial miscibility between DGEBA and PEO-*b*-PPO-*b*-PEO block copolymer. Moreover, the visual transparency of the cured thermosetting systems was studied. **Figure 8.3** shows that all investigated cured systems (1 mm thick) were optically transparent. In the case of 50 wt % PEO-*b*-PPO-*b*-PEO content, the transparency decreased significantly, although it remained transparent. This fact suggests that all investigated systems presented a microphase separation and the 50 wt % PEO-*b*-PPO-*b*-PEO cured system could probably present a macrophase separation.



**Figure 8.3.** Visual appearance of the neat DGEBA-MXDA cured system (a) and 5 (b), 15 (c), 25 (d) and 50 (e) wt % PEO-*b*-PPO-*b*-PEO/(DGEBA-MXDA) cured systems.

##### 8.3.1.2. Miscibility and thermal behavior

All investigated cured thermosetting systems were studied by dynamic DSC analysis. **Figure 8.4** shows the DSC thermograms of the second heating scan applied to the neat DGEBA-MXDA cured system and PEO-*b*-PPO-*b*-PEO/(DGEBA-MXDA) cured systems. As has been published in literature, PEO-*b*-PPO-*b*-PEO block copolymer has a  $T_g$  around  $-63$  °C attributable to the amorphous PPO block and a melting point around  $30-40$  °C, which corresponds to the semicrystalline PEO block [9,10,12]. In our case, the  $T_g$  of the PEO-*b*-PPO-*b*-PEO block copolymer could not be seen in any of

the thermograms of **Figure 8.4** as the performed scans started from  $-25\text{ }^{\circ}\text{C}$  and the  $T_g$  should appear at a temperature near  $-63\text{ }^{\circ}\text{C}$ .

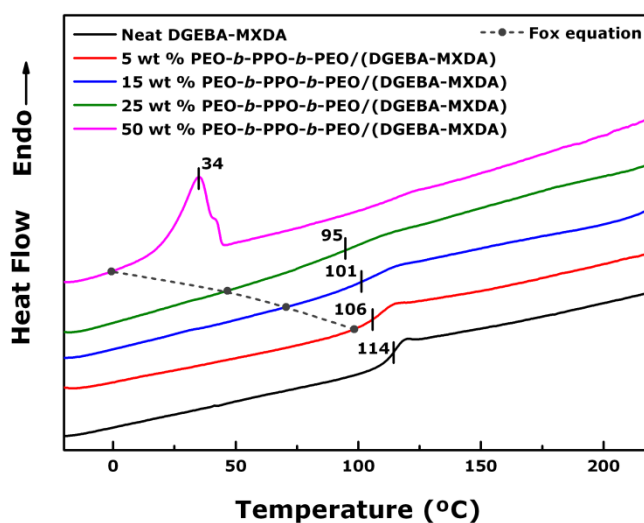


**Figure 8.4.** DSC thermograms of the neat DGEBA-MXDA cured system and 5, 15, 25 and 50 wt % PEO-*b*-PPO-*b*-PEO/(DGEBA-MXDA) cured systems. The dot line indicates the theoretical  $T_g$  values calculated by the Fox equation.

In the PEO-*b*-PPO-*b*-PEO/(DGEBA-MXDA) cured systems with a content of PEO-*b*-PPO-*b*-PEO block copolymer less than 50 wt %, no melting point was detected revealing that at those low contents of PEO-*b*-PPO-*b*-PEO block copolymer, the PEO-*b*-PPO-*b*-PEO/(DGEBA-MXDA) cured systems did not show crystallinity and the PEO block of the PEO-*b*-PPO-*b*-PEO block copolymer was partially miscible with the thermoset matrix [10]. In order to confirm the partial miscibility between PEO-*b*-PPO-*b*-PEO block copolymer and DGEBA-MXDA system, the Fox theoretical equation was employed as in Chapter 7 [17]. Experimental  $T_g$  value of the DGEBA-MXDA matrix decreased with the increase of PEO-*b*-PPO-*b*-PEO block copolymer content in investigated thermosetting systems similarly to the tendency showed by the theoretical  $T_g$ s calculated by Fox equation (**Figure 8.4**), confirming the partial miscibility between PEO-*b*-PPO-*b*-PEO block copolymer and the thermoset matrix.

In the case of the 50 wt % PEO-*b*-PPO-*b*-PEO/(DGEBA-MXDA) cured system, a melting peak at around  $34\text{ }^{\circ}\text{C}$  was observed, exactly where the melting point corresponding to PEO block of the PEO-*b*-PPO-*b*-PEO block copolymer was expected to appear, suggesting that for 50 wt % PEO-*b*-PPO-*b*-PEO content and higher contents some part of the crystalline PEO blocks phase separated with the PPO block.

Therefore, some part of the PEO block is not miscible with the thermoset system and consequently the crystallization of this block might occur and PEO block macrophase separated within PPO block as will be shown below employing the AFM technique.

On the other hand, the neat epoxy system exhibited a clear  $T_g$  around 114 °C. The addition of PEO-*b*-PPO-*b*-PEO block copolymer to the thermoset matrix led to a decrease in the  $T_g$  corresponding to the thermoset matrix as occurred in Chapter 7. Moreover, when the addition of PEO-*b*-PPO-*b*-PEO block copolymer increased, the  $T_g$  value tended to be lower, which corroborated that the PEO-*b*-PPO-*b*-PEO block copolymer was partially miscible with the thermoset matrix. Additionally, it should be taken into account that the presence of the PEO-*b*-PPO-*b*-PEO block copolymer in the systems had a plasticization effect which resulted in a reduction in the cross-linking density of the network [10]. As a consequence of this fact, a higher amount of PEO-*b*-PPO-*b*-PEO block copolymer added to the neat DGEBA-MXDA cured system led to a decrease in the  $T_g$  of the systems.

#### 8.3.1.3. Morphology

The morphologies of the neat DGEBA-MXDA cured system as well as PEO-*b*-PPO-*b*-PEO/(DGEBA-MXDA) cured systems were investigated by AFM and TEM. All investigated system images are in good agreement with the results obtained by DSC and with the visual transparency. As is shown in **Figure 8.5**, AFM phase image of the neat DGEBA-MXDA cured system presents a regular and homogeneous morphology with absence of macro and microphase separation.

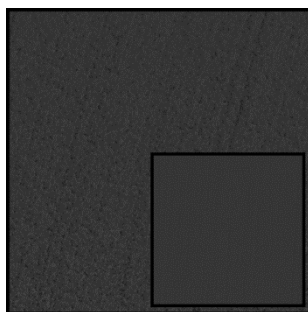


**Figure 8.5.** AFM phase image (1  $\mu\text{m}$  x 1  $\mu\text{m}$  and inset of 5  $\mu\text{m}$  x 5  $\mu\text{m}$ ) of the neat DGEBA-MXDA cured system.

On the other hand, **Figure 8.6** shows the AFM phase images of PEO-*b*-PPO-*b*-PEO/(DGEBA-MXDA) cured systems with 5, 15, 25 and 50 wt % PEO-*b*-PPO-*b*-PEO block

copolymer content. As can be observed, all investigated PEO-*b*-PPO-*b*-PEO/(DGEBA-MXDA) cured systems showed microphase separation except for the 50 wt % PEO-*b*-PPO-*b*-PEO/(DGEBA-MXDA) cured system, where a macrophase separation can be clearly distinguished.

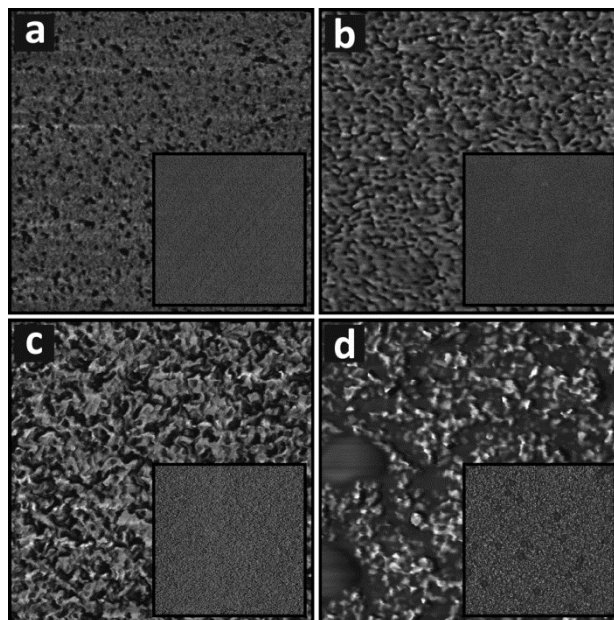


**Figure 8.6.** AFM phase images (1  $\mu\text{m}$  x 1  $\mu\text{m}$  and inset of 5  $\mu\text{m}$  x 5  $\mu\text{m}$ ) of 5 (a), 15 (b), 25 (c) and 50 (d) wt % PEO-*b*-PPO-*b*-PEO/(DGEBA-MXDA) cured systems.

In the case of 5 wt % PEO-*b*-PPO-*b*-PEO/(DGEBA-MXDA) cured system (**Figure 8.6a**), the nanostructure presented spherical morphology, where the dark spherical domains with a size between 10 and 30 nm corresponding to the PPO block rich phase appeared dispersed in a continuous PEO block/(DGEBA-MXDA) rich phase. As has been studied by other authors, physical interactions such as hydrogen bonds are formed between the OH groups initially existing in the neat DGEBA-MXDA uncured system or the ones generated during the curing and the ether group of the PEO block of the PEO-*b*-PPO-*b*-PEO block copolymer [11,14,19,20]. Consequently, PEO block is partially miscible with the thermoset matrix [11,15,17,20] and PPO block appeared as a microseparated phase.

As is observed in **Figures 8.6b** and **8.6c**, when the content of PEO-*b*-PPO-*b*-PEO block copolymer increased, the spherical morphology changed to a mainly worm-like morphology, presenting wider and longer worm-like domains when the content of PEO-*b*-PPO-*b*-PEO block copolymer increased to 25 wt % [8,9,21,22]. The size of the wormlike domains increased from 10 to 10-20 nm in diameter and from 60 nm to a wide range of lengths between 60 and 150 nm probably due to the fact that with 25 wt % of PEO-*b*-

PPO-*b*-PEO block copolymer content some part of PEO block could microseparate together with the PPO block, following the same tendency observed in Chapter 7 when the content of PS-*b*-PMMA block copolymer increased.

With the addition of even higher amount of PEO-*b*-PPO-*b*-PEO block copolymer, the 50 wt % PEO-*b*-PPO-*b*-PEO/(DGEBA-MXDA) cured system (**Figure 8.6d**) showed a macrophase separation that coexisted with a microphase separation. The macrophase separation occurred probably due to the fact that the high PPO block content tended to macroseparate and some part of the PEO block separated with the PPO block. Consequently, PPO block rich phase appeared in some regions as a macroseparated phase and coexisted with a nanostructured morphology, where worm-like domains were the matrix, contrary to the case of 25 wt % PEO-*b*-PPO-*b*-PEO/(DGEBA-MXDA) system. This fact is in good agreement with the results obtained by DSC. In order to perceive these structures and the influence of the concentration of PEO-*b*-PPO-*b*-PEO block copolymer on the morphology, schematic representations of the different proposed morphologies are shown in **Figure 8.7**.

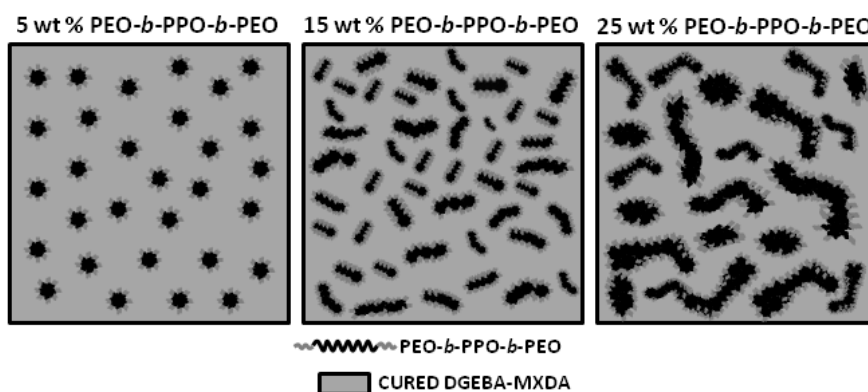


**Figure 8.7.** Schematic representation of the morphologies obtained for 5, 15 and 25 wt % PEO-*b*-PPO-*b*-PEO/(DGEBA-MXDA) cured systems.

The morphologies of all investigated thermosetting systems except for the one with 50 wt % PEO-*b*-PPO-*b*-PEO block copolymer content were also studied by TEM. TEM micrographs presented in **Figure 8.8** confirmed the morphologies obtained by AFM. A microphase separation can be observed in all studied thermosetting systems except for the neat DGEBA-MXDA cured system (**Figure 8.8a**).

The dark areas correspond to PPO microseparated phase due to the fact that the PPO block was preferentially stained with RuO<sub>4</sub> compared to the cured thermoset

matrix [10]. However, it should be pointed out that the difference between both phases was not very obvious because both blocks have a similar chemical structure and as a result of that RuO<sub>4</sub> could stain not only PPO block but also the phase composed of thermoset system and PEO block. Moreover, PEO block was distributed between the two phases as this block is partially miscible in the epoxy based thermoset system but at the same time it is linked covalently to the separated PPO block. Owing to these reasons, the difference between two phases was not as clear as in the AFM images.

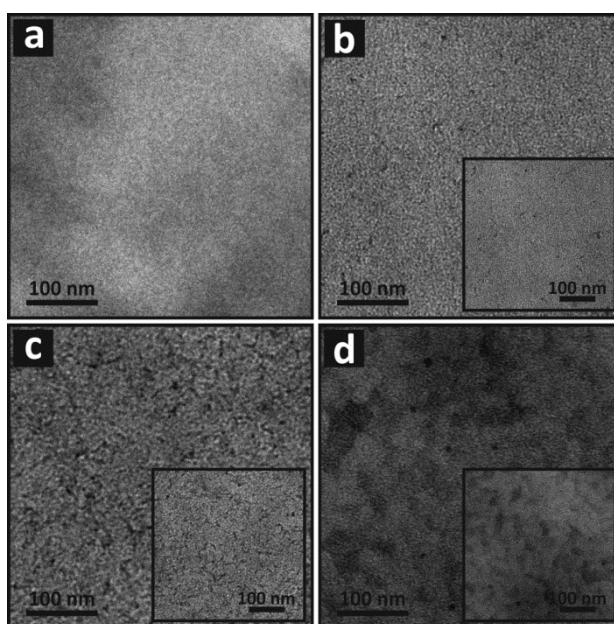


**Figure 8.8.** TEM micrographs of the neat DGEBA-MXDA cured system (a) and 5 (b), 15 (c) and 25 (d) wt % PEO-*b*-PPO-*b*-PEO/(DGEBA-MXDA) cured systems.

In spite of this fact, in the case of 5 wt % PEO-*b*-PPO-*b*-PEO/(DGEBA-MXDA) cured system (**Figure 8.8b**), some dark spherical domains can be seen, whereas when the content of block copolymer increases, the morphology changes from spherical domains to worm-like structure. When 25 wt % PEO-*b*-PPO-*b*-PEO was added to the matrix (**Figure 8.8d**), the microseparated PPO phase became bigger and wider, which is in good agreement with the AFM results.

#### 8.3.1.4. Mechanical properties

The mechanical properties of all investigated cured systems (except for the 50 wt % PEO-*b*-PPO-*b*-PEO/(DGEBA-MXDA) cured system) were studied in terms of the

flexural modulus ( $E$ ), the critical stress intensity factor ( $K_{IC}$ ) and the critical strain energy release rate ( $G_{IC}$ ).

As can be observed in **Figure 8.9**, the flexural modulus of the PEO-*b*-PPO-*b*-PEO/(DGEBA-MXDA) cured systems not only was lower than the flexural modulus of the neat DGEBA-MXDA system, but also it decreased when the added block copolymer amount increased. This phenomenon was expected taking into account the evidences found by many authors confirming that the addition of a block copolymer decreases the flexural modulus of the neat epoxy based thermoset resin [17,23-26]. This could occur due to the fact that the modifier added has a lower modulus than the neat thermosetting matrix and that the thermosetting system was partially miscible with PEO-*b*-PPO-*b*-PEO block copolymer [17]. As mentioned before, the addition of PEO-*b*-PPO-*b*-PEO block copolymer provoked a plasticization effect [9] in the blend together with a reduction in the cross-linking density of the network [9,27]. Consequently, the higher the content of block copolymer, the lower the flexural modulus of the thermosetting system.

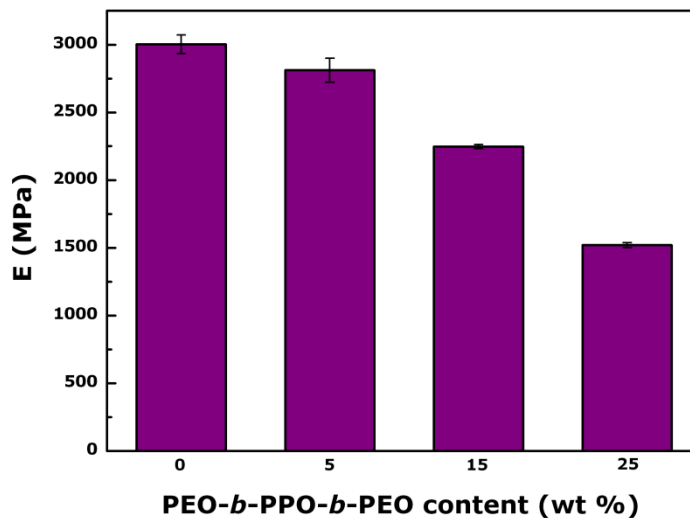


**Figure 8.9.** Flexural modulus ( $E$ ) of the neat DGEBA-MXDA cured system and 5, 15 and 25 wt % PEO-*b*-PPO-*b*-PEO/(DGEBA-MXDA) cured systems.

On the other hand, it should be indicated that the flexural modulus of the neat DGEBA-MXDA cured system resulted to be slightly higher than flexural moduli reported by other authors [17,26,28,29].

**Figure 8.10** shows the  $K_{IC}$  and the  $G_{IC}$  values for each system with a different content of PEO-*b*-PPO-*b*-PEO block copolymer. The toughness of the mixtures increased in respect to the neat DGEBA-MXDA cured system with the addition of 5 and

15 wt % of PEO-*b*-PPO-*b*-PEO block copolymer, obtaining an improvement of 30 % in the toughness in the case of 5 wt % PEO-*b*-PPO-*b*-PEO/(DGEBA-MXDA) cured system and of 14 % in the case of 15 wt % PEO-*b*-PPO-*b*-PEO/(DGEBA-MXDA) cured system. Even if the addition of the block copolymer provoked deterioration in the flexural behavior, here it can be seen that the blending of the thermosetting system with the block copolymer is worthy considering its improvement in the toughness [17,23-26].

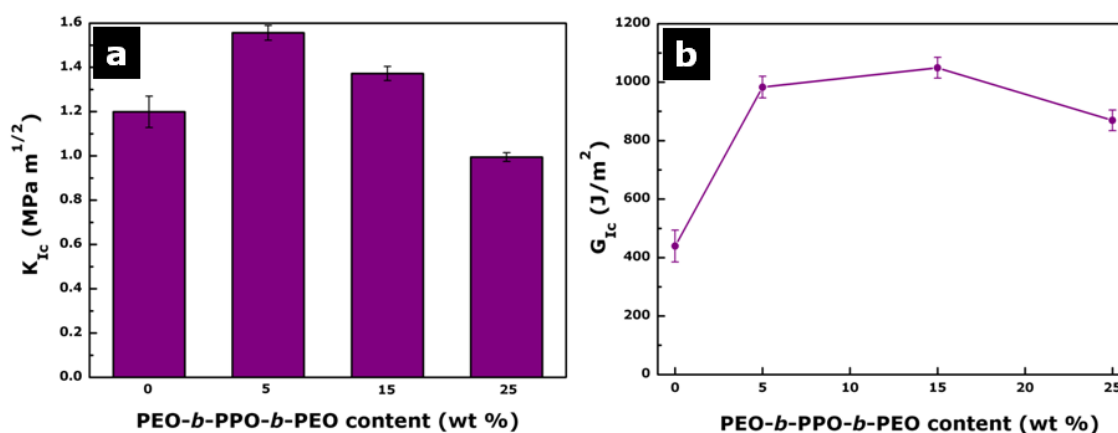


**Figure 8.10.** Critical stress intensity factor ( $K_{IC}$ ) (a) and critical strain energy release rate ( $G_{IC}$ ) (b) of the neat DGEBA-MXDA cured system and 5, 15 and 25 wt % PEO-*b*-PPO-*b*-PEO/(DGEBA-MXDA) cured systems.

The values of  $K_{IC}$  suggested that systems with microdomains of smaller size presented a higher improvement of toughness on the contrary to what was observed in Chapter 7, and when the content of PEO-*b*-PPO-*b*-PEO block copolymer increased and microdomains size became higher, the values of  $K_{IC}$  started to decrease in comparison with the 5 wt % PEO-*b*-PPO-*b*-PEO/(DGEBA-MXDA) cured system. As reported in literature, mechanical properties are related to the degree of polymerization of the thermoset [30,31] and to the morphology of the final material [2,17,23,26,32-34], which is governed by several parameters such as the volume fraction of each block [17,23,35], the block copolymer content [9,17] and miscibility of blocks [23,27].

On the other hand, on the contrary to what was observed in Chapter 7, in this case, both  $K_{IC}$  and  $G_{IC}$  do not follow exactly the same tendency [9,27]. This is related not only to the physical meaning of these two parameters but also to the calculation method used to determine them. Thus,  $K_{IC}$  mainly depends on the maximum load at which the specimen fails in the three bending test or the highest value of the load-

displacement curve, whereas  $G_{IC}$  determined by the procedure used in this study mainly depends on the area under the curve obtained during the three bending test. Consequently, depending on the flexural modulus, which is related with the slope of the load-displacement curve,  $K_{IC}$  and  $G_{IC}$  might not follow the same trend. For example, the  $K_{IC}$  corresponding to 15 wt % PEO-*b*-PPO-*b*-PEO/(DGEBA-MXDA) cured system is lower than the  $K_{IC}$  corresponding to 5 wt % PEO-*b*-PPO-*b*-PEO/(DGEBA-MXDA) cured system, but as the flexural modulus decreases from 5 to 15 wt % PEO-*b*-PPO-*b*-PEO/(DGEBA-MXDA) cured system, the final area under the curve is bigger in the case of 15 wt % PEO-*b*-PPO-*b*-PEO/(DGEBA-MXDA) cured system, which leads to a higher  $G_{IC}$  value. Anyway, it should be also mentioned that the difference between the  $G_{IC}$  values corresponding to 5 and 15 wt % PEO-*b*-PPO-*b*-PEO/(DGEBA-MXDA) cured systems is not very high if the error bars are taken into account.

Quantitative nanomechanical properties (QNM) of the neat DGEBA-MXDA cured system and DGEBA-MXDA cured system modified with different PEO-*b*-PPO-*b*-PEO block copolymer contents were investigated using AFM in PeakForce mode. The elastic modulus PeakForce QNM images of all investigated thermosetting systems are showed in **Figure 8.11**.

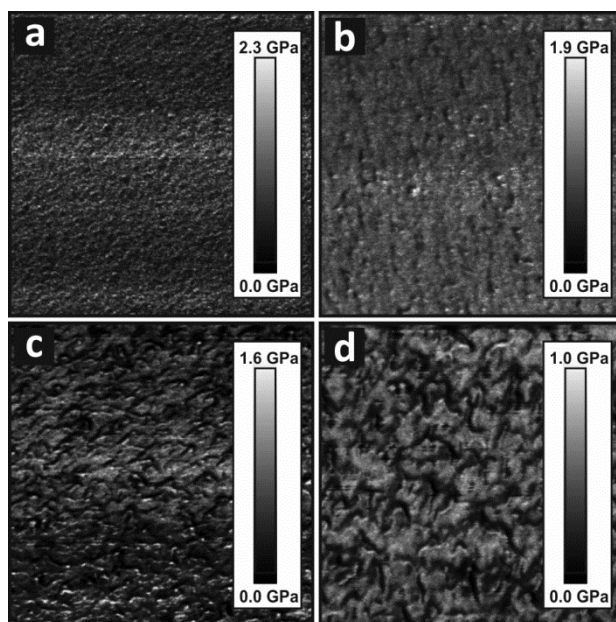


**Figure 8.11.** Elastic modulus PeakForce QNM images (1  $\mu\text{m}$  x 1  $\mu\text{m}$ ) of the neat DGEBA-MXDA cured system (a) and 5 (b), 15 (c) and 25 (d) wt % PEO-*b*-PPO-*b*-PEO/(DGEBA-MXDA) cured systems.

First of all, it should be pointed out that the morphologies detected for the four systems analyzed by PeakForce are very similar to the morphologies detected by AFM.

The modulus PeakForce QNM image of the neat DGEBA-MXDA cured system (**Figure 8.11a**) presents a quite homogeneous morphology which indicates that this system has almost the same elastic modulus value, being around 2.3 GPa, in every measured point of the investigated system surface.

However, in the modulus PeakForce QNM images of thermosetting systems modified with PEO-*b*-PPO-*b*-PEO block copolymer two different phases can be distinguished, suggesting that there are different zones with different elastic values. From the comparison between AFM and PeakForce QNM images, one can conclude that there is a clear correspondence between the phases observed in AFM and the ones observed in PeakForce QNM, which means that the highest elastic modulus (brightest phase in QNM) would correspond to the PEO block/(DGEBA-MXDA) rich phase and the lowest elastic modulus (darkest phase in QNM) would correspond to the separated PPO phase.

On the other hand, the elastic modulus value of the neat DGEBA-MXDA cured system decreased when the thermosetting system is modified with the PEO-*b*-PPO-*b*-PEO block copolymer, being the elastic modulus values of modified systems 1.9, 1.6 and 1.0 GPa, for 5, 15, and 25 wt % PEO-*b*-PPO-*b*-PEO/(DGEBA-MXDA) cured systems, respectively. For the 25 wt % PEO-*b*-PPO-*b*-PEO/(DGEBA-MXDA) cured system the modulus value is more than two times lower than the elastic modulus of the neat DGEBA-MXDA cured system. This fact confirms once again that PEO block is partially miscible with the DGEBA-MXDA cured system but that its addition provokes a decrease in the elastic modulus probably since the PEO block has a lower modulus than the matrix, showing a behavior similar to that seen for the flexural modulus studied at macroscale.

In addition, the elastic modulus values of the microseparated PPO block phase were lower than those of the PEO block/(DGEBA-MXDA) rich phase, and much lower than the modulus of the neat DGEBA-MXDA cured system, being of 1.1, 0.9 and 0.8 GPa for 5, 15, and 25 wt % PEO-*b*-PPO-*b*-PEO/(DGEBA-MXDA) cured systems, respectively.

#### 8.3.1.5. Optical properties

UV-vis measurements were carried out to study the optical transparency of the thermosetting systems. **Figure 8.12** shows the UV-vis transmittance spectra of the neat

DGEBA-MXDA cured system and all investigated PEO-*b*-PPO-*b*-PEO/(DGEBA-MXDA) cured systems. Although **Figure 8.3** had presented a clear visual transparency for all systems, here it can be seen that the transmittances were not very high even for the neat DGEBA-MXDA cured system. The transmittance could be related with the thickness of the cured systems, that in this case was 1 mm. Moreover, other authors have reported similar transmittance values for neat epoxy based thermosetting system [36,37].

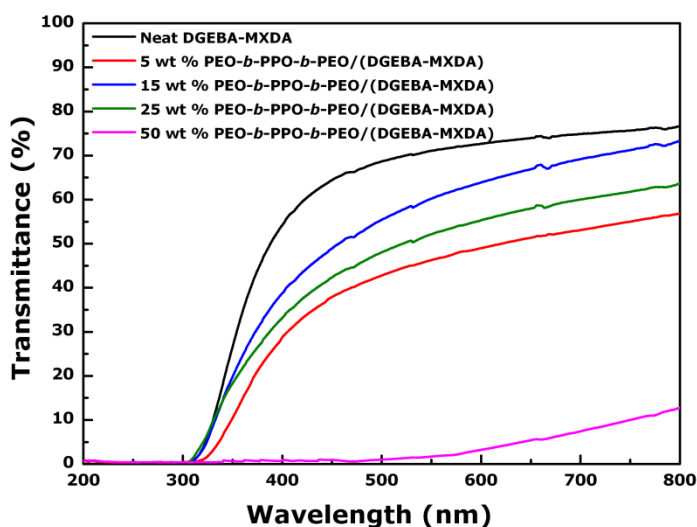


**Figure 8.12.** UV-vis transmittance spectra of the neat DGEBA-MXDA cured system and 5, 15, 25 and 50 wt % PEO-*b*-PPO-*b*-PEO/(DGEBA-MXDA) cured systems.

The neat DGEBA-MXDA cured system exhibited the highest UV-vis transmittance and when PEO-*b*-PPO-*b*-PEO block copolymer was added to the thermoset matrix the transmittance of PEO-*b*-PPO-*b*-PEO modified systems slightly decreased indicating that PEO-*b*-PPO-*b*-PEO block copolymer had a weak effect of light absorption in both visible and UV ranges. The most important decrease was observed in the case of 50 wt % PEO-*b*-PPO-*b*-PEO/(DGEBA-MXDA) cured system, which had a transmittance lower than 15 % in the visible range and a value near to zero in the UV range. This fact is related to the low visual transparency observed for the 50 wt % PEO-*b*-PPO-*b*-PEO/(DGEBA-MXDA) cured system in **Figure 8.3**.

Comparing to the neat epoxy system, 5, 15 and 25 wt % PEO-*b*-PPO-*b*-PEO/(DGEBA-MXDA) cured systems had a lower transmittance, being the 5 wt % PEO-*b*-PPO-*b*-PEO/(DGEBA-MXDA) cured system the one with a lower transmittance. This could be attributed to the following phenomenon. In the case of a low content of PEO-*b*-PPO-*b*-PEO

block copolymer (5 wt %), the PEO block was present in an even lower concentration in respect to the PPO block content. In fact, in the 5 wt % PEO-*b*-PPO-*b*-PEO/(DGEBA-MXDA) cured system, only the 1.5 wt % of the thermosetting system corresponded to the PEO block. This low content of PEO block provoked that even if PEO block was partially miscible with the epoxy based thermoset matrix, it tended to microseparate together with the immiscible PPO block instead of being partially mixed with the thermoset system. Therefore, at this content of block copolymer, PEO-*b*-PPO-*b*-PEO block copolymer could not be completely mixed with the thermosetting matrix. This could affect to the transmittance of the thermosetting system, reducing it as is revealed in **Figure 8.12**.

#### 8.3.1.6. Surface properties

The changes in the hydrophilic nature of PEO-*b*-PPO-*b*-PEO/(DGEBA-MXDA) cured systems with varying block copolymer content and comparison with the neat DGEBA-MXDA cured system were analyzed by contact angle measurements. Moreover, the surface free energies ( $\gamma_{sv}$ ) were calculated from the contact angle ( $\theta$ ) data by using the Berthelot's rule [38,39], where  $\gamma_{lv}$  is the water surface tension:

$$\gamma_{sv} = \frac{(1 + \cos \theta)^2}{4} \gamma_{lv}$$

As is observed in the data of the **Table 8.1**, the contact angle of the systems decreased and the surface free energy increased with the addition of PEO-*b*-PPO-*b*-PEO block copolymer.

**Table 8.1.** Water contact angle and surface free energy values of the neat DGEBA-MXDA cured system and investigated PEO-*b*-PPO-*b*-PEO/(DGEBA-MXDA) cured systems.

System	Contact angle (°)	$\gamma_{sv}$ (mN/m)
Neat DGEBA-MXDA	83.4 ± 1.6	22.6
5 wt % PEO- <i>b</i> -PPO- <i>b</i> -PEO/(DGEBA-MXDA)	79.8 ± 3.1	25.2
15 wt % PEO- <i>b</i> -PPO- <i>b</i> -PEO/(DGEBA-MXDA)	71.1 ± 1.1	31.9
25 wt % PEO- <i>b</i> -PPO- <i>b</i> -PEO/(DGEBA-MXDA)	69.1 ± 2.8	33.5
50 wt % PEO- <i>b</i> -PPO- <i>b</i> -PEO/(DGEBA-MXDA)	29.5 ± 2.9	63.7

The surface became more hydrophilic with increasing the content of PEO-*b*-PPO-*b*-PEO block copolymer in the system. Thus, the most hydrophobic system was the neat DGEBA-MXDA one, whereas the most hydrophilic one was the 50 wt % PEO-*b*-PPO-*b*-PEO/(DGEBA-MXDA) one. This could be attributed to the hydrophilic character of well-distributed PEO block microseparated domains of the block copolymer [40] and to the existence of PEO block at the surface of the samples. The increase of the hydrophilic character of the systems can be also observed in the images of **Figure 8.13**.

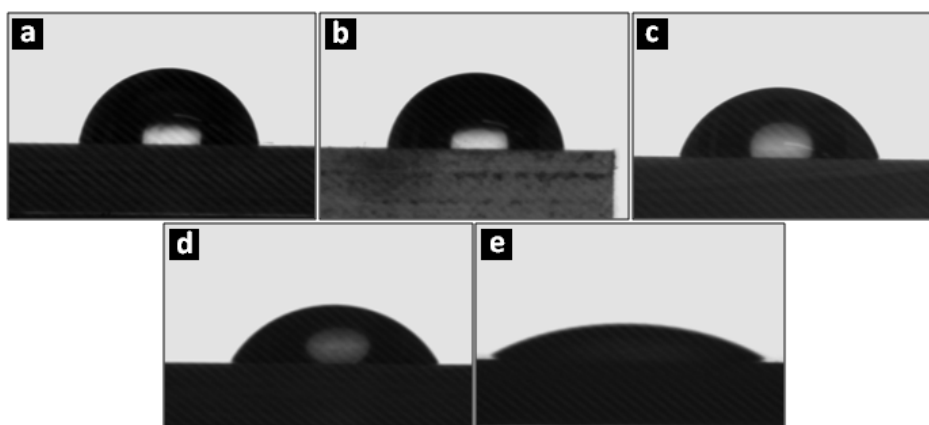


**Figure 8.13.** Images of a water droplet in contact with the neat DGEBA-MXDA cured system (a) and 5 (b), 15 (c), 25 (d) and 50 (e) wt % PEO-*b*-PPO-*b*-PEO/(DGEBA-MXDA) cured systems.

#### 8.4. Conclusions

Epoxy based nanostructured thermosetting systems modified with different contents of PEO-*b*-PPO-*b*-PEO block copolymer were successfully prepared. The incorporation of PEO-*b*-PPO-*b*-PEO block copolymer into the DGEBA-MXDA system resulted to be an effective method to improve the toughness of the epoxy system as well as to obtain well nanostructured thermosetting systems.

The curing process was carried out at 25 °C owing to the lower critical solution temperature (LCST) behavior of the block copolymer. The addition of the block copolymer to the DGEBA-MXDA system caused a decrease in the  $T_g$  of the systems compared to the neat DGEBA-MXDA cured system  $T_g$ , due to the plasticization effect provoked by the addition of the block copolymer.

As was confirmed by AFM and TEM, the cured thermosetting systems showed well nanostructured morphologies up to 25 wt % PEO-*b*-PPO-*b*-PEO content, where the microseparated phase corresponded to PPO block rich phase. The morphology

obtained resulted to be dependent of the PEO-*b*-PPO-*b*-PEO block copolymer content and it changed from spherical structure to worm-like structure with the content of block copolymer.

Regarding the mechanical properties, the toughness improved considerably with 5 and 15 wt % PEO-*b*-PPO-*b*-PEO block copolymer contents and it almost remained the same with 25 wt % content. The elastic modulus measured by QNM decreased with the addition of PEO-*b*-PPO-*b*-PEO block copolymer, easily distinguishing two phases with different modulus values.

UV-vis measurements mainly indicated a slight decrease in the transmittance with the increase of PEO-*b*-PPO-*b*-PEO block copolymer content. This decrease of transmittance was also reflected in the visual appearance of the investigated thermosetting systems, although all investigated systems remained transparent. Finally, the mixture with PEO-*b*-PPO-*b*-PEO block copolymer made the surface of thermosetting systems more hydrophilic.

## 8.5. References

- [1] J. M. Dean, N. E. Verghese, H. Q. Pham, F. S. Bates, *Macromolecules* 2003, **36** 9267-9270.
- [2] J. Liu, Z. J. Thompson, H. J. Sue, F. S. Bates, M. A. Hillmyer, M. Dettloff, G. Jacob, N. Verghese, H. Pham, *Macromolecules* 2010, **43**, 7238-7243.
- [3] R. B. Grubbs, J. M. Dean, F. S. Bates, *Macromolecules* 2001, **34**, 8593-8595.
- [4] S. Ritzenthaler, F. Court, E. Girard-Reydet, L. Leibler, J. P. Pascault, *Macromolecules* 2003, **36**, 118-126.
- [5] V. Rebizant, A. S. Venet, F. Tournilhac, E. Girard-Reydet, C. Navarro, J. P. Pascault, L. Leibler, *Macromolecules* 2004, **37**, 8017-8027.
- [6] H. Kosonen, J. Ruokolainen, M. Torkkeli, R. Serimaa, P. Nyholm, O. Ikkala, *Macromol. Chem. Physic.* 2002, **203**, 388-392.
- [7] N. Boyard, C. Sinturel, M. Vayer, R. J. Erre, *Appl. Polym. Sci.* 2006, **102**, 149-165.
- [8] D. H. Builes, A. Tercjak, I. Mondragon, *Polymer* 2012, **53**, 3669-3676.
- [9] D. H. Builes, H. Hernandez, I. Mondragon, A. Tercjak, *J. Phys. Chem. C* 2013, **117**, 3563-3571.

- [10] Q. Guo, R. Thomann, W. Gronski, *Macromolecules* 2002, **35**, 3133-3144.
- [11] M. Larrañaga, M. D. Martín, N. Gabilondo, G. Kortaberria, M. A. Corcuera, C. C. Riccardi, I. Mondragon, *Polym. Int.* 2004, **53**, 1495-1502.
- [12] P. Sun, Q. Dang, B. Li, T. Chen, Y. Wang, H. Lin, Q. Jin, D. Ding, *Macromolecules* 2005, **38**, 5654-5667.
- [13] M. Larrañaga, N. Gabilondo, G. Kortaberria, E. Serrano, P. Remiro, C. C. Riccardi, I. Mondragon, *Polymer* 2005, **46**, 7082-7093.
- [14] M. Larrañaga, M. D. Martin, N. Gabilondo, G. Kortaberria, A. Eceiza, C. C. Riccardi, I. Mondragon, *Colloid. Polym. Sci.* 2006, **284**, 1403-1410.
- [15] M. Larrañaga, P. Arruti, E. Serrano, K. De la Caba, P. M. Remiro, C. C. Riccardi, I. Mondragon, *Colloid. Polym. Sci.* 2006, **284**, 1419-30.
- [16] K. De la Caba, M. Larrañaga, A. Eceiza, M. A. Corcuera, I. Mondragon, *Macromol. Symp.* 2006, **239**, 30-35.
- [17] M. Larrañaga, E. Serrano, M. D. Martin, A. Tercjak, G. Kortaberria, K. De la Caba, C. C. Riccardi, I. Mondragon, *Polym. Int.* 2007, **56**, 1392-1403.
- [18] C. J. Chang, Y. L. Yang, Y. P. Lee, C. J. Chiang, C. A. Dai, J. C. Chen, Y. Y. Cheng, C. C. Chen, M. W. Liu, W. P. Shih, J. Y. Yen, *Microelectron. Eng.* 2011, **88**, 1737-1741.
- [19] S. M. George, D. Puglia, J. M. Kenny, P. Jyotishkumar, S. Thomas, *Polym. Eng. Sci.* 2012, **52**, 2336-2347.
- [20] Q. Guo, C. Harrats, G. Groeninckx, M. H. J. Koch, *Polymer* 2001, **42**, 4127-4140.
- [21] N. Hameed, Q. Guo, T. Hanley, Y. W. Mai, *J. Polym. Sci. Pol. Phys.* 2010, **48**, 790-800.
- [22] M. Blanco, M. López, G. Kortaberria, I. Mondragon, *Polym. Int.* 2010, **59**, 523-528.
- [23] J. M. Dean, P. M. Lipic, R. B. Grubbs, R. F. Cook, F. S. Bates, *J. Polym. Sci. Pol. Phys.* 2001, **39**, 2996-3010.
- [24] J. M. Dean, R. B. Grubbs, W. Saad, R. F. Cook, F. S. Bates, *J. Polym. Sci. Pol. Phys.* 2003, **41**, 2444-2456.
- [25] J. Wu, Y. S. Thio, F. S. Bates, *J. Polym. Sci. Pol. Chem.* 2005, **43**, 1950-1965.
- [26] C. Ocando, A. Tercjak, E. Serrano, J. A. Ramos, S. Corona-Galván, M. D. Parellada, M. J. Fernández-Berridi, I. Mondragon, *Polym. Int.* 2008, **57**, 1333-1342.
- [27] C. Ocando, A. Tercjak, M. D. Martín, J. A. Ramos, M. Campo, I. Mondragon, *Macromolecules* 2009, **42**, 6215-6224.

- [28] D. Ratna, O. Becker, R. Krishnamurthy, G. P. Simon, R. J. Varley, *Polymer* 2003, **44**, 7449-7457.
- [29] C. Ocando, A. Tercjak, I. Mondragon, *Compos. Sci. Technol.* 2010, **70**, 1106-1112.
- [30] C. M. Sahagun, S. E. Morgan, *ACS Appl. Mater. Interfaces* 2012, **4**, 564-572.
- [31] J. P. Pascault, H. Sautereau, J. Verdu, R. J. J. Williams, *Thermosetting polymers*, Marcel Dekker Inc., New York (USA), 2002 [chapter 11].
- [32] J. M. Dean, P. M. Lipic, R. B. Grubbs, R. F. Cook, F. S. Bates, *J. Polym. Sci. Pol. Phys.* 2001, **39**, 2996-3010.
- [33] Y. S. Thio, J. Wu, F. S. Bates, *J. Polym. Sci. Pol. Phys.* 2009, **47**, 1125-1129.
- [34] D. H. Builes, J. Labidi, A. Eceiza, I. Mondragon, A. Tercjak, *Compos. Sci. Technol.* 2013, **89**, 120-126.
- [35] D. H. Builes, J. P. Hernandez-Ortiz, M. A. Corcuera, I. Mondragon, A. Tercjak, *ACS Appl. Mater. Interfaces* 2014, **6**, 1073-1081.
- [36] K. Mizutani, *J. Mater. Sci.* 1993, **28**, 2178-2182.
- [37] J. Gutierrez, A. Tercjak, I. Mondragon, *J. Phys. Chem. C* 2010, **114**, 22424-22430.
- [38] A. R. Balkenende, H. J. A. P. Van de Boogard, M. Scholten, N. P. Willard, *Langmuir* 1998, **14**, 5907-5912.
- [39] J. Long, P. Chen, *Langmuir* 2001, **17**, 2965-2972.
- [40] P. Alexandridis, *Curr. Opi. Colloid. In.* 1997, **2**, 478-489.



# 9

**General conclusions, future work and  
scientific contributions**



## 9. General conclusions, future work and scientific contributions

### 9.1. General conclusions

The main conclusions of the investigation work presented in this memory are the following:

- Self-assembled PS-*b*-PMMA diblock copolymer can be successfully used as template for the fabrication of different kinds of nanocomposites, with commercial TiO<sub>2</sub> nanocrystals, and synthesized TiO<sub>2</sub> nanorods and  $\gamma$ -Fe<sub>2</sub>O<sub>3</sub> nanocrystals.
- The organic capping layer of synthesized nanoparticles allows to disperse up to high nanoparticles content in the block copolymer, leading to enhanced properties.
- TiO<sub>2</sub>NR/PS-*b*-PMMA nanocomposites show optical properties as well as conductive properties, which open the venue to the integration of such functional nanostructured materials for applications in memory and optoelectronic devices, catalysts, and sensors, as well as in energy conversion fields.
- The achieved nanostructured  $\gamma$ -Fe<sub>2</sub>O<sub>3</sub>NC/PS-*b*-PMMA nanocomposite materials present magnetic properties and are good candidates as functional components in potential applications ranging from magnetic sensors to magnetic information storage.
- The incorporation of both PS-*b*-PMMA diblock copolymer and PEO-*b*-PPO-*b*-PEO triblock copolymer onto an epoxy based thermosetting matrix has resulted to be an effective method to improve the low toughness of epoxy matrices as well as to obtain well nanostructured thermosetting systems.

### 9.2. Future work

In order to continue the investigation work done in this thesis, the following research lines are proposed:

- Perform further and more specific characterization on TiO<sub>2</sub>NR/PS-*b*-PMMA nanocomposites based electro-devices, focusing on the

determination of solar cell efficiency.

- Optimize the TiO<sub>2</sub>NR/PS-*b*-PMMA nanocomposites based electro-devices systems, in order to create effectively applicable devices.
- Incorporate inorganic nanoparticles into epoxy based thermosetting systems or epoxy based thermosetting systems modified with block copolymers, in order to improve mechanical properties together with other properties like optical, conductive or magnetic.
- Develop nanocomposites based on other kinds of block copolymers, and adding different kinds of nanofillers, opening the field also to biopolymers or nanofillers coming from renewable resources, with the aim of directing the application of these materials toward biomedical or environmental applications.

### 9.3. Scientific contributions

#### 9.3.1. Publications

Scientific publications directly related to the investigation work summarized in this report:

- **L. Cano**, J. Gutierrez, A. Tercjak, Rutile TiO<sub>2</sub> nanoparticles dispersed in a self-assembled polystyrene-*block*-polymethyl methacrylate diblock copolymer template, *J. Phys. Chem. C* 2013, **117**, 1151-1156.  
Impact Factor: 4.835, 29 of 251 in Materials Science, Multidisciplinary (JCR 2013). Cited: 8.
- **L. Cano**, D. H. Builes, A. Tercjak, Morphological and mechanical study of nanostructured epoxy systems modified with amphiphilic poly(ethylene oxide-*b*-propylene oxide-*b*-ethylene oxide) triblock copolymer, *Polymer* 2014, **55**, 738-745.  
Impact Factor: 3.562, 16 of 82 in Polymer Science (JCR 2014). Cited: 7.
- **L. Cano**, A. E. Di Mauro, M. Striccoli, M. L. Curri, A. Tercjak, Optical and conductive properties of as-synthesized organic-capped TiO<sub>2</sub> nanorods highly dispersible in polystyrene-*block*-poly(methyl methacrylate) diblock copolymer, *ACS Appl. Mater. Interfaces* 2014, **6**, 11805-11814.

Impact Factor: 6.723, 23 of 260 in Materials Science, Multidisciplinary (JCR 2014).

- **L. Cano**, A. E. Di Mauro, F. Petronella, E. Fanizza, M. Striccoli, M. L. Curri, A. Tercjak, Effect of iron oxide nanocrystal content on the morphology and magnetic properties of polystyrene-*block*-poly(methyl methacrylate) diblock copolymer based nanocomposites, *J. Phys. Chem. C* 2015, **119**, 6435-6445.

Impact Factor: 4.772, 32 of 260 in Materials Science, Multidisciplinary (JCR 2014).

- **L. Cano**, J. Gutierrez, A. E. Di Mauro, M. L. Curri, A. Tercjak, The effect of TiO<sub>2</sub> nanocrystal shape on the electrical properties of poly(styrene-*b*-methyl methacrylate) block copolymer based nanocomposites for solar cell application, *Electrochim. Acta* 2015, **184**, 8-16.

Impact Factor: 4.504, 4 of 28 in Electrochemistry (JCR 2014).

- **L. Cano**, J. Gutierrez, A. Tercjak, Enhancement of the mechanical properties at macro and nanoscale of thermosetting systems modified with polystyrene-*block*-polymethyl methacrylate block copolymer, *ACS Appl. Mater. Interfaces* (submitted).

Other scientific publications:

- A. E. Di Mauro, M. Striccoli, N. Depalo, E. Fanizza, **L. Cano**, C. Ingrosso, A. Agostiano, M.L. Curri, A. Tercjak, Selective confinement of oleylamine capped Au nanoparticles in self-assembled PS-*b*-PEO diblock copolymer templates, *Soft Matter* 2014, **10**, 1676-1684.

Impact Factor: 4.029, 10 of 82 in Polymer Science.

- D. H. Builes, H. Hernández, J. P. Hernández-Ortiz, **L. Cano**, I. Mondragon, A. Tercjak, Nanostructured unsaturated polyester using block copolymers: morphology, optical properties and fracture toughness relationship, *Revista Colombiana de Materiales* 2014, **5**, 35-41.
- J. Gutierrez, R. Fernández, **L. Cano**, D. H. Builes, A. Tercjak, Chapter IV Self-assembled block copolymers for preparation of advanced materials, *Block copolymers: phase morphology, material applications and future*

*challenges*, Nova Science Publishers, Hauppauge (USA), 2014, 113-137, ISBN: 978-1-62948-626-0.

- S. Carrasco-Hernandez, J. Gutierrez, **L. Cano**, A. Tercjak, Thermal and optical behaviour of poly(ethylene-*b*-ethylene oxide) block copolymer dispersed liquid crystals blends, *Eur. Polym. J.* (in second revision).

### 9.3.2. Contributions in conferences

Contributions in conferences directly related to the investigation work summarized in this report:

- **L. Cano**, J. Gutierrez, A. Tercjak, PS-*b*-PMMA block copolymer as template for rutile TiO<sub>2</sub> nanoparticles, NanoSpain 2013, Bilbao (Spain), April 2013, contribution: **poster**. Student grant from **Phantoms Foundation**.
- **L. Cano**, J. Gutierrez, A. Tercjak, Preparation and characterization of hybrid inorganic/organic materials based on PS-*b*-PMMA diblock copolymer and rutile TiO<sub>2</sub> nanoparticles, JIP 2013 Congreso Nacional de Jóvenes Investigadores en Polímeros, Menorca (Spain), May 2013, contribution: **oral communication**.
- **L. Cano**, D. H. Builes, A. Tercjak, Nanostructured epoxy based thermosetting systems modified with poly(ethylene oxide-*b*-propylene oxide-*b*-ethylene oxide) triblock copolymer to enhance fracture toughness, NanoSpain 2014, Madrid (Spain), March 2014, contribution: **poster**. Student grant from **Phantoms Foundation**.
- **L. Cano**, D. H. Builes, A. Tercjak, Nanostructured and toughened thermosetting systems modified with PEO-*b*-PPO-*b*-PEO triblock copolymer, MoDeSt 2014 Conference, Portoroz (Slovenia), August 2014, contribution: **oral communication**. Student grant from **Modest Society**.
- **L. Cano**, J. Gutierrez, A. E. Di Mauro, M. Striccoli, M. L. Curri, A. Tercjak, Optoelectrical characterization of hybrid nanocomposites based on PS-*b*-PMMA diblock copolymer and both commercial and ex situ synthesized colloidal TiO<sub>2</sub> nanoparticles, 8th ECNP International Conference on

Nanostructured Polymers and Nanocomposites, Dresden (Germany), September 2014, contribution: **oral communication**. Grant from **University of the Basque Country (UPV/EHU)**.

- **L. Cano**, A. E. Di Mauro, J. Gutierrez, M. Striccoli, M. L. Curri, A. Tercjak, Hybrid nanocomposite films based on polystyrene-*block*-polymethyl methacrylate block copolymer and synthesized colloidal nanoparticles, NanoSpain Chemistry 2015, Bilbao (Spain), March 2015, contribution: **oral communication**. Student grant from **Phantoms Foundation**.
- **L. Cano**, A. E. Di Mauro, F. Petronella, E. Fanizza, M. Striccoli, M. L. Curri, A. Tercjak, PS-*b*-PMMA diblock copolymer as template for the preparation of nanocomposites with high iron oxide nanocrystal contents, Functional Polymeric Materials Conference, Ascot (United Kingdom), August 2015, contribution: **poster**. Grant from the **organization**.
- **L. Cano**, J. Gutierrez, A. E. Di Mauro, M. L. Curri, A. Tercjak, Nanocomposites based on poly(styrene-*b*-methyl methacrylate) block copolymer modified with TiO<sub>2</sub> nanoparticles for solar cell application, JIP-JEPO 1st French-Spanish Joint Congress for Young Researchers in Polymers, Donostia-San Sebastián (Spain), September 2015, contribution: **oral communication**. **Best talk award** received.

Other contributions in conferences:

- A. Tercjak, J. Gutierrez, **L. Cano**, I. L. Combarro, I. Mondragon, Conductive properties of inorganic/organic nanostructured systems based on block copolymers, PCAM Summer School 2011 Electronic & Optical Properties of Nanoscale Materials, Donostia-San Sebastián (Spain), July 2011, contribution: poster.
- A. Tercjak, J. Gutierrez, D. H. Builes, **L. Cano**, R. Fernández, I. Mondragon, Nanostructured thermosetting systems designed using block copolymers as template for thermo-, photo- and electro-responsive materials, 7th Conference MoDeSt 2012, Prague (Czech Republic), September 2012, contribution: oral communication.
- J. Gutierrez, **L. Cano**, D. H. Builes, R. Fernández, A. Tercjak, Inorganic/organic multiphase nanostructured thermosetting materials,

Hybrid Materials 2013 3rd International Conference on Multifunctional, Hybrid and Nanomaterials, Sorrento (Italy), March 2013, contribution: poster.

- A. Tercjak, J. Gutierrez, **L. Cano**, D. H. Builes, Electrostatic and tunneling force microscopy to study electric properties of sol-gel synthesized nanoparticles dispersed used block copolymers as template, Sol-Gel2013 XVII International Sol-Gel Conference, Madrid (Spain), August 2013, contribution: poster.
- D. Builes, H. Hernández, J. Hernández-Ortiz, **L. Cano**, I. Mondragon, A. Tercjak, Nanostructured unsaturated polyester using block copolymers: morphology, optical properties and fracture toughness relationship, VII Congreso Internacional de Materiales CIM 2013, Medellín (Colombia), October 2013, contribution: oral communication.
- D. H. Builes, H. Hernández, **L. Cano**, A. Tercjak, Fibrillated cellulose and block copolymers as a modifiers of unsaturated polyester nanocomposites, NANOSTRUC 2014 International Conference on Structural Nano Composites, Madrid (Spain), May 2014, contribution: oral communication.
- J. Gutierrez, **L. Cano**, D. H. Builes, R. Fernández, A. Tercjak, Advanced multifunctional nanostructured materials, NanoFunMat 2014, Pultusk (Poland), June 2014, contribution: oral communication.
- J. Gutierrez, **L. Cano**, S. Carrasco-Hernandez, R. Fernández, A. Tercjak, Blokezko kopolimeroetan oinarritutako funtzio anitzeko material nanoegituratu berriak, Materialen Zientzia eta Teknologia II. Kongresua, Donostia-San Sebastián (Spain), July 2014, contribution: poster.
- D. H. Builes, H. Hernández, **L. Cano**, A. Tercjak, Unsaturated polyester nanocomposites modified with sisal microfibrillated cellulose and PEG-*b*-PPG-*b*-PEG block copolymers: morphology and mechanical properties relationship, CIADICYP 2014 VIII Congreso Iberoamericano de Investigación en Celulosa y Papel, Medellín (Colombia), November 2014, contribution: oral communication.

- A. Tercjak, **L. Cano**, D. H. Builes, S. Carrasco-Hernandez, J. Gutierrez, Multiphasic materials based on block copolymers and nanostructured thermosets, EMN Meeting on Polymer, Orlando (USA), January 2015, contribution: oral communication.
- A. Tercjak, **L. Cano**, J. Gutierrez, Morphological structure and conductive properties of hybrid inorganic/organic materials based on block copolymers and synthesized TiO<sub>2</sub> nanoparticles, HYMA 2015 Fourth International Conference on Multifunctional, Hybrid and Nanomaterials, Sitges (Spain), March 2015, contribution: poster.
- A. Tercjak, **L. Cano**, S. Carrasco-Hernandez, R. Fernández, J. Gutierrez, Mechanical properties of composite materials by PeakForce Quantitative Nanomechanical Mapping technique, 4th International Symposium on Energy Challenges & Mechanics, Aberdeen (United Kingdom), August 2015, contribution: oral communication.

### 9.3.3. Research stays

- Research stay at the Institute for Physical and Chemical Processes (IPCF) of the Italian National Research Council (CNR) in Bari (Italy) from May 2014 to August 2014 working on the topic “Approaches for development of new nanocomposites based on colloidal inorganic nanoparticles”, supervised by Dr. M. Lucia Curri and funded by COST Action CM1101 Colloidal Aspects of Nanoscience for Innovative Processes and Materials.
- Research stay at the Institute of Chemistry and Processes for Energy, Environment and Health (ICPEES) of the European School of Chemistry, Polymers and Materials (ECPM) in the University of Strasbourg (France) from April 2015 to July 2015 working on the topic “Development of bionanocomposites based on chitosan and TiO<sub>2</sub> nanoparticles”, supervised by Dr. Luc Avérous and funded by the Basque Government.



## Appendix

### List of symbols

<b>A</b>	area
<b>r</b>	radius
<b>N</b>	degree of polymerization
<b><math>\chi</math></b>	Flory-Huggins interaction parameter
<b>f</b>	volume fraction of one block of block copolymer
<b>E</b>	flexural modulus
<b>L</b>	support span
<b>b</b>	specimen width
<b>d</b>	specimen depth
<b>m</b>	slope of the tangent of the load-deflection curve
<b>P</b>	load
<b>B</b>	SENB specimen thickness
<b>W</b>	SENB specimen depth
<b>a</b>	crack length
<b>U</b>	corrected integrated energy factor
<b><math>\Phi</math></b>	energy calibration factor
<b><math>K_{IC}</math></b>	critical stress intensity factor
<b><math>G_{IC}</math></b>	critical strain energy release rate
<b><math>M_n</math></b>	number average molecular weight
<b><math>M_w</math></b>	weight average molecular weight
<b><math>M_w/M_n</math></b>	polydispersity index
<b><math>T_g</math></b>	glass transition temperature
<b><math>R_s</math></b>	sheet resistivity
<b><math>\rho</math></b>	electrical resistivity
<b>t</b>	thickness
<b><math>\sigma</math></b>	electrical conductivity
<b><math>\theta</math></b>	contact angle
<b><math>\gamma_{SV}</math></b>	surface free energy of the solid
<b><math>\gamma_{LV}</math></b>	surface tension of the liquid

**List of abbreviations**

<b>AFM</b>	atomic force microscopy
<b>ATR</b>	attenuated total reflection
<b>CPS</b>	close-packed spherical morphology
<b>DDIOL</b>	dodecan-1,2-diol (C <sub>12</sub> H <sub>24</sub> (OH) <sub>2</sub> )
<b>DGEBA</b>	diglycidyl ether of bisphenol A
<b>DGEBA-MCDEA</b>	system based on diglycidyl ether of bisphenol A and 4,4'-methylene-bis(3-chloro-2,6-diethylaniline)
<b>DGEBA-MXDA</b>	system based on diglycidyl ether of bisphenol A and m-Xylylenediamine
<b>DIS</b>	disordered morphology
<b>DSC</b>	differential scanning calorimeter
<b>EFM</b>	electrostatic force microscopy
<b>γ-Fe<sub>2</sub>O<sub>3</sub>NC</b>	maghemite iron oxide nanocrystals
<b>γ-Fe<sub>2</sub>O<sub>3</sub>NC/PS-<i>b</i>-PMMA</b>	nanocomposites based on polystyrene- <i>block</i> -polymethyl methacrylate and maghemite iron oxide nanocrystals
<b>FTIR</b>	Fourier transform infrared spectroscopy
<b>G</b>	double-gyroidal morphology
<b>H</b>	hexagonally-packed cylindrical morphology
<b>I-V</b>	current-voltage
<b>ITO</b>	indium tin oxide
<b>L</b>	lamellar morphology
<b>LCST</b>	lower critical solution temperature
<b>MCDEA</b>	4,4'-methylene-bis(3-chloro-2,6-diethylaniline)
<b>MFM</b>	magnetic force microscopy
<b>MTS</b>	materials testing system
<b>MXDA</b>	m-Xylylenediamine
<b>ODE</b>	1-octadecene (C <sub>18</sub> H <sub>36</sub> )
<b>ODT</b>	order-disorder transition
<b>OLEA</b>	oleic acid (C <sub>17</sub> H <sub>33</sub> CO <sub>2</sub> H)

<b>OLEAM</b>	oleylamine (C <sub>18</sub> H <sub>35</sub> NH <sub>2</sub> )
<b>PEDOT:PSS</b>	poly-3,4-ethylenedioxythiophene- polystyrenesulfonate
<b>PEO</b>	polyethylene oxide
<b>PEO-<i>b</i>-PPO-<i>b</i>-PEO</b>	polyethylene oxide- <i>block</i> -polypropylene oxide- <i>block</i> - polyethylene oxide
<b>PMMA</b>	polymethyl methacrylate
<b>PPO</b>	polypropylene oxide
<b>PS</b>	polystyrene
<b>PS-<i>b</i>-PMMA</b>	polystyrene- <i>block</i> -polymethyl methacrylate
<b>PS-<i>b</i>-PMMA/(DGEBA-MCDEA)</b>	system based on diglycidyl ether of bisphenol A and 4,4'-methylene-bis(3-chloro-2,6-diethylaniline) modified with polystyrene- <i>block</i> -polymethyl methacrylate
<b>P3HT</b>	poly(3-hexylthiophene-2,5-diyl)
<b>QNM</b>	PeakForce quantitative nanomechanical measurements
<b>RIPS</b>	reaction induced phase separation
<b>S</b>	body-centered spherical morphology
<b>SEM</b>	scanning electron microscopy
<b>SENB</b>	single edge notched specimen
<b>TEM</b>	transmission electron microscopy
<b>TiO<sub>2</sub>NC</b>	titanium dioxide nanocrystals
<b>TiO<sub>2</sub>NC/PS-<i>b</i>-PMMA</b>	nanocomposites based on polystyrene- <i>block</i> - polymethyl methacrylate and titanium dioxide nanocrystals
<b>TiO<sub>2</sub>NR</b>	titanium dioxide nanorods
<b>TiO<sub>2</sub>NR/PS-<i>b</i>-PMMA</b>	nanocomposites based on polystyrene- <i>block</i> - polymethyl methacrylate and titanium dioxide nanorods
<b>TM-AFM</b>	tapping mode atomic force microscopy
<b>TMAO</b>	trimethylamino-N-oxide dihydrate ((CH <sub>3</sub> ) <sub>3</sub> NO·2H <sub>2</sub> O)
<b>TTIP</b>	titanium tetraisopropoxide (Ti(OPri) <sub>4</sub> )

<b>TUNA</b>	PeakForce tunneling atomic force microscopy
<b>UCST</b>	upper critical solution temperature
<b>UV-vis</b>	ultraviolet-visible
<b>XRD</b>	x-ray diffraction

## List of tables

### Chapter 5

**Table 5.1.** Sheet resistivity, thickness, electrical resistivity and conductivity values calculated for the selected electro-devices.

### Chapter 8

**Table 8.1.** Water contact angle and surface free energy values of the neat DGEBA-MXDA cured system and investigated PEO-*b*-PPO-*b*-PEO/(DGEBA-MXDA) cured systems.

## List of figures

### Chapter 1

**Figure 1.1.** Some examples of materials in the size range from 0.1 nm to 1 mm.

**Figure 1.2.** Illustration to demonstrate the effect of the increased surface area provided by nanomaterials.

**Figure 1.3.** Various applications of nanotechnology.

**Figure 1.4.** Schematic representation of some types of linear block copolymers: AB diblock copolymer (a), ABC triblock copolymer (b) and ABA triblock copolymer (c).

**Figure 1.5.** Theoretical phase diagram of an AB diblock copolymer.

**Figure 1.6.** Equilibrium morphologies of AB diblock copolymers in bulk.

**Figure 1.7.** Different kinds of nanofillers, depending on their shape.

**Figure 1.8.** Top-down and bottom-up approaches for the synthesis of nanoparticles.

**Figure 1.9.** Epoxide functional group.

**Figure 1.10.** Reactions which take place during the curing: primary amine hydrogen with an epoxy group (a), secondary amine hydrogen reacting with another epoxy group (b) and etherification reaction (c).

### Chapter 2

**Figure 2.1.** Schematic illustration of the AFM tapping mode operation.

**Figure 2.2.** Schematic illustration of the EFM operation.

**Figure 2.3.** Schematic illustration of the PeakForce TUNA operation.

**Figure 2.4.** Schematic illustration of the two-point mode and four-point collinear probe mode.

**Figure 2.5.** Schematic illustration of the MFM operation.

**Figure 2.6.** Setup of three-bending system for the flexural test (a) and the fracture toughness test (b), and corresponding specimen shapes.

### Chapter 3

**Figure 3.1.** Chemical structure of the PS-*b*-PMMA diblock copolymer.

**Figure 3.2.** XRD pattern (a) and AFM image (5  $\mu\text{m}$  x 5  $\mu\text{m}$  and inset of 1  $\mu\text{m}$  x 1  $\mu\text{m}$ ) (b) of the commercial TiO<sub>2</sub> nanocrystals and AFM phase profile of a TiO<sub>2</sub> nanocrystal (c). The bar on the AFM phase image indicates the position where the profile was measured.

**Figure 3.3.** DSC thermograms of the neat PS-*b*-PMMA block copolymer and TiO<sub>2</sub>NC/PS-*b*-PMMA nanocomposites containing different TiO<sub>2</sub> nanocrystal contents.

**Figure 3.4.** AFM phase images (5 μm x 5 μm and inset of 1 μm x 1 μm) of the neat PS-*b*-PMMA block copolymer (a) and TiO<sub>2</sub>NC/PS-*b*-PMMA nanocomposites containing 0.5 (b), 1 (c), 2 (d), 3 (e) and 4 (f) wt % TiO<sub>2</sub> nanocrystal contents.

**Figure 3.5.** EFM phase images (2 μm x 2 μm) of the neat PS-*b*-PMMA block copolymer (a) and TiO<sub>2</sub>NC/PS-*b*-PMMA nanocomposites containing 0.5 (b), 1 (c), 2 (d), 3 (e) and 4 (f) wt % TiO<sub>2</sub> nanocrystal contents obtained by applying 0, 6, 9, -6 and -9 V.

**Figure 3.6.** UV-vis absorption spectra of the neat PS-*b*-PMMA block copolymer and TiO<sub>2</sub>NC/PS-*b*-PMMA nanocomposites containing different TiO<sub>2</sub> nanocrystal contents.

#### Chapter 4

**Figure 4.1.** Chemical structure of the oleic acid.

**Figure 4.2.** TEM micrograph (a) and FTIR spectrum (b) of oleic acid-coated TiO<sub>2</sub> nanorods.

**Figure 4.3.** Visual appearance of the neat PS-*b*-PMMA block copolymer (a) and TiO<sub>2</sub>NR/PS-*b*-PMMA nanocomposite solutions containing 1 (b), 3 (c), 5 (d), 10 (e), 15 (f), 20 (g), 30 (h), 40 (i) and 50 (j) wt % TiO<sub>2</sub> nanorod contents.

**Figure 4.4.** AFM phase image (2 μm x 2 μm) of the neat PS-*b*-PMMA block copolymer.

**Figure 4.5.** AFM phase images (2 μm x 2 μm and inset of 0.5 μm x 0.5 μm) of TiO<sub>2</sub>NR/PS-*b*-PMMA nanocomposites containing 1 (a), 3 (b), 5 (c), 10 (d), 15 (e), 20 (f), 30 (g), 40 (h) and 50 (i) wt % TiO<sub>2</sub> nanorod contents.

**Figure 4.6.** EFM phase images (3 μm x 3 μm) of the neat PS-*b*-PMMA block copolymer (a) and TiO<sub>2</sub>NR/PS-*b*-PMMA nanocomposites containing 3 (b), 10 (c) and 20 (d) wt % TiO<sub>2</sub> nanorod contents obtained by applying 0, 6, 9, -6 and -9 V.

**Figure 4.7.** Current-voltage curves (I-V) of the neat PS-*b*-PMMA block copolymer and TiO<sub>2</sub>NR/PS-*b*-PMMA nanocomposites containing different TiO<sub>2</sub> nanorod contents obtained by applying a voltage sweep between -4 and 4 V.

**Figure 4.8.** TUNA current images (3 μm x 3 μm) taken at voltages of -6, 0 and 6 V for 30 (a), 40 (b) and 50 (c) wt % TiO<sub>2</sub>NR/PS-*b*-PMMA nanocomposites and same contents 30 (d), 40 (e) and 50 (f) wt % TiO<sub>2</sub>NR/PS-*b*-PMMA after being exposed to UV light for 24 hours. The graphs correspond to horizontal section profiles of each -6 and 6 V images.

**Figure 4.9.** Schematic representation of the conductive behavior of TiO<sub>2</sub>NR/PS-*b*-PMMA nanocomposites containing different TiO<sub>2</sub> nanorod contents.

**Figure 4.10.** UV-vis absorption spectra of the neat PS-*b*-PMMA block copolymer and TiO<sub>2</sub>NR/PS-*b*-PMMA nanocomposites containing different TiO<sub>2</sub> nanorod contents.

## Chapter 5

**Figure 5.1.** AFM phase images (3 μm x 3 μm) of ITO-glass/PEDOT:PSS/P3HT/(TiO<sub>2</sub>NR/PS-*b*-PMMA) electro-devices fabricated with 50 (a), 60 (b) and 70 (c) wt % TiO<sub>2</sub>NR/PS-*b*-PMMA nanocomposite layer and of ITO-glass/PEDOT:PSS/P3HT/TiO<sub>2</sub>NR electro-device (d).

**Figure 5.2.** Current-voltage (I-V) curves of ITO-glass/PEDOT:PSS/P3HT/(TiO<sub>2</sub>NR/PS-*b*-PMMA) electro-devices fabricated with 50, 60 and 70 wt % TiO<sub>2</sub>NR/PS-*b*-PMMA nanocomposite layer and of ITO-glass/PEDOT:PSS/P3HT/TiO<sub>2</sub>NR electro-device, by applying a voltage sweep between -6 and 6 V.

**Figure 5.3.** TUNA images (3 μm x 3 μm) taken at 6 V of ITO-glass/PEDOT:PSS/P3HT/(TiO<sub>2</sub>NR/PS-*b*-PMMA) electro-devices fabricated with 50 (a), 60 (b) and 70 (c) wt % TiO<sub>2</sub>NR/PS-*b*-PMMA nanocomposite layer and of ITO-glass/PEDOT:PSS/P3HT/TiO<sub>2</sub>NR electro-device (d). The graphs correspond to the current profiles marked on the TUNA images.

**Figure 5.4.** Schematic representation of the fabricated electro-devices based on TiO<sub>2</sub>NR/PS-*b*-PMMA nanocomposites.

**Figure 5.5.** UV-vis absorption spectra of ITO-glass/PEDOT:PSS/P3HT/(TiO<sub>2</sub>NR/PS-*b*-PMMA) electro-devices fabricated with 50, 60 and 70 wt % TiO<sub>2</sub>NR/PS-*b*-PMMA nanocomposite layer and of ITO-glass/PEDOT:PSS/P3HT/TiO<sub>2</sub>NR electro-device.

## Chapter 6

**Figure 6.1.** Chemical structure of the oleylamine.

**Figure 6.2.** TEM micrograph (a) and FTIR spectrum (b) of oleic acid- and oleylamine-coated γ-Fe<sub>2</sub>O<sub>3</sub> nanocrystals.

**Figure 6.3.** Visual appearance of the neat PS-*b*-PMMA block copolymer and γ-Fe<sub>2</sub>O<sub>3</sub>NC/PS-*b*-PMMA nanocomposite solutions containing 1, 3, 5, 10, 20, 30, 40, 50 and 60 wt % γ-Fe<sub>2</sub>O<sub>3</sub> nanocrystal contents.

**Figure 6.4.** AFM phase image (2 μm x 2 μm and inset of 0.5 μm x 0.5 μm) of the neat PS-*b*-PMMA block copolymer.

**Figure 6.5.** AFM phase images (2  $\mu\text{m}$  x 2  $\mu\text{m}$  and inset of 0.5  $\mu\text{m}$  x 0.5  $\mu\text{m}$ ) of  $\gamma\text{-Fe}_2\text{O}_3\text{NC/PS-}b\text{-PMMA}$  nanocomposites containing 1 (a), 3 (b), 5 (c), 10 (d), 20 (e), 30 (f), 40 (g), 50 (h) and 60 (i) wt %  $\gamma\text{-Fe}_2\text{O}_3$  nanocrystal contents.

**Figure 6.6.** Detailed AFM phase image (400 nm x 400 nm) (a) of the  $\gamma\text{-Fe}_2\text{O}_3$  nanocrystal clusters present in the 5 wt %  $\gamma\text{-Fe}_2\text{O}_3\text{NC/PS-}b\text{-PMMA}$  nanocomposite. AFM phase profile (b) corresponds to the white line of the AFM phase image.

**Figure 6.7.** Schematic representation of the main components of the system, the neat PS-*b*-PMMA block copolymer and  $\gamma\text{-Fe}_2\text{O}_3$  nanocrystals, the neat block copolymer and nanocomposite solutions in toluene and the neat block copolymer and nanocomposite films with low, medium and high nanocrystal contents.

**Figure 6.8.** SEM image of the neat PS-*b*-PMMA block copolymer.

**Figure 6.9.** SEM images of  $\gamma\text{-Fe}_2\text{O}_3\text{NC/PS-}b\text{-PMMA}$  nanocomposites containing 1 (a), 3 (b), 5 (c), 10 (d), 20 (e), 30 (f), 40 (g), 50 (h) and 60 (i) wt %  $\gamma\text{-Fe}_2\text{O}_3$  nanocrystal contents. The inset in c shows a  $\gamma\text{-Fe}_2\text{O}_3$  nanocrystal cluster present in the 5 wt %  $\gamma\text{-Fe}_2\text{O}_3\text{NC/PS-}b\text{-PMMA}$  nanocomposite with higher magnification.

**Figure 6.10.** AFM phase (a, c, e and g) and MFM images (b, d, f and h) of 5, 30 and 60 wt %  $\gamma\text{-Fe}_2\text{O}_3\text{NC/PS-}b\text{-PMMA}$  nanocomposites and pristine  $\gamma\text{-Fe}_2\text{O}_3$  nanocrystals films, respectively, after being exposed to UV light for 24 hours (2  $\mu\text{m}$  x 2  $\mu\text{m}$ ). Digital images of 5 (i), 30 (j) and 60 (k) wt %  $\gamma\text{-Fe}_2\text{O}_3\text{NC/PS-}b\text{-PMMA}$  nanocomposites and pristine  $\gamma\text{-Fe}_2\text{O}_3$  nanocrystals (l) solutions in presence of a magnet.

## Chapter 7

**Figure 7.1.** Chemical structure of the DGEBA epoxy resin.

**Figure 7.2.** Chemical structure of the MCDEA curing agent.

**Figure 7.3.** Visual appearance of the neat DGEBA-MCDEA cured system (a) and 5 (b), 15 (d) and 25 (f) wt % PS-*b*-PMMA/(DGEBA-MCDEA) cured systems prepared by the non-solvent method and 5 (c), 15 (e) and 25 (g) wt % PS-*b*-PMMA/(DGEBA-MCDEA) cured systems prepared by the solvent method.

**Figure 7.4.** DSC thermograms of the neat DGEBA-MCDEA cured system, neat PS-*b*-PMMA block copolymer and 5, 15, 25 and 50 wt % PS-*b*-PMMA/(DGEBA-MCDEA) cured systems prepared by the non-solvent method (a) and by the solvent method (b). The dot line in each graph indicates the theoretical  $T_g$  values calculated by the Fox equation.

**Figure 7.5.** AFM phase image (1  $\mu\text{m}$  x 1  $\mu\text{m}$  and inset of 3  $\mu\text{m}$  x 3  $\mu\text{m}$ ) of the neat DGEBA-MCDEA cured system.

**Figure 7.6.** AFM phase images (1  $\mu\text{m}$  x 1  $\mu\text{m}$  and inset of 3  $\mu\text{m}$  x 3  $\mu\text{m}$ ) of 5 (a), 15 (b), 25 (c) and 50 (d) wt % PS-*b*-PMMA/(DGEBA-MCDEA) cured systems prepared by the non-solvent method and 5 (e), 15 (f), 25 (g) and 50 (h) wt % PS-*b*-PMMA/(DGEBA-MCDEA) cured systems prepared by the solvent method.

**Figure 7.7.** Schematic representation of the morphologies obtained for thermosetting systems modified with low and high PS-*b*-PMMA block copolymer contents.

**Figure 7.8.** Flexural modulus (E) of the neat DGEBA-MCDEA cured system and 5, 15 and 25 wt % PS-*b*-PMMA/(DGEBA-MCDEA) cured systems prepared by the non-solvent and the solvent method.

**Figure 7.9.** Critical stress intensity factor ( $K_{IC}$ ) (a) and critical strain energy release rate ( $G_{IC}$ ) (b) of the neat DGEBA-MCDEA cured system and 5, 15 and 25 wt % PS-*b*-PMMA/(DGEBA-MCDEA) cured systems prepared by the non-solvent and the solvent method.

**Figure 7.10.** Elastic modulus PeakForce QNM image (1  $\mu\text{m}$  x 1  $\mu\text{m}$ ) of the neat DGEBA-MCDEA cured system.

**Figure 7.11.** Elastic modulus PeakForce QNM images (1  $\mu\text{m}$  x 1  $\mu\text{m}$ ) of 5 (a), 15 (b), 25 (c) and 50 (d) wt % PS-*b*-PMMA/(DGEBA-MCDEA) cured systems prepared by the non-solvent method and 5 (e), 15 (f), 25 (g) and 50 (h) wt % PS-*b*-PMMA/(DGEBA-MCDEA) cured systems prepared by the solvent method.

## Chapter 8

**Figure 8.1.** Chemical structure of the MXDA curing agent.

**Figure 8.2.** Chemical structure of the PEO-*b*-PPO-*b*-PEO triblock copolymer.

**Figure 8.3.** Visual appearance of the neat DGEBA-MXDA cured system (a) and 5 (b), 15 (c), 25 (d) and 50 (e) wt % PEO-*b*-PPO-*b*-PEO/(DGEBA-MXDA) cured systems.

**Figure 8.4.** DSC thermograms of the neat DGEBA-MXDA cured system and 5, 15, 25 and 50 wt % PEO-*b*-PPO-*b*-PEO/(DGEBA-MXDA) cured systems. The dot line indicates the theoretical  $T_g$  values calculated by the Fox equation.

**Figure 8.5.** AFM phase image (1  $\mu\text{m}$  x 1  $\mu\text{m}$  and inset of 5  $\mu\text{m}$  x 5  $\mu\text{m}$ ) of the neat DGEBA-MXDA cured system.

**Figure 8.6.** AFM phase images (1  $\mu\text{m}$  x 1  $\mu\text{m}$  and inset of 5  $\mu\text{m}$  x 5  $\mu\text{m}$ ) of 5 (a), 15 (b), 25 (c) and 50 (d) wt % PEO-*b*-PPO-*b*-PEO/(DGEBA-MXDA) cured systems.

**Figure 8.7.** Schematic representation of the morphologies obtained for 5, 15 and 25 wt % PEO-*b*-PPO-*b*-PEO/(DGEBA-MXDA) cured systems.

**Figure 8.8.** TEM micrographs of the neat DGEBA-MXDA cured system (a) and 5 (b), 15 (c) and 25 (d) wt % PEO-*b*-PPO-*b*-PEO/(DGEBA-MXDA) cured systems.

**Figure 8.9.** Flexural modulus (E) of the neat DGEBA-MXDA cured system and 5, 15 and 25 wt % PEO-*b*-PPO-*b*-PEO/(DGEBA-MXDA) cured systems.

**Figure 8.10.** Critical stress intensity factor ( $K_{IC}$ ) (a) and critical strain energy release rate ( $G_{IC}$ ) (b) of the neat DGEBA-MXDA cured system and 5, 15 and 25 wt % PEO-*b*-PPO-*b*-PEO/(DGEBA-MXDA) cured systems.

**Figure 8.11.** Elastic modulus PeakForce QNM images (1  $\mu\text{m}$  x 1  $\mu\text{m}$ ) of the neat DGEBA-MXDA cured system (a) and 5 (b), 15 (c) and 25 (d) wt % PEO-*b*-PPO-*b*-PEO/(DGEBA-MXDA) cured systems.

**Figure 8.12.** UV-vis transmittance spectra of the neat DGEBA-MXDA cured system and 5, 15, 25 and 50 wt % PEO-*b*-PPO-*b*-PEO/(DGEBA-MXDA) cured systems.

**Figure 8.13.** Images of a water droplet in contact with the neat DGEBA-MXDA cured system (a) and 5 (b), 15 (c), 25 (d) and 50 (e) wt % PEO-*b*-PPO-*b*-PEO/(DGEBA-MXDA) cured systems.

